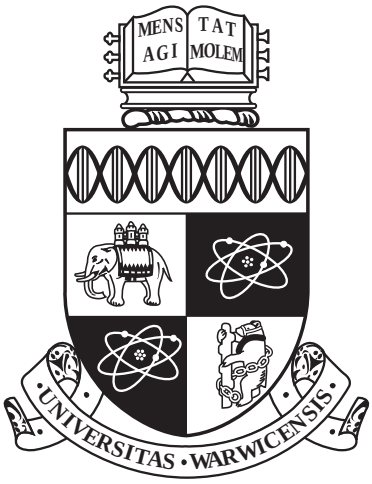

Fine spatiotemporal calcium signals and kinematic properties revealed by motion-corrected calcium images of contracting myometrium

by

Fiona Loftus

Thesis

Submitted to the University of Warwick

for the degree of

Doctor of Philosophy

Warwick Systems Biology Doctoral Training Centre

September 2015

THE UNIVERSITY OF
WARWICK

Contents

List of Tables

List of Figures

Acknowledgments

Thank you to my supervisors Dr Magnus Richardson and Dr Anatoly Shmygol for their ideas, support and enthusiasm. Thank you to the UK Biotechnology and Biological Sciences Research Council (BBSRC) for funding this research.

Declarations

This thesis is submitted to the University of Warwick in support of my application for the degree of Doctor of Philosophy. It has been composed by myself and has not been submitted in any previous application for any degree.

The work presented (including data generated and data analysis) was carried out by the author except in the cases outlined below:
Experimental recordings were collected by Dr Gilles Bru-Mercier and Dr Anatoly Shmygol.

Parts of this thesis have been published by the author in Loftus et al. (2014) and Loftus et al. (2015).

Abstract

Successful childbirth depends on precisely coordinated uterine contractions during labour. Calcium indicator fluorescence imaging is one of the main techniques for investigating the mechanisms governing this physiological process and its pathologies. The effective spatiotemporal resolution of calcium signals is, however, limited by the motion of contracting tissue: structures of interest that are of the order of microns can move over a hundred times their width during a contraction. The simultaneous changes in local intensity and tissue configuration make motion tracking a nontrivial image-analysis problem and confound many of the standard techniques. In this thesis I present a method that tracks local motion throughout the tissue allowing for an almost complete removal of motion artifacts. This provides a stabilised calcium signal down to a pixel resolution which, for the data examined, is of the order of a few microns. As a byproduct of the image stabilisation, a complete kinematic description of the contraction-relaxation cycles is also obtained containing novel information about the mechanical response of the tissue, such as the identification of a characteristic length scale, of the order of 40-50 microns, below which tissue motion is homogeneous. This kinematic information will help to fill the gaps in experimentally recorded mechanical properties of contracting myometrium. Applying the algorithm to over twenty datasets, I show that for the first time unrestricted single-cell calcium measurements can be taken from myometrial tissue slices over multiple contraction-relaxation cycles. I investigate single-cell calcium signals in between contractions and compare single- cell calcium dynamics in control and oxytocin-treated myometrium. Additionally, I use the kinematics of tissue motion to compare calcium signals at the subcellular level and local contractile motion. Freely modifiable code written in the MATLAB environment was published under the GNU General Public license in the hope that it will be useful to researchers analysing these or similar datasets.

Abbreviations

MHC	Myosin heavy chain
MLC	Myosin light chain
MLCK	Myosin light chain kinase
MLCP	Myosin light chain phosphatase
$[Ca^{2+}]_i$	Intracellular free calcium ions
PLC-β	Phospholipase C-β
PIP_2	Phosphatidylinositol-bis-phosphate
IP_3	Inositol-tris-phosphate
DAG	Diacyglycerol
SR	Sarcoplasmic reticulum
SOCE	Store-operated calcium release
ROCK	Rho kinase
PKC	Protein kinase C
PIV	Particle image velocimetry
ROI	Region of interest

Chapter 1

Introduction

1.1 Uterine contractility

The physiological mechanisms governing uterine contractility are complex and dynamic. For the majority of pregnancy, uterine contractions are weak and unsynchronised, and this quiescent environment is essential for harbouring the foetus. The contractions progressively increase towards the end of pregnancy, and culminate in precisely timed and coordinated uterine contractions that expel the foetus during labour. The correct timing and development of such phasic regular contractions is essential to successful labour. Premature onset of synchronised contractions leads to preterm labour and subsequent birth; a breakdown in the coordination of contractions (i.e. weak and unsynchronised) can result in uterine dystocia, including prolonged labour, caesarean section or postpartum haemorrhage. Elucidation of cellular- and tissue-level mechanisms regulating myometrial contractility is crucial for improvement in management of such obstetric abnormalities.

The human uterus is a hollow organ, comprising three histologically distinct layers (from inside to outside): the endometrium, the myometrium and the perimetrium (Fig. 1.1). The endometrium is made up of a layer of connective tissue lined with a surface epithelium. It functions as a lining for the uterus and supports the implantation of a fertilised ovum and the growth of a foetus. The perimetrium is a serous membrane forming the outer layer of the uterus. Contractility of the uterus occurs within the myometrium; the muscle mass that lies between the endometrium and the perimetrium.

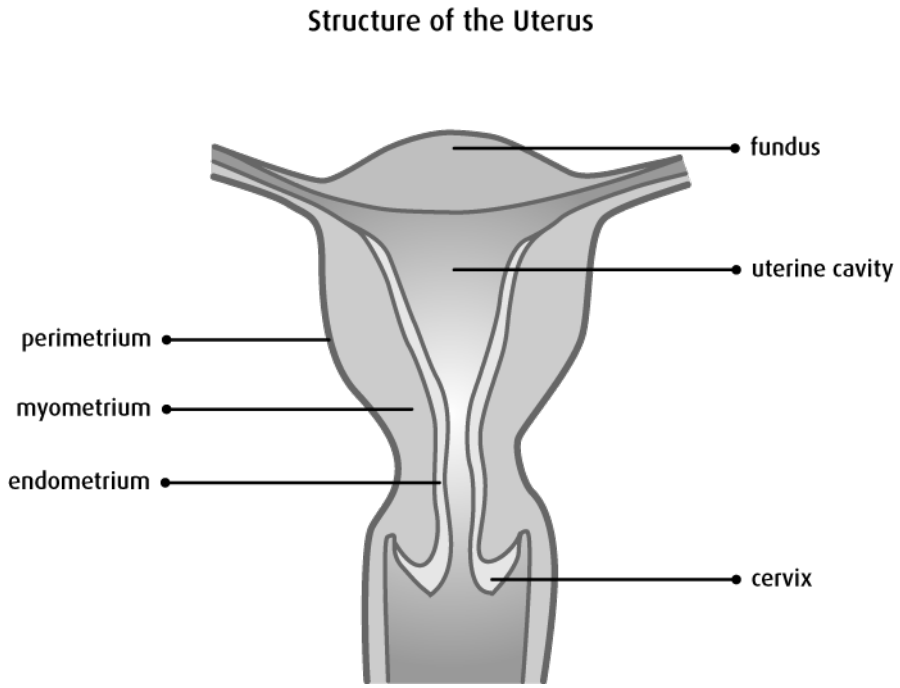

Figure 1.1: **Structure of the non-pregnant human uterus** (from http://www.cancer.ca/)

1.1.1 Contraction of uterine myocytes

The basic functional unit of the myometrium is the myocyte; these are spindle-shaped smooth muscle cells ranging in size from about 2 to 10μm in diameter and from 200 to 600μm in length in a non-pregnant uterus, non-contractile state (Kuriyama et al., 1998; Fig. 1.2A). The spindle shape is determined by the cytoplasmic cytoskeleton (Yu and Lopez Bernal, 1998). Like all smooth muscle cells, myometrial myocytes are equipped with contractile apparatus; the major components are illustrated in Fig. 1.2. The contractile motion occurs via the sliding of the thin actin filaments along the thick myosin filaments causing a shortening of the cell (Fig. 1.2B). The myosin filaments involved in human muscle contraction are myosin class II proteins; these are made up of two myosin heavy chains (MHC) and two pairs of myosin light chains (MLC). The structure of the filaments can be viewed as three different domains: the 'head', 'neck' and 'tail' (Fig. 1.2C). The tail domain is made up of the C-terminal of the two MHCs, which are coiled together to form a rod-like structure. Together the two N-terminals of the MHCs form the head domain: two protruding globular heads which provide the force required for the contraction of the cell. The intermediate neck domain contains the binding sites for the MLCs; one of each of MLC_{20} (regulatory light chain) and MLC_{17} (essential light chain) bind

to each of the MHCs at these sites.

During contractions, the myosin head acts as a crossbridge, cyclically attaching, performing a power stroke then detaching from the actin filament, thus causing the actin and myosin filaments to slide over each other. The state of contractility of the cell is predominantly regulated by the concentration of intracellular free calcium ions ($[Ca^{2+}]_i$); a sharp rise in $[Ca^{2+}]_i$ activates the contractile machinery. $[Ca^{2+}]_i$ bind to calmodulin proteins to form complexes which activate myosin light chain kinases (MLCK). MLCK catalyses the phosphorylation of MLC_{20}; this activates the ATPase activity of the myosin head region and causes a conformation change enabling the interaction of myosin with actin. Together these processes provide the energy and conditions for the actomysoin crossbridge cycling which causes the cell to contract. The inactivation of MLCK, a drop in $[Ca^{2+}]_i$ and the dephosphorylation of MLC by myosin light chain phosphatase (MLCP) effects the subsequent relaxation of the cell. The changes in $[Ca^{2+}]_i$ associated with the contraction and relaxation of myometrial myocytes contribute to the 'excitation-contraction coupling' process; a fundamental component of smooth muscle contraction.

1.1.2 Excitation-contraction coupling

Myometrial myocytes are electrically excitable, maintaining a transmembrane gradient of calcium, potassium, sodium and chloride ions. Ions are selectively transported across the cell membrane via pumps and co-transporters, travelling down their respective electro-chemical gradients. The relative concentrations of ions inside and outside of the cell and the mechanisms by which the respective channels are opened regulate the cell's membrane potential; a key factor in determining the contractile state of the cell. The type and density of these channels can vary between individual myometrial myocytes at the same stage of gestation (Jones et al., 2004; Blanks et al., 2007) and over the course of gestation (Inoue and Sperelakis, 1991; Brainard et al., 2007).

The membrane potential of human myometrial myocytes tends to depolarise during the course of pregnancy (from ~ -70mV at week 29 of gestation to ~ -55mV at term and during labour; Parkington et al., 1999). During a contraction, there is a sharp rise in the cell's membrane potential (an action potential), which triggers the intracellular contractile machinery. This inward depolarising current is primary carried by calcium ions that enter the cell through L-type calcium channels (Shmigol et al., 1998). L-type calcium channels are activated by a depolarisation of the cell membrane, with an activation threshold of ~ -50mV. The

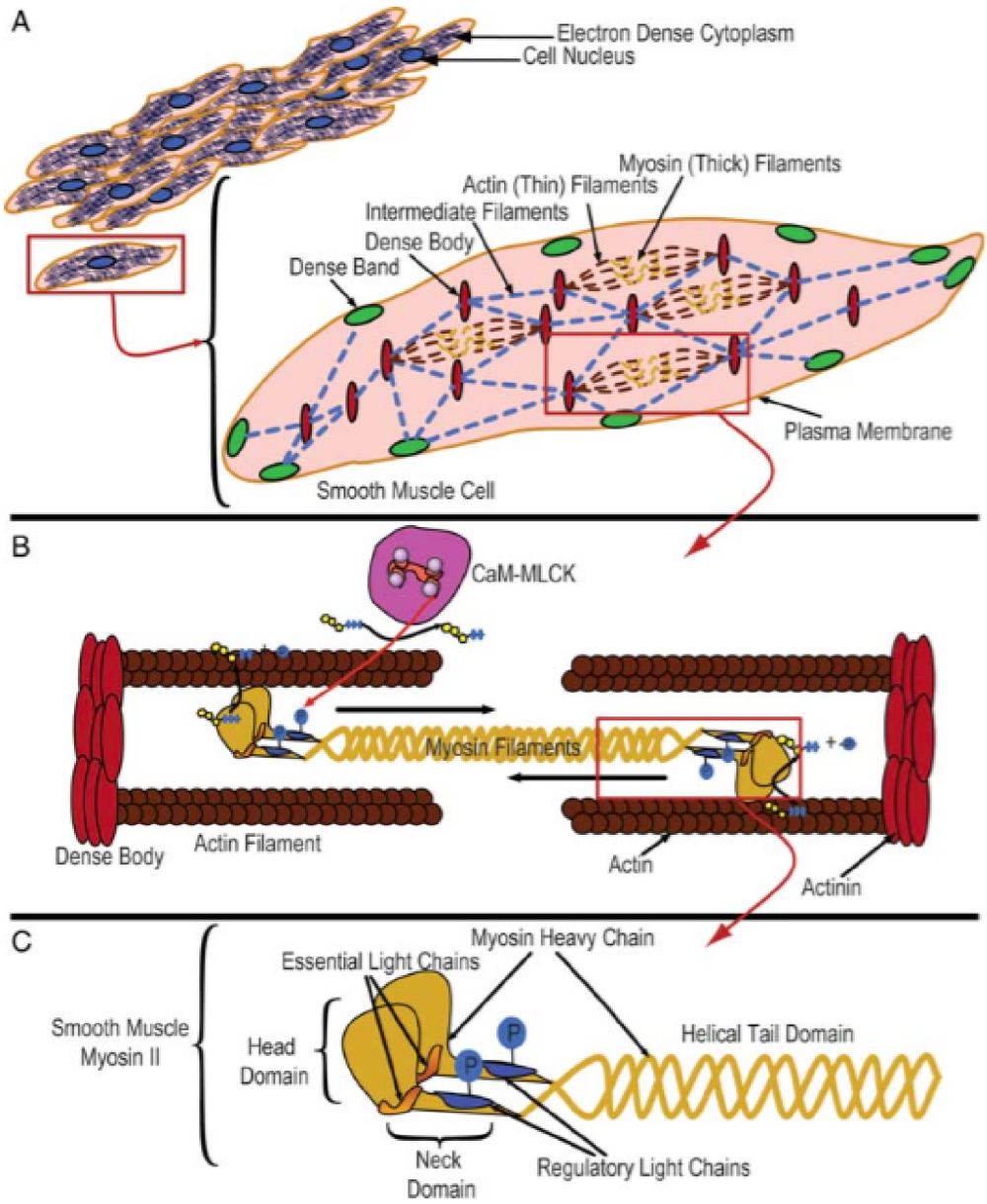

Figure 1.2: **Myometrial smooth muscle contraction** (A) The structural components (dense bodies, dense bands, intermediate filaments) and contractile machinery (thick and thin filaments) in myometrial myocytes. (B) Sliding of the actin filaments over the myosin filaments causes contraction of the cell, mediated via the calmodulin-dependent phosphorylation of the regulatory light chains. (C) Myosin filaments are made up of two myosin heavy chains and two pairs of myosin light chains. From Aguilar and Mitchell (2010)

action potential is terminated by outward potassium currents through both calcium- and voltage-sensitive potassium channels (Khan et al., 2001; Knock et al., 2004; Blanks et al., 2007). This results in a partial repolarisation of the cell and one of two types of action potential waveform: a plateau type or a spike type (Nakao et al., 1997; Shmygol et al., 2007). With either type of waveform, the action potential triggers a contraction which lasts for the duration of the action potential (1.5-2min) before full repolarisation of the cell to ~ -55mV gives rise to cell relaxation.

Myometrial tissue is myogenic, i.e., action potentials are generated by the muscle cells without the need for extrinsic neural or hormonal stimulation. This property of myometrium is clearly evidenced in the data used in this thesis: we examine and process calcium indicator fluorescence images of contracting myometrium, the majority of which undergo spontaneous contractions. The depolarisation of the membrane during pregnancy brings it much closer to the activation threshold of the L-type calcium channels, preparing the tissue for contraction-inducing action potentials during labour. However, the mechanism through which the cell becomes sufficiently depolarised to activate the L-type calcium channels and trigger a calcium-mediated action potential remains unknown. Evidence for specialised pacemaker cells, which are present in some other smooth muscle tissue (e.g., cardiac and gastrointestinal tract) has not been found in the myometrium (Duquette et al., 2005). The current view is that there is no fixed site of action potential initiation and that multiple and variable cells/regions have the ability to trigger contraction-inducing action potentials (Lammers, 2013; Young and Barendse, 2014; Wray et al., 2014)

1.1.3 The role of oxytocin

The hormone oxytocin is well known for stimulating myometrial contractions. It facilitates contraction in the human myometrium by increasing the frequency, amplitude and duration of action potentials (Nakao et al., 1997; Shmygol et al., 2006). Synthetic compounds to activate and inhibit the oxytocin receptor have long been used in the management of dysfunctional and preterm births. However, the success of these interventions is limited; the use of oxytocin agonists to augment labour has been reported to be only 50% effective (Blanch et al., 1998; Arrowsmith and Wray, 2014). Extensive research has been carried out on oxytocin and this has revealed that its role in reproduction is complex and varied. The complexity of its role means that although the net effect of oxytocin on uterine contractions is understood some of the pathways have not yet been elucidated; further research is therefore required

to improve the effectiveness of oxytocin receptor agonists and antagonists in clinical treatment of dysfunctional and preterm labour . In Chapters 4 and 5 we illustrate the effects of oxytocin application on $[Ca^{2+}]_i$ and the kinematics of tissue contraction. Here we provide an overview of some of the known pathways by which oxytocin regulates parturition; these include Ca^{2+} release from internal stores, Ca^{2+} entry from the extracellular space and Ca^{2+}-sensitisation.

Sources of Ca^{2+} for increases in $[Ca^{2+}]_i$ in myometrial smooth muscle cells are both extracellular (entering as currents through voltage-activated calcium channels, as previously discussed) and intracellular. Oxytocin is best known for inducing myometrial contractions through a release of Ca^{2+} from intracellular stores. Simultaneous measurements of Ca^{2+} in the sarcoplasmic reticulum (SR) and $[Ca^{2+}]_i$ in isolated rat myometrial cells show that application of oxytocin decreases the concentration of SR Ca^{2+} and increases $[Ca^{2+}]_i$ (Shmygol et al., 2006). Oxytocin receptors are G-protein coupled receptors and the action of oxytocin binding to its receptor activates the $G\alpha_{q/11}$ protein which couples to phospholipase C-β (PLC-β). PLC-β catalyses the hydrolysis of phosphatidylinositol-bis-phosphate (PIP_2) into inositol-tris-phosphate (IP_3) and diacyglycerol (DAG). IP_3 triggers the release of Ca^{2+} from the SR, resulting in an increase in $[Ca^{2+}]_i$. Release of Ca^{2+} from internal stores is sufficient to induce contractions; human myometrial strips bathed in calcium-free solution exhibit oxytocin-induced contractions albeit of a smaller magnitude (Luckas et al., 1999). The increased levels of $[Ca^{2+}]_i$ activate the contractile mechanisms by formation of the calcium/calmodulin complex detailed above.

The reduction in the magnitude of oxytocin-induced contractions in myometrial strips in the absence of external Ca^{2+} reported in Luckas et al. (1999) indicate that oxytocin also affects the influx of Ca^{2+} from the extracellular space. Indeed, in human myometrial strips when the SR has been disabled by application of thapsigargin, application of oxytocin still produces a marked increase in the amplitude and duration of contractions Shmygol et al. (2006). In the absence of extracellular Ca^{2+}, application of oxytocin to isolated human (Thornton et al., 1992) and rat (Arnaudeau et al., 1994b) myometrial cells, as well as to human myometrial strips (Luckas et al., 1999) produces an initial $[Ca^{2+}]_i$ transient, smaller in amplitude than those produced in the presence of extracellular Ca^{2+}. However, Thornton et al. (1992) demonstrated that subsequent applications of oxytocin fail to illicit a response in $[Ca^{2+}]_i$. This indicates that under physiological conditions, IP_3-mediated Ca^{2+} release from the SR triggers Ca^{2+} entry from the extracellular space.

Capacitative Ca^{2+} entry or store-operated Ca^{2+} entry (SOCE) may contribute to this influx. When the Ca^{2+} store pumps (SR and endoplasmic reticulum cal-

cium ATPase; SERCA) in an immortalised myometrial-derived cell line are inhibited by thapsigargin, a greater increase in $[Ca^{2+}]_i$ following replacement of extracellular Ca^{2+} to Ca^{2+}-free medium is seen than when thapsigargin is not applied, providing evidence for SOCE in the myometrium (Monga et al., 2016). A study by Shlykov and Sanborn (2004) supports suggestions that capacitative Ca^{2+} plays a role in oxytocin-induced contractions; 1-oleoyl-2-acetyl-*sn*-glycerol, a membrane-permeant analogue of DAG, activates extracellular Ca^{2+} entry through TrpC in primary myometrial cells and immortalised myometrial cell line PMH1. However, the role of SOCE in oxytocin-induced myometrial contractions is debatable. The simultaneous recordings of SR Ca^{2+} and $[Ca^{2+}]_i$ in the study by Shmygol et al. (2006) show only an initial decrease in SR Ca^{2+}; for SOCE we would expect to see a persistent decrease in SR Ca^{2+}. The increase in $[Ca^{2+}]_i$ following IP_3-mediated Ca^{2+} release from the SR induces opening Ca^{2+}-activated chloride and cation channels, leading to depolarisation of the cell membrane (Arnaudeau et al., 1994a). Depolarisation of the membrane will contribute to Ca^{2+} influx from the extracellular space by opening the L-Type calcium channels; these Ca^{2+} -activated channels therefore likely play a significant role in the increased frequency of oxytocin-induced contractions.

As previously discussed, the contractile state of myometrial myocytes is dependent on the phosphorylation and dephosphorylation of MLC by MLCK and MLCP respectively. In addition to the Ca^{2+}-dependent pathways detailed above, oxytocin increases the force of contraction in a Ca^{2+}-independent manner by altering the ratio between MLCK and MCLP. This process, known as calcium sensitisation, involves the inhibition of MCLP, prolonging the phosphorylation of MLC and leading to enhanced tension in a Ca^{2+}-independent manner. Evidence for calcium sensitisation as a pathway by which oxytocin affects contractions can be found in studies showing a decreased rate of relaxation in oxytocin-induced contractions (Thornton et al., 1998; Shmygol et al., 2006; Gullam et al., 2009). Thornton et al. (1998) also showed that in the absence of extracellular Ca^{2+} oxytocin increased the force of contractions without affecting the peak amplitude of $[Ca^{2+}]_i$. Further evidence can be found in a study by Kupittayanant et al. (2001), in which application of oxytocin to human myometrial strips depolarised by KCl could increase the force of contraction without altering $[Ca^{2+}]_i$.

The molecular mechanisms by which oxytocin-induced sensitisation of the contractile apparatus to $[Ca^{2+}]_i$ are complex and the pathways have yet to be fully elucidated. The activation of RhoA by stimulation of receptors coupled to $G\alpha_{12/13}$ is one mechanism by which Ca^{2+}-sensitisation occurs in the myometrium. RhoA in

turn triggers the activation of Rho kinase (ROCK), which inhibits MLCP by phosphorylation of its myosin binding subunit. Oxytocin is known to contribute to Ca^{2+}-sensitisation in a ROCK dependent way: pharmacological inhibition of ROCK was associated with a decrease in force of oxytocin-induced contractions in human myometrial strips (Kupittayanant et al., 2001; Woodcock et al., 2004; Hudson et al., 2012). It is likely that there are other mechanisms by which oxytocin mediates Ca^{2+}-sensitisation of the contractile apparatus in human myometrium. Protein kinase C (PKC), which is activated by DAG (a byproduct of the oxytocin-mediated $G\alpha_{q/11}$ cascade described earlier) also modulates MLCP activity either by direct phosphorylation of the phosphatase or by the smooth muscle inhibitor CPI-17. Both ROCK and PKC can activate CPI-17, inducing inhibition of MLCP (Kitazawa et al., 2000).

1.1.4 Contraction at tissue level

The structure of the myometrium is spatially complex and highly specialised. The muscle mass comprises three poorly delineated layers: the stratum supravasculare, an external layer lying next to the perimetrium; the highly vascular stratum vasculare; and the inner stratum subvasculare. The fibre architecture - the structure and organisation of myocytes and collagen fibres - varies within and between these layers. There is significant anisotropy of fibre orientation, particularly within the strata vasculare and supravasculare; the inner subvasculare is the most isotropic layer, consisting primarily of circular orientated fibres (Weiss et al., 2006).

Within each layer of the myometrium, beneath the higher fibre architecture, myocytes and connective tissue are spatially organised. Individual myocytes are integrated into bundles, $\sim 300 \pm 100$μm in diameter; the spindle-shaped myocytes lie parallel to one another within these bundles (Young and Hession, 1999; Young, 2007). The bundles are organised into fasciculi which are 1-2mm in diameter. Connective tissue (including collagen fibres) surrounds myocytes within and between bundles. There is variability in the density of myocytes within bundles and bundles within fasciculi which contributes to the anisotropy of myometrial contractions.

Electrical propagation of action potentials between cells occurs via gap junctions; these are high conductance pathways which increase in number dramatically prior to, during and immediately following parturition (Garfield et al., 1977; Garfield et al., 1978). Gap junctions form the cell-to-cell connectivity required during labour for synchronised phasic contractions; their absence during pregnancy until this point contributes to uterine quiescence. They are formed by a family

of proteins called connexins, with connexin-43 appearing to play the most prominent role in myometrial cell-to-cell coupling during labour (Miyoshi et al., 1998; Döring et al., 2006). Spatial variability in the expression levels of gap junction proteins between different regions of the uterus (Spaery et al., 1999) and sensitivity to hormonal cues (Lye et al., 1993) are indicative of the dynamic and specialised preparation undertaken by the uterus for successful labour.

1.2 Calcium imaging

The central role intracellular calcium has in activating the contractile machinery in myometrium has meant that a key method for investigating the underlying physiological mechanisms is *in vitro* calcium indicator fluorescence imaging of contracting strips of myometrium. Ratiometric calcium-sensitive dyes and force transducers have been used to obtain simultaneous measurements of $[Ca^{2+}]_i$ transients and force in strips of rat (Taggart et al., 1996; Longbottom et al., 2000; Noble and Wray, 2002; Jones et al., 2004) and human (Word et al., 1994; Longbottom et al., 2000; Fomin et al., 2006) myometrium. In spontaneously contracting tissue, when the coupling between $[Ca^{2+}]_i$ and force production remains intact, a close correlation exists between the two measurements with $[Ca^{2+}]_i$ transients peaking before force (Taggart et al., 1996; Noble and Wray, 2002; Jones et al., 2004). However, the $[Ca^{2+}]_i$ signals in these studies reflect an average of tissue-wide $[Ca^{2+}]_i$ activity; while contributing to an understanding of the relationship between global $[Ca^{2+}]_i$ transients and total force production, such measurements do not provide information about $[Ca^{2+}]_i$ signals at the cellular level or the intercellular communication that results in synchronous contractions.

Recently, two studies sought to characterise the spatial and temporal propagation of $[Ca^{2+}]_i$ transients within slices of rat (Burdyga et al., 2009) and human (Bru-Mercier et al., 2012) myometrium. Burdyga et al. (2009) measured calcium indicator transients from individual cells exhibiting non-propagating oscillations. Temporal characteristics of regional $[Ca^{2+}]_i$ activity were also examined, during periods of global $[Ca^{2+}]_i$ activity and tissue contraction. However, the associated motion of the contracting tissue prevented the measurement of calcium indicator signals at the cellular and subcellular level during global activity. In this thesis for the first time we address this limitation in spatiotemporal resolution of calcium images of contracting myometrium caused by to motion artifacts.

In Bru-Mercier et al. (2012), the $[Ca^{2+}]_i$ transients of cells both within the same bundle of myocytes and between two bundles during contraction were com-

pared. The $[Ca^{2+}]_i$ measurements in this study reflect the average of the calcium indicator fluorescence from both the cell and the neighbouring region of tissue. The choice of cells from which calcium indicator fluorescence measurements could be taken was therefore limited: measurements could only be taken from cells positioned at least as far as their maximal displacement away from neighbouring cells. In this work we present a motion-correction method that allows unrestricted single-cell $[Ca^{2+}]_i$ measurements to be taken during the contraction and relaxation of myometrial tissue. In the next section we provide details of the experimental procedures used to acquire the images of contracting myometrial tissue.

1.3 Acquisition of data

Myometrial biopsy specimens were obtained with informed written consent (information leaflet Ref: PTL220705) and approval from the Local Ethics Committee at University Hospital Coventry and Warwickshire (REC-05/Q2802/107) from term-pregnant women ($\geq$37weeks gestation) undergoing elective caesarean section before the onset of labour.

1.3.1 Experimental data

The data processed using our algorithm were obtained using confocal imaging of 200µm-thick myometrial slices and loaded with Fluo-4/AM. Full details are provided in Bru-Mercier et al. (2012). Briefly, each biopsy specimen was trimmed into a strip, which was then ligatured at both ends before being stretched and fixed to the base of a stainless steel tissue holder. From this, 200µm-thick slices were cut. For $[Ca^{2+}]_i$ recording, the slices were incubated in Krebs solution containing 13µM Fluo-4/AM (Invitrogen, Paisley, UK). The loaded slice was placed in a glass-bottomed Petri dish and weighted down with a 250mg slice grid. This was secured on the stage of an inverted microscope equipped with an LSM 510 META confocal scanner and superfused with pre-warmed Krebs solution until stable spontaneous contractions developed. Confocal imaging of Fluo-4 loaded slices was achieved by scanning a 488nm wavelength laser beam focused into a diffraction-limited spot via a Fluar 5$\times$/0.25NA objective lens and recording fluorescence through a band-pass filter (505-530nm) using a photomultiplier tube with a pinhole in front of it. The frame size of the images ranged between 217 $\times$ 412 and 512 $\times$ 512 pixels with the pixel size between 1 and 4.5µm. The recordings were made at a rate of 1 or 2 frames per second (fps) for a recording time of between 12 and 67 minutes. For some of

the datasets the tissue was subject to additional pharmacological protocols: control conditions, nifedipine (1μM), oxytocin (10-100nM) or combinations of the above.

1.4 Image analysis and motion tracking

Motion tracking algorithms have long been applied to biological images, from single cell and particle tracking to tissue-level motion tracking (see Meijering et al., 2012; Chenouard et al., 2014). Quantification of deformation of heart tissue has developed from analysis of two-dimensional motion in echocardiograms (Mailloux et al., 1987; Mailloux et al., 1989) to three-dimensional descriptions of motion in echocardiograms (Suffoletto, 2006) and magnetic resonance (MR) images (Mansi et al., 2011). Recently, software has been developed to track and correct for motion artifacts in *in vivo* two photon calcium indicator imaging of neurons (Greenberg and Kerr, 2009; Tomek et al., 2013). Suffoletto (2006) used speckle-tracking to obtain descriptions of cardiac motion: a technique commonly used in echocardiography that tracks the motion of stable patterns of natural acoustic markers, 'speckles'. In Tomek et al. (2013), the contrast between the intra- and extracellular intensity levels was used to track the motion of the cells. The algorithms implemented in all other cases relied on the assumption that the local intensity of the imaged tissue remained constant throughout the image sequences. The application of motion-tracking algorithms to contracting myometrium, however, is complicated by the fact that there are simultaneous changes in image intensity. In a study investigating intra- and intercellular Ca^{2+} waves in the murine large intestine, Hennig et al. (2002) applied a motion-correction algorithm to calcium indicator fluorescence images of this contracting smooth muscle tissue. In this case, the imaged tissue contained aligned longitudinal muscle cells, and the direction of motion was therefore similar throughout the imaged slice. To our knowledge no algorithms have been developed to correct for motion artifacts in calcium indicator fluorescence imaging of highly contracting tissue in which spatially heterogenous movements occur simultaneously within the field of view.

1.5 Outline of thesis

In this thesis we present a solution to the limitation in spatiotemporal resolution of calcium signals in calcium indicator fluorescence imaging of contracting myometrium caused by motion artifacts. We present a novel motion-correction algorithm that tracks local motion throughout the tissue and allows for the almost

complete removal of motion artifacts. This provides a stabilised calcium signal down to a pixel resolution, which, for the data examined, is in the order of a few microns. As a byproduct of image stabilisation, a complete kinematic description of the contraction-relaxation cycle is also obtained. This contains novel information about the mechanical response of the tissue which will inform biomechanical models of contracting myometrium.

In Chapter 2 we apply three of the most established optical flow-based motion-tracking algorithms to calcium indicator fluorescence images of contracting myometrium: two variants of the Lucas-Kanade algorithm (Lucas and Kanade, 1981) and the Horn-Schunck algorithm (Horn and Schunck, 1981). These algorithms are illustrative of two different approaches to tissue-level motion-correction. The Lucas-Kanade algorithms track the motion of small regions (windows) of tissue within the image, producing trajectories of motion for these irregularly distributed windows. For motion-correction, a method for extrapolating these motion trajectories to estimate the movement across the entire field-of-view is still required. The Horn-Schunck algorithm produces a smooth approximation of the motion within the entire field-of-view and can be used immediately to correct for motion in the images.

In Chapter 3 we present our novel method for motion-correction. This algorithm follows the first approach to motion-correction, namely tracking identifiable landmarks and extrapolating to obtain an approximation of tissue-wide motion. We compare three methods for landmark tracking: fitting a Gaussian function to identified features of high intensity and the simple and extended Lucas-Kanade registration methods detailed in Chapter 2. We find that all three methods for landmark-tracking are successful in reducing motion artifacts when combined with our outlier detection and motion extrapolation methods. We find that the simple Lucas-Kanade algorithm is better suited to our data than the extended version, with a slight increase in performance and a significant increase in speed of performance. We find little difference in the outcome of the Gaussian-fitting and simple Lucas-Kanade methods but differences in the speed of performance, with Gaussian-fitting providing the most efficient method. We demonstrate that our method for motion-correction outperforms the Horn-Schunck method, removing artifacts with no loss of spatial resolution detail.

In Chapter 4 we perform analyses of datasets processed using our motion-correction algorithm and show fine spatiotemporal detail of calcium signals. We show that for the first time unrestricted single-cell calcium measurements can be taken from myometrial tissue slices over multiple contraction-relaxation cycles. We investigate single-cell calcium signals in between contractions and compare single-

cell calcium dynamics in control and oxytocin-treated myometrium.

In Chapter 5 we demonstrate the kinematic properties of contracting myometrium revealed by our method of motion-correction. We identify a characteristic length scale of contracting myometrial tissue slices, in the order of 40-50μm, below which tissue motion is homogeneous. We compare the rough, stochastic paths of tracked landmarks between contraction-relaxation cycles and between different phases of the contraction-relaxation cycle. We illustrate that the data produced by our motion-correction algorithm can be used to compare the spatiotemporal profiles of tissue contraction and calcium signals.

In Chapter 6 we conclude by highlighting the significance of this work in the context of gaining a better understanding of uterine contractility. We draw attention to some further questions posed by our research, the answers to which will contribute to a more complete understanding of the complexities of human labour.

Chapter 2

Application of optical flow-based motion-tracking algorithms

Calcium indicator fluorescence imaging of contracting strips of myometrial tissue is a key method for investigating the underlying physiological mechanisms regulating myometrial contractility. However the spatiotemporal resolution of recordings made from such data is limited due to the motion artifacts in the contracting tissue. Processing the imaging data for motion-correction will significantly increase the amount of information that can be extracted. Motion-tracking and motion-correction algorithms have been applied to a large variety of biological data, including cardiac (Mailloux et al., 1987; Mailloux et al., 1989; Mansi et al., 2011) and *in vivo* imaging of neuronal tissue in awake animals, where the movement of the animal can produce significant motion artifacts (Greenberg and Kerr, 2009). Such algorithms are used both to quantify motion and to improve the spatiotemporal resolution of measurements extracted from the data. In these examples, optical flow-based motion tracking algorithms were used to estimate motion. Optical flow is the distribution of apparent velocities of movement of brightness in an image arising from the relative motion between an observer and the scene. Computer vision techniques for image alignment (the transformation of a deformable template to minimise the difference between the template and an image) and motion tracking frequently involve the computation of optical flow (see Aggarwal and Nandhakumar, 1988; Barron et al., 1994). To our knowledge, optical flow-based motion correction algorithms have not previously been applied to calcium indicator fluorescence imaging of contracting smooth muscle.

The calcium indicator fluorescence imaging data of contracting myometrial tissue poses two particular challenges with respect to motion-tracking techniques:

(i) the data often comprises multiple myocyte bundles of varying alignment contracting simultaneously and producing spatially heterogeneous movements within the field of view; and (ii) the contractile motion in the tissue is accompanied by simultaneous changes in image intensity resulting from the influx and subsequent release of $[Ca^{2+}]_i$. Optical flow-based techniques rely on the assumption that the image intensity will remain constant throughout the image sequence, i.e., that the tissue under a voxel at location **x** and time t will have the same intensity $I(\mathbf{x}, t)$ as the same section of tissue in any later frame:

$$I(\mathbf{x}, t) = I(\mathbf{x} + \Delta\mathbf{x}, t + \Delta t), \tag{2.1}$$

where $\Delta\mathbf{x}$ is the change in location of the tissue and Δt is the time change. Thus any changes in intensity between the same voxel in different frames will be the result of tissue motion relative to the fixed recording equipment. This assumption is reasonable for imaging techniques such as echocardiography and magnetic resonance imaging, and optical flow algorithms have been used to quantify cardiac deformation in datasets obtained using both of these techniques (Mailloux et al., 1987; Mailloux et al., 1989; Mansi et al., 2011). However, for calcium imaging data, where the experimental motivation is to measure changes in intensity caused by local fluctuations in calcium concentration, this condition is necessarily violated. In this work, we attempted to minimise violation of this condition by pre-processing the data for optimum performance.

We tested three of the most established optical flow-based algorithms on our calcium indicator fluorescence imaging data of contracting myometrial tissue: two versions of the Lucas-Kanade algorithm (one restricted to simple translations and one allowing all affine transformations; Lucas and Kanade, 1981) and the Horn-Schunck algorithm (Horn and Schunck, 1981). These two algorithms represent two distinct approaches for correction of tissue-wide motion artifacts in biological images. The Lucas-Kanade registration algorithm can be used to track the motion of small regions (windows) within the image. This results in trajectories of motion for multiple windows within the image frame; extrapolation of the motion of the tracked windows is still required to provide a complete description of the tissue-wide motion. The Horn-Schunck algorithm computes a smooth approximation of the optical flow over the entire image and this information can immediately be used to process the image sequence for motion correction. We developed MATLAB code of the first Lucas-Kanade algorithm (which we will call the *simple* Lucas-Kanade algorithm) and the Horn-Schunck algorithm, and we modified existing MATLAB code of the

extended Lucas-Kanade algorithm developed by Baker and Matthews (2004) for use on our data.

In this chapter, we show the results of applying the simple and extended Lucas-Kanade algorithms to multiple regions within one dataset of contracting myometrial tissue and of using the smooth approximation of optical flow produced by the Horn-Schunck method to correct for motion in the same dataset. In this dataset a slice of human myometrium is imaged over a single contraction induced by 10nM oxytocin. Note that this concentration is significantly higher than the naturally occurring concentration (plasma oxytocin concentration is $\sim 1-2$pM during labour; Thornton et al., 1992), but is typical of the concentrations used to examine its effects on *in vitro* myometrial contractions. We apply the algorithms both to the raw data and to data that has been pre-processed to reduce the effects of the change of image intensity accompanying the contraction. In Chapter 3 we will show that tracking multiple regions is preferable to producing smooth approximation of motion in these images, and that an alternative method of landmark tracking (Gaussian-fitting) is faster than the Lucas-Kanade optical flow-based method of tracking.

2.1 Lucas-Kanade method

2.1.1 Overview of Lucas-Kanade registration algorithm

The Lucas-Kanade image alignment algorithm uses optical flow to align a template image $T(\mathbf{x})$ to an input image $I(\mathbf{x})$, where $\mathbf{x} = (x, y)$ are the pixel coordinates. The goal of the algorithm is to minimise the sum of the squared error between the template and the input images:

$$E = \sum_{\mathbf{x}} \left[I(\mathbf{x} + \mathbf{p}) - T(\mathbf{x}) \right]^2 , \tag{2.2}$$

where $\mathbf{p} = (p_x, p_y)$ describes the translation (optical flow) of the input image relative to the template image. The algorithm uses a Gauss-Newton gradient descent method to iterate over small increments to the parameter vector ($\Delta\mathbf{p}$), minimising the sum of squared differences at each iteration.

The sum of squared differences between the image translated by parameter vector $\mathbf{p} + \Delta\mathbf{p}$ and the template image is expressed:

$$E(\mathbf{p} + \Delta\mathbf{p}) = \sum_{\mathbf{x}} \left[I(\mathbf{x} + \mathbf{p} + \Delta\mathbf{p}) - T(\mathbf{x}) \right]^2 . \tag{2.3}$$

The error is minimised with respect to $\Delta\mathbf{p}$ using a linear approximation to $I(\mathbf{x}+\mathbf{p}+\Delta\mathbf{p})$:

$$\frac{\partial E}{\partial \Delta\mathbf{p}} \simeq 2\sum_{\mathbf{x}} \left(\frac{\partial I}{\partial \mathbf{x}}\right) \left[I(\mathbf{x}+\mathbf{p}) + \Delta\mathbf{p}\frac{\partial I}{\partial \mathbf{x}} - T(\mathbf{x})\right], \tag{2.4}$$

where $\frac{\partial I}{\partial \mathbf{x}} = (\frac{\partial I}{\partial x}, \frac{\partial I}{\partial y})^T$. Equation 2.4 is set to zero and rearranged to solve for $\Delta\mathbf{p}$ at each increment:

$$\Delta\mathbf{p} \simeq \left[\sum_{\mathbf{x}} \left(\frac{\partial I}{\partial \mathbf{x}}\right)^T [T(\mathbf{x}) - I(\mathbf{x}+\mathbf{p})]\right] \left[\sum_{\mathbf{x}} \left(\frac{\partial I}{\partial \mathbf{x}}\right)^T \left(\frac{\partial I}{\partial \mathbf{x}}\right)\right]^{-1}. \tag{2.5}$$

A forwards-additive formulation is used to update the parameter $\mathbf{p}$ at each step:

$$\mathbf{p} \leftarrow \mathbf{p} + \Delta\mathbf{p}. \tag{2.6}$$

Given an initial estimate of displacement $\mathbf{p}$, steps 2.5 and 2.6 are repeated until the estimates of the parameters $\mathbf{p}$ converge. Convergence is typically tested by seeing whether norm of the vector $\Delta\mathbf{p}$ or the error E is less than a threshold ϵ, i.e., $\|\Delta\mathbf{p}\| \leq \epsilon$ or $E \leq \epsilon$.

It can be shown that for an ideal function in 2-dimensions:

$$I(x) = \sin x \tag{2.7}$$

$$T(x) = I(x+p) = \sin(x+p) \tag{2.8}$$

the registration algorithm will converge to the correct p for $|p| < \pi$, i.e., for translations as large as one-half wavelength (Lucas and Kanade, 1981). More generally, the range of convergence is dependent upon the relationship between the high spatial frequencies in the image and the size of the inter-frame displacements.

The Lucas-Kanade algorithm can be used to track local motion by defining the template image as an image patch in the first frame and the input image as the image in subsequent frames. The algorithm is initiated with an estimate for the translation of the image patch between the first and second frames (e.g, $\mathbf{p} = (0, 0)$) and Equations 2.5 and 2.6 are computed iteratively until the two parameters converge. When the parameters $\mathbf{p}$ converge they provide an approximation of the motion of the image patch between the first two frames. These parameters are then used in the initiation of the algorithm to approximate the motion between the first and third frames. This process is repeated for all subsequent frames, with the convergent parameters describing the motion between frame 1 and frame $N-1$ used

to initiate the algorithm for frame N. By identifying multiple image patches (windows) in the first frame and tracking their motion throughout the image sequence we can obtain a description of the motion of multiple regions of tissue. Further developments are required to use these motion trajectories to produce a complete description of the tissue motion; in Chapter 3 we illustrate our novel method for such computations.

2.1.2 Identifying suitable windows for tracking

Windows suitable for tracking were identified using a method described in Tomasi and Kanade (1991) which looks for windows enclosing corners and highly textured regions. The right-hand-side of Equation 2.4 can be rearranged and set to zero to give:

$$\sum_{\mathbf{x}} \frac{\partial I}{\partial \mathbf{x}} \Delta \mathbf{p} \frac{\partial I}{\partial \mathbf{x}} = \sum_{\mathbf{x}} \frac{\partial I}{\partial \mathbf{x}} \left[T(\mathbf{x}) - I(\mathbf{x} + \mathbf{p}) \right]. \tag{2.9}$$

The left-hand-side of Equation 2.9 can be rewritten to give a system of two scalar equations in two unknowns:

$$G \Delta \mathbf{p} = \sum_{\mathbf{x}} \frac{\partial I}{\partial \mathbf{x}} \left[T(\mathbf{x}) - I(\mathbf{x} + \mathbf{p}) \right] \tag{2.10}$$

where G is the 2×2 coefficient matrix:

$$G = \sum_{\mathbf{x}} \frac{\partial I}{\partial \mathbf{x}} \frac{\partial I}{\partial \mathbf{x}}^T. \tag{2.11}$$

A window can be tracked between frames if Equation 2.10 can be solved easily; i.e., if the matrix G is above the noise level of the images and well-conditioned. The eigenvalues of G inform about the texture within our window: two small eigenvalues correspond to a roughly constant intensity profile; one large and one small eigenvalue will be found in windows with a unidirectional profile; two large eigenvalues represent corners and multidirectional patterns that can easily be tracked. We therefore selected windows based on the minimum eigenvalue of their coefficient matrix G.

We used windows of size $(2r+1) \times (2r+1)$ pixels where $r = 3$ was found to be the optimum value for our dataset. Fig. 2.1 illustrates the procedure employed to identify windows in the dataset on which the algorithm was tested. The first frame in the sequence was scanned by a window of $(2r + 1) \times (2r + 1)$ pixels

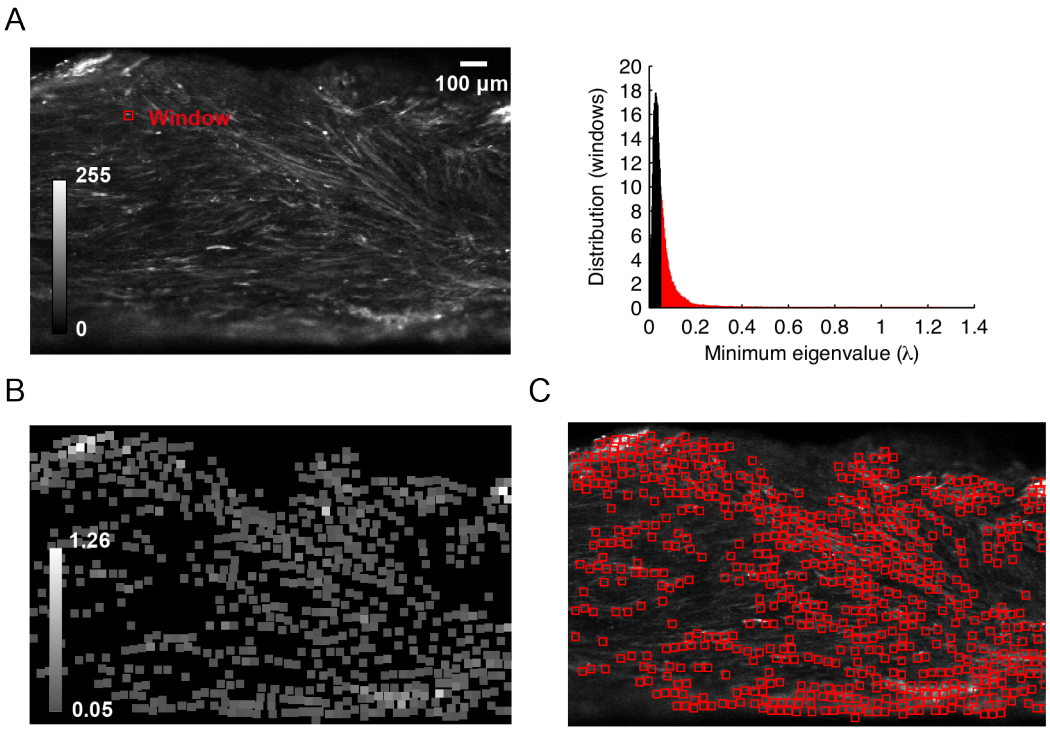

Figure 2.1: **Identifying suitable windows for tracking** (A) The entire first frame (*left*) is scanned by a window of pixel size $(2r+1) \times (2r+1)$ where here $r = 3$. Windows suitable for tracking are identified as those whose minimum eigenvalue (λ) exceeds a threshold value (here $\lambda \geq 0.05$). *Right:* The distribution of eigenvalues for all 3×3 windows in the first frame, with those exceeding the threshold shown in red. (B) Colormap showing the minimum eigenvalues of non overlapping windows selected for tracking ($\lambda \geq 0.05$). (C) First frame with windows identified.

and the minimum eigenvalue ($\lambda = \min(\lambda_1, \lambda_2)$) of each window was calculated (Fig. 2.1A). We sought to identify a threshold value of λ (λ_{th}) such that windows where λ exceeded this threshold were suitable for tracking. We tested a range of values: $\lambda_{th} = 0.01, 0.02, 0.05$ and 0.1. Inspection by eye suggested $\lambda_{th} = 0.05$ to be the optimum threshold value: for values larger than this, large areas contained no tracking windows; for values smaller than this, many additional tracking windows overlapped with windows obtained using a higher threshold and therefore carried little additional information. Windows where λ exceeded $\lambda_{th} = 0.05$ were selected, and where windows overlapped, only the window with the highest valued λ was retained. This process produced the position in pixel coordinates of each $(2r+1) \times (2r+1)$ window and also the positions (x_1, y_1) of the central pixel in the window.

2.1.3 Implementation of the Lucas-Kanade method

We used the Lucas-Kanade registration algorithm to track features within each of our selected $(2r+1)\times(2r+1)$ pixel windows ($r = 3$) over all frames in the sequence. At each frame and for each window, we ran the algorithm until the displacements **p** converged ($E < \epsilon$; we used the root-mean-squared error and used $\epsilon = 0.02$) or for a maximum of fifty iterations. As a result, we obtained the subpixel location of the window's central pixel in each frame as a set of coordinates

$$(x_1, y_1), (x_2, y_2), (x_3, y_3), \ldots, (x_N, y_N) \tag{2.12}$$

where N is the total number of frames over which the window is tracked.

The trajectories of the central pixels of all selected windows during the contraction are shown in Fig. 2.2B (left panel). The trajectories broadly capture the motion of the tissue, and the consistency of motion among spatially local windows (e.g., top left corner) demonstrates the potential of the Lucas-Kanade algorithm as a significant step towards motion correction. Note that we applied the algorithm to a large number of windows and expected that an outlier detection step would be required to remove window trajectories that were not well tracked. For this reason, we did not carry out detailed convergence checks. Inspection by eye revealed that a large number of trajectories appeared to broadly capture the motion of the tissue, and suggested that the algorithm was largely converging to the correct parameter displacements. However, we do see a large number of spurious trajectories, where the motion of windows goes against the flow of motion of tissue in that area; it is likely that for these windows the algorithm has not converged to the correct parameter displacements. Additionally, it is notable that there are a large number of trajectories where 'jumps' have occurred (long, uniform sections representing significant changes in velocity and/or acceleration); here the window originally being tracked is lost and a mismatch in the template matching has occurred. One likely reason for the instability in the tracking is the significant change in intensity of the image which accompanies the contraction.

2.1.4 Histogram specification improves reliability of tracking

In an attempt to increase the reliability of the tracking, we pre-processed the data using histogram specification (Fig. 2.3). Histogram specification is a nonlinear transformation that adjusts the contrast in an image by fitting the image intensities to a prescribed histogram of image intensities. For a reference image I, we wish to

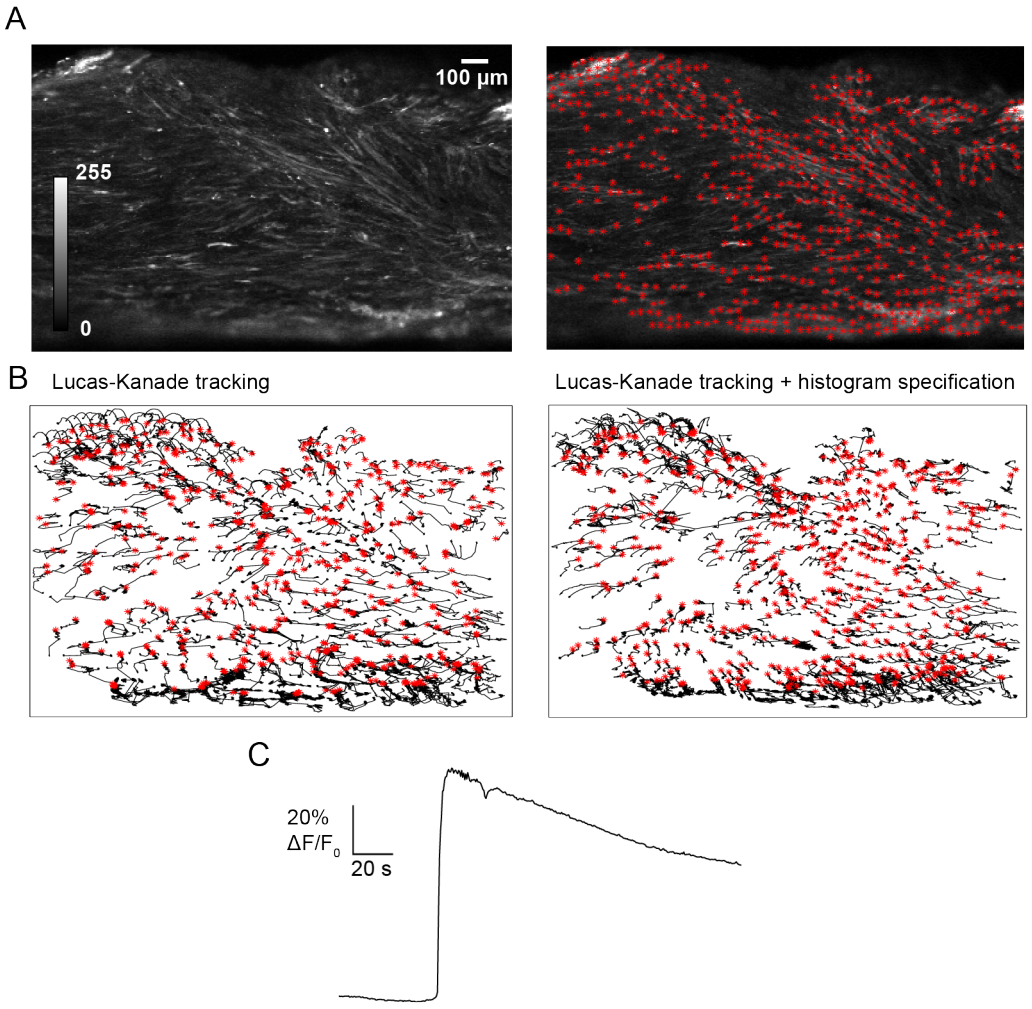

Figure 2.2: **The motion of selected windows is tracked during a single contraction using Lucas-Kanade algorithm** (A) The centre of windows selected as suitable for tracking are identified in the first frame in the sequence (red $*$). (B) The motion of the windows is tracked using the Lucas-Kanade iterative image registration technique. The data show the trajectory of each landmark during a single contraction with the final frame indicated (red $*$) for raw (*left*) data and data pre-processed using histogram specification (*right*). Note the improvement in tracking when data is pre-processed using histogram specification, illustrated by an increased regularity of local tracks. (C) The tissue-averaged change in baseline fluorescence (ΔF) over the course of the imaging sequence.

adjust its histogram $H1$ to match a target histogram $H2$. This is approximately achieved by normalising each histogram to obtain probability histograms and then finding their cumulative distribution functions (CDF): $C1$ and $C2$. Each pixel intensity value in $C1$ is mapped to a single pixel intensity value in $C2$, with the transformation chosen such that the error between the $C1$ and $C2$ is minimised. We selected the intensity histogram from the first image in the sequence as our target histogram and applied histogram specification to all subsequent image frames. In Fig. 2.3B two frames (one taken from a period of low fluorescence prior to a contraction and one from a period of high fluorescence during a contraction) and their associated histograms of intensity distribution are shown for the raw data and the data processed using histogram specification. This process significantly reduced the effect of the global increase in image intensity associated with the contraction, as evidenced by the tissue-averaged baseline fluorescence (ΔF) transient taken from both the raw data and the data pre-processed using histogram specification (Fig. 2.3B).

The trajectories of the central pixels of selected windows for the data pre-processed using histogram specification are shown in Fig. 2.2B (right panel). Comparison between the two panels (raw data and pre-processed data) reveals a significant decrease in the number of jumps and and marked increase in the consistency among spatially localised trajectories when the data is pre-processed using histogram specification. This evidence of increased reliability of the Lucas-Kanade method when the data has been pre-processed is supported by a reduction in the average tracking error (Fig. 2.4). The tracking error is calculated as the root-mean-squared error between the template window in the first frame and the image window in all subsequent frames; this is then averaged over all tracked windows. For the raw data, the error jumps significantly as the change in baseline fluorescence associated with tissue contraction increases. This can be attributed both to the movement of the tissue and the dramatic change in intensity throughout the image, making tracking windows less robust. For the data pre-processed using histogram specification the jump is much less significant, supporting an improvement in the reliability of window tracking.

2.2 Extended Lucas-Kanade method

The Lucas-Kanade algorithm can be extended to registration between the template image $T(\mathbf{x})$ and an input image $I(\mathbf{x})$, where instead of a simple translation, the two images are related by any affine transformation (any transformation that preserves colinearity and the ratio of distances). Baker and Matthews (2004) developed MAT-

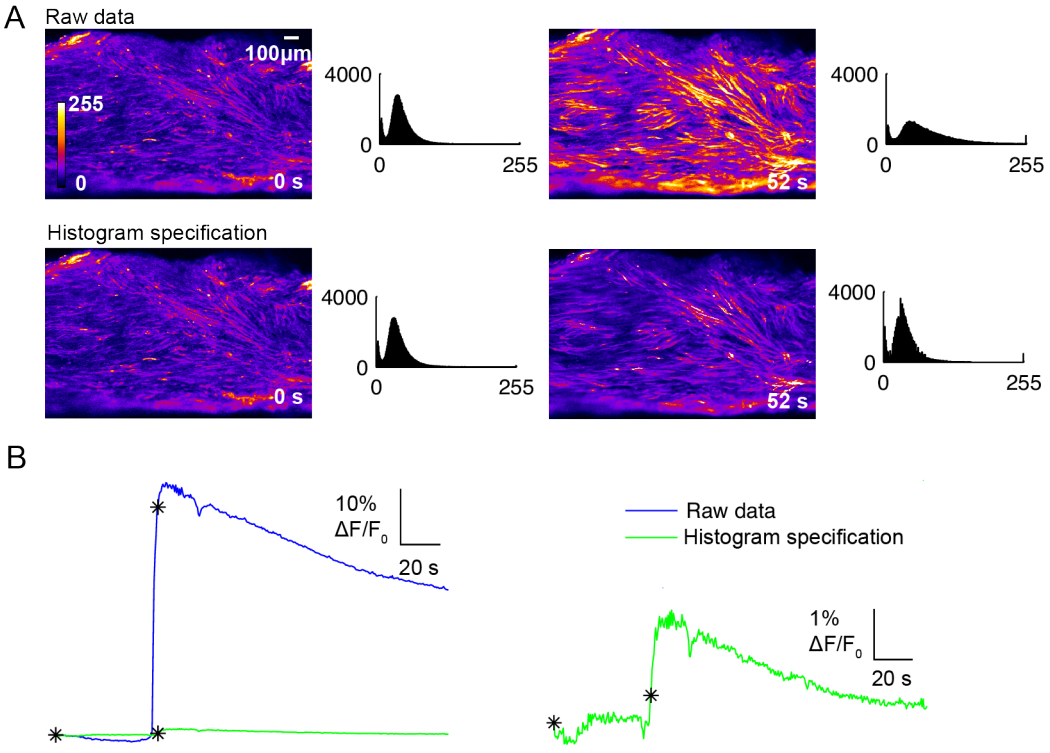

Figure 2.3: **Processing the data using histogram specification reduces the effect of global changes in fluorescence during a contraction.** (A) The change in intensity between a frame showing the tissue prior to a contraction (*left*) and during a contraction (*right*) is significantly reduced when the data is processed using histogram specification (*bottom*) compared to raw data (*top*). The histograms illustrating the distribution of pixel intensities are shown next to each frame. Note that when the data is processed for histogram specification, the two histograms are much more similar than for the raw data. (B) The tissue-averaged change in baseline fluorescence (ΔF) for raw and processed data. The frames used in (A) are indicated (black $*$).

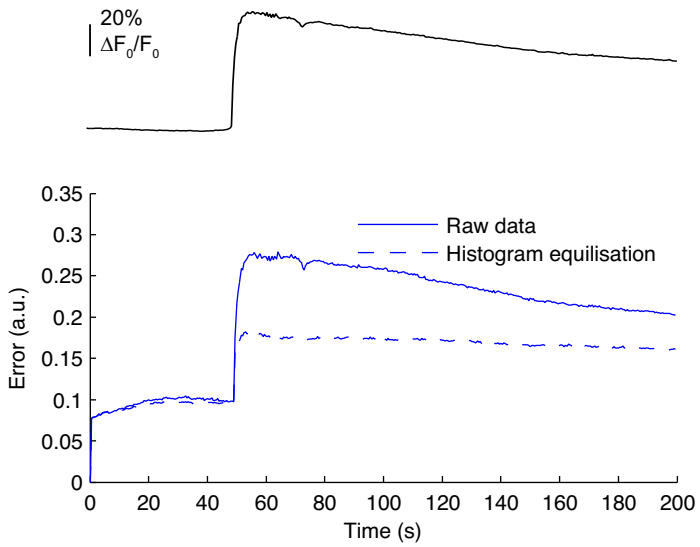

Figure 2.4: **Processing the data using histogram specification reduces the average tracking error** The root-mean-squared error between the template window in the first frame and the image window in all subsequent frames was calculated for all tracked windows. The average error over all windows is plotted (*main plot*) for both the raw data (*solid line*) and the data pre-processed using histogram specification (*dashed line*). The tissue-averaged change in baseline fluorescence (ΔF) for the raw data is shown above. The error for the raw data jumps significantly as the change in baseline fluorescence associated with muscle contraction increases. In the pre-processed data, the jump is less significant.

LAB code for the Lucas-Kanade algorithm permitting all affine transformations. In this development, following Baker and Matthews (2004), the error E in Eqn. 2.2 to be minimised can be written:

$$E = \sum_{\mathbf{x}} \left[I(W(\mathbf{x}; \mathbf{p})) - T(\mathbf{x}) \right]^2 , \tag{2.13}$$

where $W(\mathbf{x}; \mathbf{p})$ denotes the set of permitted warps:

$$W(\mathbf{x}; \mathbf{p}) = \begin{pmatrix} 1 + p_1 & p_3 & p_5 \\ p_2 & 1 + p_4 & p_6 \end{pmatrix} \begin{pmatrix} x \\ y \\ 1 \end{pmatrix} \tag{2.14}$$

parameterised by $\mathbf{p} = (p_1, p_2, p_3, p_4, p_5, p_6)^T$. The six independent parameters in **p** parameterise all affine transformations, including translations, dilations, rotations and shears, and compositions of any of these transformations. For a simple translations only, as permitted in the simple Lucas-Kanade method, all parameters would be set to zero, except p_5 and p_6:

$$W(\mathbf{x}; \mathbf{p}) = \begin{pmatrix} 1 & 0 & p_5 \\ 0 & 1 & p_6 \end{pmatrix} \begin{pmatrix} x \\ y \\ 1 \end{pmatrix} \tag{2.15}$$

An iterative method is again used to find the values of **p** that minimise the error E.

2.2.1 Application of extended Lucas-Kanade algorithm

We modified the code developed by Baker and Matthews (2004) to track the motion of our selected windows to see whether permitting any affine transformation in the registration of the template and image windows improved the results of the tracking. In Fig. 2.5 the trajectories of the selected windows are shown for both raw data (Fig. 2.5B, left panel) and data pre-processed using histogram specification (Fig. 2.5B, right panel). Once again, pre-processing the data for histogram specification increases the consistency of local trajectories and reduces the number of trajectories that appear to jump. However, when comparing Figs. 2.2 and 2.5, spatially neighbouring trajectories appear to be more consistent in Fig. 2.2, suggesting that the performance of the Lucas-Kanade algorithm in tracking windows in the calcium indicator fluorescence imaging of myometrial tissue is optimal when only simple translations are permitted.

It is possible that by introducing extra parameters to the permitted set of

warps in the extended version we may reduce the scale of convergence for some of our windows. At the resolution of the 7×7 pixel windows (i.e., $\sim 30 \times 30$μm), there is not much distortion of the muscle tissue. This is supported by our ability to track landmarks by fitting a Gaussian function to the equivalent area (see Gaussian-fitting algorithm; Section 3.2). By permitting transformations other than simple translations, we may be introducing local minima to which the algorithm converges, thus producing more incorrect trajectories. Convergence analysis of both the simple and extended Lucas-Kanade algorithms applied to our data would allow us to see whether this is the case and this may be valuable further work. However, in this thesis we chose to process the trajectories obtained by each algorithm for outlier detection and judge the performance of each motion tracking method on the stability of the images obtained after the complete description of motion has been inferred. In Chapter 3 we compare the results of both versions of the Lucas-Kanade tracking algorithms with a Gaussian-fitting algorithm. We find that after processing the trajectories using our outlier detection method, there is only a slight difference in the performance of the two methods. However, the simple Lucas-Kanade method is significantly faster than the extended version and the alternative Gaussian-fitting landmark tracking method is more efficient than both Lucas-Kanade algorithms.

2.3 Horn-Schunck method

2.3.1 Overview of Horn-Schunck method

The Horn-Schunck method finds an approximation to the local optical flow everywhere in image by imposing two constraints on the data: (i) the image brightness of a point (x, y) remains constant over time; and (ii) the optical flow in the image varies smoothly everywhere in the image. The first of these constraints is written:

$$\frac{dI}{dt} = 0. \tag{2.16}$$

The method finds the error (E_c) between the image and this assumption of constant intensity:

$$E_c = I_x u + I_y v + I_t, \tag{2.17}$$

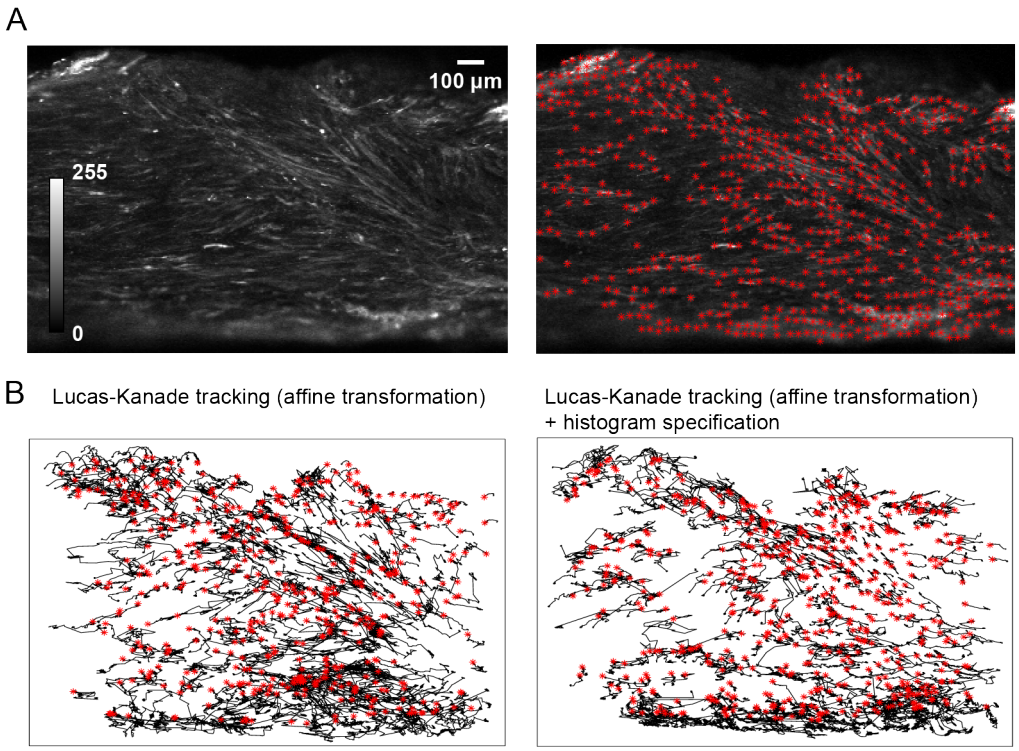

Figure 2.5: **The motion of selected windows is tracking during a single contraction using Lucas-Kanade algorithm with affine transformations** (A) The centre of windows selected as suitable for tracking are identified in the first frame in the sequence (red $*$). (B) The motion of the windows is tracked using the Lucas-Kanade iterative image registration technique allowing for affine transformations. The data show the trajectory of each landmark during a single contraction with the final frame indicated (red $*$) for raw data (*left*) and data pre-processed using histogram specification (*right*). Note that compared with the trajectories of windows tracked using the Lucas-Kanade algorithm restricted to translations (Fig. 2.2), there appears to be less regularity in the local trajectories of windows tracked using affine transformations.

where I_x, I_y and I_t are the partial derivatives of the image (I) with respect to x, y and t respectively, and

$$u = \frac{dx}{dt} \quad \text{and} \quad v = \frac{dy}{dt} \tag{2.18}$$

describe the optical flow of the image. The right-hand-side of Eqn. 2.17 is found by applying the chain rule to the left-hand-side of Eqn. 2.16.

The second constraint (that of smoothness) is expressed as a minimisation of the sum of the squares of the Laplacians of the x- and y-components of the optical flow:

$$E_s^2 = \nabla^2 u + \nabla^2 v, \tag{2.19}$$

where

$$\nabla^2 u = \frac{\partial^2 u}{\partial x^2} + \frac{\partial^2 u}{\partial y^2} \quad \text{and} \quad \nabla^2 v = \frac{\partial^2 v}{\partial x^2} + \frac{\partial^2 v}{\partial y^2}. \tag{2.20}$$

The method seeks to minimise a total error:

$$E^2 = \alpha^2 E_s^2 + E_c^2, \tag{2.21}$$

where α is a weighting factor that scales the global smoothness of the flow: larger values of α lead to a smoother flow. Mailloux et al. (1987) used a value of $\alpha = 10$ in their analysis of echocardiograms; we tested a number of values ($1 \leq \alpha \leq 50$) and found $\alpha = 10$ to be a suitable value for our myometrial data. For smaller values of α the image became significantly distorted by noise; for higher values the motion was not well captured. Minimisation of the error in Equation 2.21 is achieved by differentiating E^2 with respect to u and v and setting each to zero to give two equations in u and v, where approximations for the partial derivatives and the Laplacians are used. An iterative method is then used to compute the optical flow estimates (u, v).

2.3.2 Application of Horn-Schunck method to correct for motion artifacts

The Horn-Schunck method estimates the optical flow at all points of the image between two image frames, which here is an approximation of the motion of the tissue. We applied the Horn-Schunck algorithm to each consecutive pair of frames in the same dataset as used in Sections 2.1 and 2.2 to obtain an obtain an estimate of the

tissue deformation (Fig. 2.6). The first condition of the Horn-Schunck method assumes that the brightness in all areas of the tissue remains constant throughout the image sequence. As for the Lucas-Kanade method, we found that pre-processing the images using histogram specification significantly improved the performance of the algorithm. The second constraint is based on the assumption of an underlying continuous image with smooth spatial derivative. This suggests that the motion may be more reliably tracked if the images are also smoothed prior to processing with the Horn-Schunck method. We further pre-processed our image sequence testing a variety of sizes of mean filters, pixel size $(2r+1)\times(2r+1)$ (Fig. 2.6A). We found that there was a payoff with the radius of the filter, r: for larger r and smoother images, the motion was better captured at a larger spatial resolution, but the finer spatial detail was lost; for smaller r, features of small spatial resolution (e.g., myocytes) were better retained, but the motion was less well captured.

In Fig. 2.6, the motion of the tissue over the contraction calculated using the Horn-Schunck method is shown for images pre-processed using histogram specification and a mean filter with radius $r = 3$. This was found to be the optimum size of filter for reliable tracking and retention of fine spatial resolution. For clarity, the trajectories in Fig. 2.6B are only shown for every 20th pixel. The algorithm clearly detects some of the tissue deformation; to assess how reliable this motion detection is we can use the trajectories to construct a motion-corrected image sequence. This is done by mapping the intensity value found at a position in any later frame back to its point of origin in the first frame.

In Fig. 2.7 a magnified subsection of images of contracting tissue taken at four different time points is shown for the raw data (Fig. 2.7A) and the data processed for motion-correction (Fig. 2.7B, C). The images processed for motion-correction have been pre-processed using histogram specification only (Fig. 2.7B) and histogram specification and a mean filter, pixel size 7×7 (Fig. 2.7C). Four regions of interest encompassing myocytes in the first frame have been labelled to highlight the motion of the tissue in the raw data and the reduction of motion in images processed using the Horn-Schunck algorithm. It is clear that the motion artifacts are reduced when the Horn-Schunck method is applied, and that the reduction is optimal when the data is pre-processed using both histogram specification and smoothing (Fig. 2.7C). However, it is also clear that the Horn-Schunck method produces its own artifacts: the reduction in motion is accompanied by blotching of high resolution detail. This high resolution smudging is particularly evident in the areas of high intensity above and below the four labelled myocytes (Fig. 2.7).

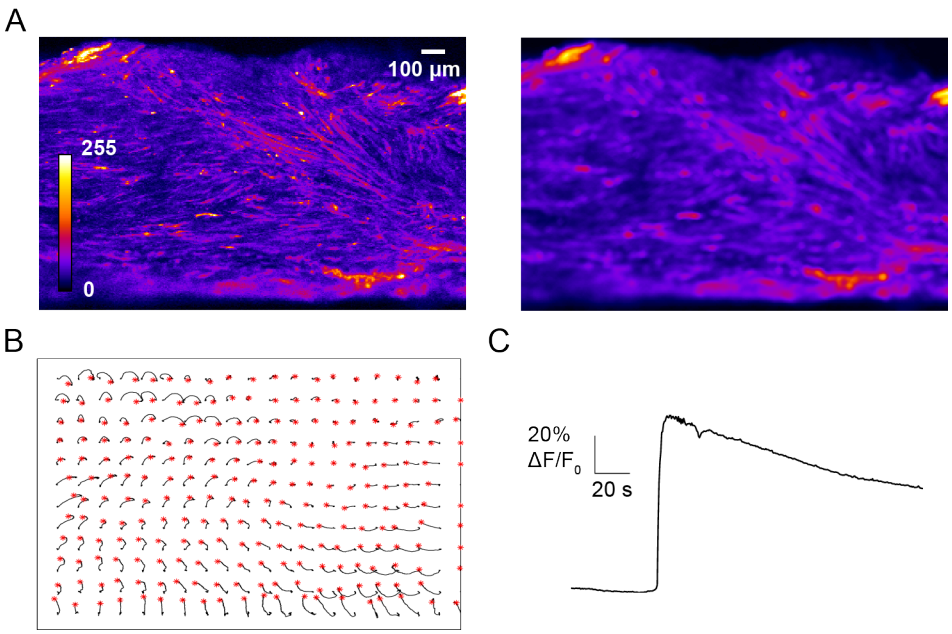

Figure 2.6: **The contractile motion of the myometrial tissue during a single contraction is estimated using the Horn-Schunck method** (A) The images are processed using histogram specification (see Fig. 2.3) and a mean filter of pixel size $(2r+1) \times (2r+1)$, where here $r = 3$. The first frame in the sequence is shown, both raw image (*left panel*) and image processed with mean filter (*right panel*). (B) The motion of the tissue is estimated using the Horn-Schunck method to pixel resolution. Note that for clarity tracks are only shown for every 20th pixel (separation of 90µm). (C) The tissue-averaged change in baseline fluorescence (ΔF) for the image sequence.

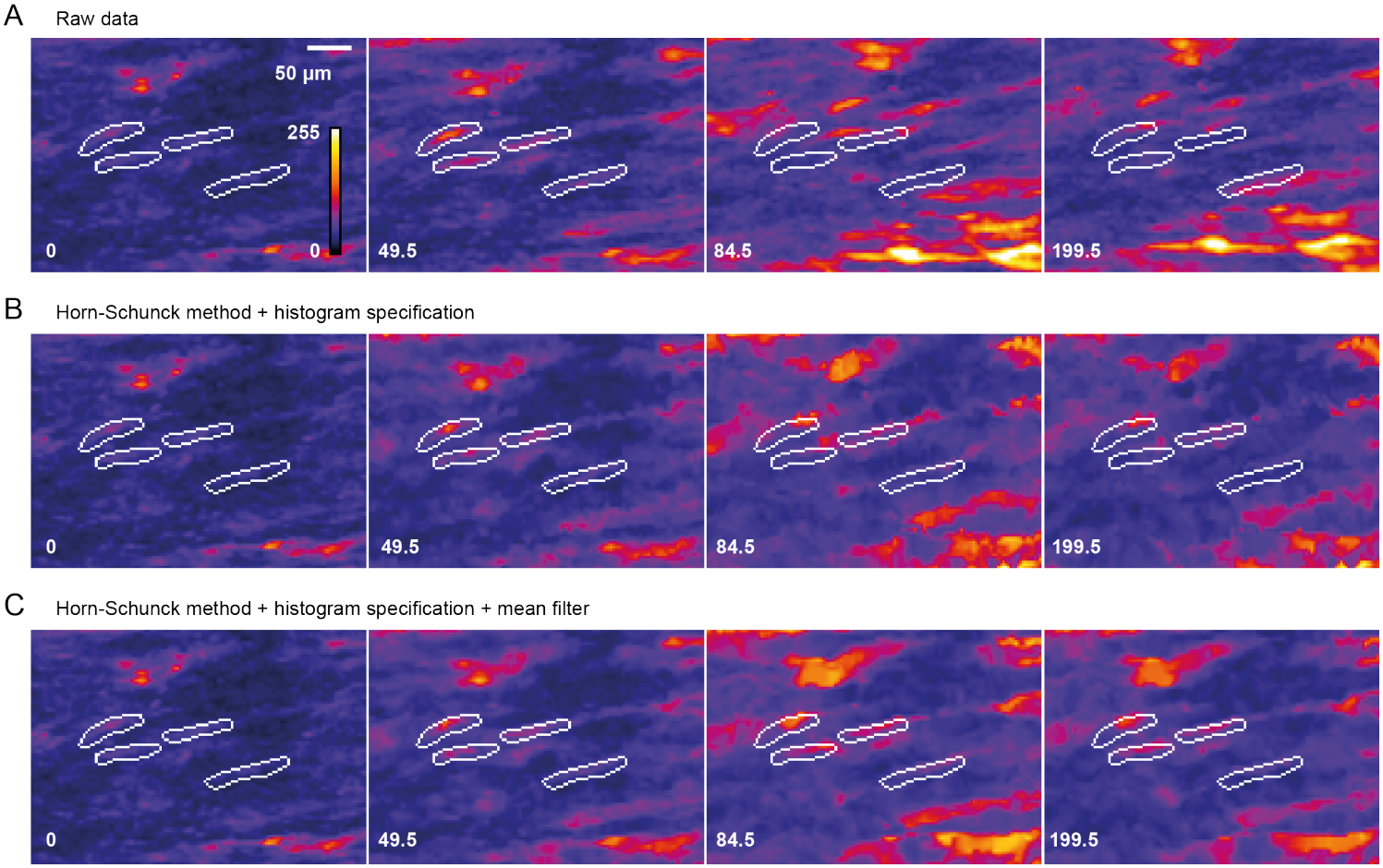

Figure 2.7: **Motion artifacts reduced using Horn-Schunck motion-correction but fine spatial detail lost** Magnified subsection of imaged tissue taken at times indicated (s) showing raw images (A) and images processed using Horn-Schunck motion-correction algorithm with histogram specification (B) and histogram specification and smoothing with mean filter of pixel size 7×7. Four regions of interest (ROIs) encompassing myocytes have been labelled to illustrate motion-reduction. Motion-reduction is accompanied by blotching of fine resolution detail using Horn-Schunck method (see particularly areas of high intensity above and below labelled myocytes).

Chapter 3

Gaussian-fitting motion-correction algorithm

In Chapter 2 we presented the results of applying three different optical flow-based motion-tracking algorithms to calcium indicator fluorescence imaging data of contracting myometrial tissue. These motion-tracking algorithms fell into two different categories in terms of the way they can be used to obtain a complete description of motion within the entire field-of-view (in this case the tissue-wide motion).

In the first category, the Horn-Schunck method (Horn and Schunck, 1981) produces a smooth approximation of the optical flow over the entire field-of-view and this information can immediately be used to process the image sequence for motion correction (Figs. 2.6, 2.7). We illustrated that the Horn-Schunck method reduced the motion artifacts in the images of contracting myometrial tissue but that this came at a cost: an accompanying loss of fine spatial resolution detail. Therefore although processing the data with the Horn-Schunck method improves the spatiotemporal resolution of recordings of contracting myometrium, at high spatial resolution ($\lesssim$50μm), the structure of the tissue was compromised by smudging.

In the second category, the simple and extended Lucas Kanade algorithms (Lucas and Kanade, 1981) track the motion of selected landmarks (windows) within the image (Figs. 2.1, 2.2, 2.5). These landmarks are unevenly distributed within the image frame, and the resulting trajectories need to be extrapolated to all neighbouring pixels to produce a complete description of the tissue motion. We showed that the motion trajectories of many of the landmarks produced using the Lucas-Kanade algorithms appeared to capture the contractile deformation of the tissue, and this was optimised when the data was pre-processed using histogram equilisation. The simple Lucas-Kanade algorithm appeared to be better suited for our

data than the extended algorithm, as evaluated by consistency of spatially local trajectories and number of obvious jumps where the velocity and/or acceleration of a landmark is inconsistent with neighbouring landmarks. However, a number of outliers were still evident in this data; a method for detecting and removing these outliers would be required before extrapolating the motion to produce a complete description of tissue-wide motion.

In this chapter we present an alternative novel method for processing the calcium indicator fluorescence imaging data of contracting myometrial tissue. This method falls into the second category of motion-correction algorithms: irregularly distributed landmarks are selected in the first frame and tracked throughout the series of images. In this method, the shape rather than the intensity of landmarks is compared throughout the series of frames: circular structures are identified and their motion is tracked by scanning the local area for the best fit to a Gaussian function in each frame. These features (which are likely leukocytes) were selected in part because inspection by eye suggested that their fluorescence, and therefore structure, remained reasonably stable throughout the image sequences. However, it should be noted that their structure as viewed in the two-dimensional plane will also be dependent on the structure of the locally surrounding tissue. The assumption that the structure of the feature remains constant is a good approximation when the tissue surrounding the landmarks does not exhibit significant changes in thickness over the course of a contraction-relaxation cycle; e.g., when the feature is located in passive connective tissue. The assumption may fail for landmarks located in highly contractile regions, e.g., within myocyte bundles, if significant and heterogeneous changes in the thickness of the surrounding tissue during contraction alter the image we see in two-dimensions. The two-dimensional projection of the landmark may then become altered or partially obscured as a result of the crumpling of the surrounding tissue. Empirically we found that it was a good approximation to assume that the structure of these features remained unchanged throughout contraction-relaxation cycles, and were well tracked by Gaussian-fitting.

We developed a complete method for motion correction which identifies landmarks, tracks their motion, removes outliers and extrapolates the motion to produce a complete description of tissue motion. Here we present details of the algorithm and demonstrate its superiority in removing artifacts with no loss of fine spatial details when compared with the Horn-Schunck method. We compare the simple and extended Lucas-Kanade methods of tracking landmarks with that of Gaussian-fitting by processing the motion trajectories produced using the Lucas-Kanade methods with our novel methods for outlier detection and extrapolation to

give motion of all neighbouring pixels. We demonstrate that the extended Lucas-Kanade method takes much longer to track landmarks than the simple version and is slightly less effective at removing motion artifacts. We show that the both the Gaussian-fitting method and the simple Lucas-Kanade optical flow-based method successfully remove motion artifacts from calcium indicator fluorescence imaging data of slices of contracting myometrial tissue when combined with our outlier detection and motion extrapolation methods, but that the Gaussian-fitting method is faster. We processed over twenty datasets of myometrial slices undergoing multiple contraction-relaxation cycles under various pharmacological conditions using our method and found an almost complete removal of motion artifacts in all. A number of these datasets are presented in the description of the algorithm.

3.1 Overview of Gaussian-fitting motion-correction algorithm

The main steps of the algorithm are shown in Fig. 3.1 and comprise: (i) landmark identification by band-pass filtering the image to emphasise circular structures of size 30μm; (ii) tracking the motion of each landmark between frames for the entire image stack; (iii) removing outlier landmarks; and (iv) extrapolating the motion of landmarks to all neighbouring pixels to yield a complete description of the tissue motion. This requires identifying a characteristic length scale below which tissue motion is homogeneous. This tissue-motion description constitutes the calcium-signal timeseries and kinematic data - position, velocity and acceleration as functions of time - for the tissue under each pixel in the initial frame.

3.2 Identification of landmarks

In all datasets circular-shaped features of $\sim$15μm radius were present and displaced predictably with little change in shape over contraction-relaxation cycles, though their fluorescence intensity changed markedly (Fig. 3.2A). These landmarks were emphasised by bandpass-filtering each frame to suppress high frequency noise and structures with low spatial frequency. The bandpass filter operates in the frequency domain; the discrete Fourier transform is (DFT) of the image is computed using a fast Fourier transform (FFT) algorithm and this is then filtered using a high pass and low pass Gaussian filter. The FFT algorithm requires a square $N \times N$ input image, where N is a power of 2. Thus, we create an $N \times N$ image using our

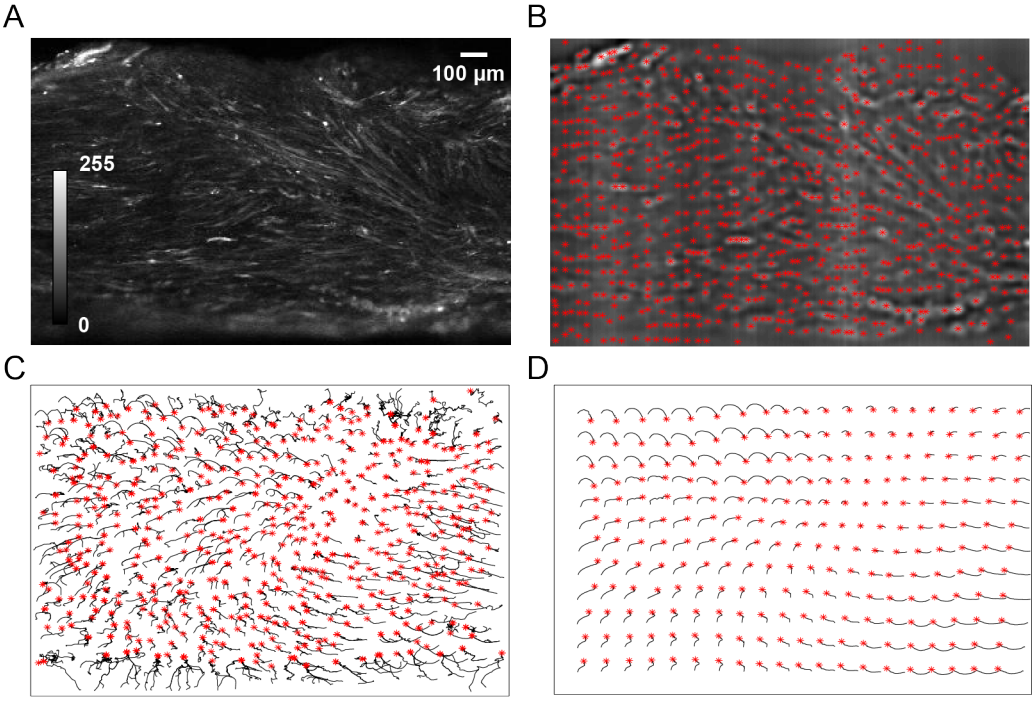

Figure 3.1: **Overview of the motion correction algorithm** (A) Raw fluorescence image of a Fluo-4 loaded myometrial slice. (B) The raw image is bandpass-filtered to emphasise circular structures with radii $\sim$15µm. Landmarks suitable for tracking are identified (red $*$) as those having a high correlation with a two-dimensional Gaussian function. (C) The landmarks are then tracked by placing a small window over each landmark and looking within the window in the next frame for the displaced landmark. The data show the trajectories during a single contraction with the final frame indicated (red $*$). The trajectory of each landmark is tested for regularity and any outliers are removed from the data set. (D) The motion of the landmarks is then extrapolated to neighbouring pixels to provide a complete description of the tissue-wide motion. The extrapolation procedure also identifies a characteristic length-scale below which tissue motion is homogeneous. Note that for clarity tracks in panel D are only shown for every 20th pixel (separation of 90µm).

$m \times n$ image $I(x, y)$ and padding the edges with mirror images of I. $\hat{I}$, the DFT of the padded image I is calculated:

$$\hat{I}(u, v) = \mathcal{F}(I(x, y)) = \sum_{x=1}^{N} \sum_{y=1}^{N} I(x, y) \exp\left(-2\pi i(\frac{ux}{N} + \frac{vy}{N})\right). \tag{3.1}$$

The high pass (H_h) and low pass (H_l) filters are computed:

$$H_h(u, v) = 1 - \exp\left(-D^2(u, v)/2D_h^2\right) \tag{3.2}$$

$$H_l(u, v) = \exp\left(-D^2(u, v)/2D_l^2\right), \tag{3.3}$$

where D is the distance of pixel (u, v) from the origin and D_h, D_l are the cut off frequencies of the high- and low-pass filters respectively ($D_l > D_h$). For the majority of our datasets, with pixel width representing between 3.4µm and 4.5µm, we found that the landmark-to-noise ratio was maximised when the parameters were set such that structures between 10 and 18 pixels were highlighted in the bandpass filter (i.e., $D_h = \frac{10}{N}$, $D_l = \frac{18}{N}$). Note that our landmarks have diameter ~ 30µm (between 7 and 9 pixels), and this would suggest that a smaller value for D_h would be preferable. We tested a number of values for both D_h and D_l and and inspection by eye suggested that our landmarks were best identified using the thresholds indicated above. This may be due to filter roll-off; i.e., there is a gradient at the upper and lower boundaries of the filter, meaning that the frequencies lower than D_h and higher than D_l are also attenuated.

The bandpass-filtered image in the frequency domain $\hat{I}_{bp}$ was calculated by multiplying the image by the two filters:

$$\hat{I}_{bp}(u, v) = \hat{I}(u, v) H_h(u, v) H_l(u, v), \tag{3.4}$$

and the inverse FFT was used to obtain the filtered image in the spatial domain (I_{bp}):

$$I_{bp}(x, y) = \mathcal{F}^{-1}(\hat{I}_{bp}(u, v). \tag{3.5}$$

The first band-passed frame was then scanned in its entirety by a square window of size $(2r + 1) \times (2r + 1)$ pixels (with r chosen so the window was large enough to contain one landmark only: typically $r = 3$ was sufficient). Each window was normalised such that the sum of all pixel intensities was equal to one and

compared to a discrete approximation to a 2D Gaussian function of the form

$$G(x,y) = B \exp\left(-\frac{x^2+y^2}{2\sigma^2}\right) \quad x,y \in \mathbb{Z} \quad x,y \in [-r,r] \tag{3.6}$$

with parameters fixed ($\sigma = (2r+1)/3$, B a normalisation constant set such that $\sum_x \sum_y G = 1$). Note that for values of $x, y > 3\sigma$, the Gaussian function is approximately zero, suggesting a value of $\sigma = r/3$. However, we found that using a slightly larger value for sigma allowed good identification of landmarks. It was straightforward to identify windows containing landmarks by the quality of the correlation between the image contained with the window and the Gaussian function (see distribution in Fig. 3.2B). This was measured by calculating the correlation coefficient $r_{W,G}$ between the window W and the discrete approximation to the Gaussian function G:

$$r_{W,G} = \frac{\sum_x \sum_y (G-\bar{G})(W-\bar{W})}{\sqrt{\sum_x \sum_y (G-\bar{G})^2 (W-\bar{W})^2}}, \tag{3.7}$$

where

$$\bar{W} = \frac{1}{(2r+1)^2} \sum_x \sum_y W, \quad \bar{G} = \frac{1}{(2r+1)^2} \sum_x \sum_y G. \tag{3.8}$$

Windows enclosing landmarks had correlation coefficients close to one and those not enclosing landmarks had correlation coefficients close to zero, yielding a bimodal distribution of correlation coefficients. A two-component Gaussian mixture-model was fitted to the correlation-component distribution (see blue lines, distribution Fig. 3.2B). A Gaussian mixture-model is a probabilistic model that assumes that all data points are generated from a mixture of Gaussian distributions with unknown parameters. An expectation-maximisation iterative algorithm is used to fit a Gaussian mixture model to data: briefly, randomly sampled data points are used to provide initial parameter estimates; for each data point the probability of being generated by each distribution is calculated (expectation); parameter values are adjusted to maximise the likelihood of the data given the distribution assignments. We assume that our correlation coefficient data can be generated as a mixture of two Gaussian distributions, and select the subpopulation of landmarks associated with the distribution with the higher mean value for tracking. The same landmark will be contained by a number of overlapping windows, but only the window with the landmark placed most centrally was retained. After this last step the positions $x_1,\ y_1$ of each landmark in frame 1 are known (Fig. 3.2C) as is the position in pixel

coordinates of each $(2r+1)\times(2r+1)$ window centred on the landmarks.

The spatial distribution of landmarks identified in the dataset in Fig. 3.2 is illustrated in Fig. 3.3, where the x-axis shows the distance from a landmark to its nearest neighbour. The first sharp peak at $\sim$18µm (4 pixels) corresponds to the minimum distance permitted between landmarks: landmarks situated closer than this distance were considered to overlap and therefore removed. This may indicate that the landmarks (which are most likely leukocytes) can be found in clusters in human myometrial strips taken at term. It is also possible however that this peak is an artifact of the bandpass filter. Most landmarks are located between 18 and 50µm of their nearest neighbour.

3.3 Tracking of landmarks

A square 7×7 pixel window around each landmark was selected in frame 1, and the new landmark position x_2, y_2 in frame 2 was located by fitting a 2D Gaussian of the form:

$$G(x,y) = A + B \exp\left(-\frac{(x-x_2)^2+(y-y_2)^2}{2\sigma^2}\right) \tag{3.9}$$

to the frame 2 data enclosed within the frame 1 window. The parameters A, B, σ,x_2, y_2 were optimised for the fit. Once this had been achieved, the position of the window was updated if required. This process was repeated for all landmarks and for all subsequent frames to obtain the sub pixel location of a landmark in each frame as a set of coordinates

$$(x_1,y_1),\ (x_2,y_2),\ (x_3,y_3),\ \ldots,\ (x_N,y_N) \tag{3.10}$$

where N is the total number of frames over which the landmarks are tracked.

3.4 Removal of outliers

3.4.1 The challenge of identifying outliers

The coordinates describing the time-dependent location of each tracked landmark over the course of a contraction-relaxation cycle need to be filtered to remove outliers. In Fig. 3.4, the unfiltered trajectories of all landmarks tracked over a contraction-relaxation cycle are shown for one dataset. The motion of the tissue over a single

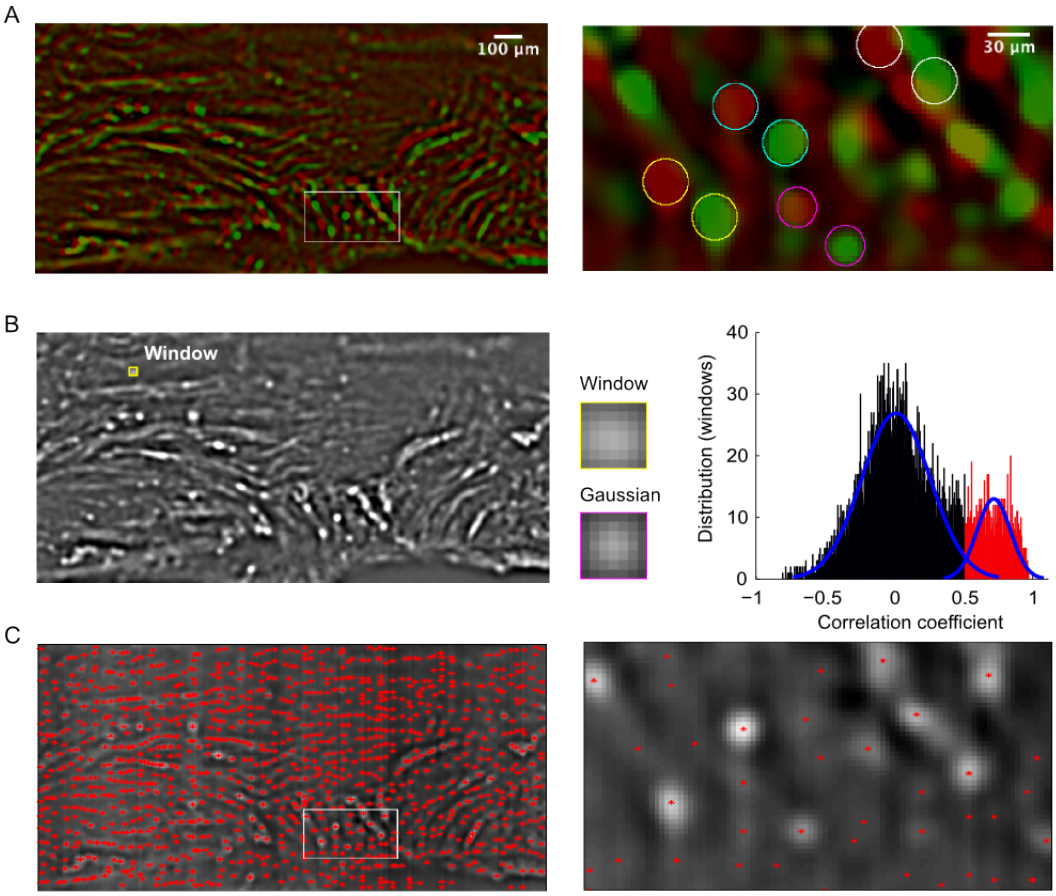

Figure 3.2: **Identification of landmarks for tracking** (A) Frames are band-pass filtered to emphasise small cell bodies (landmarks) with radii $\sim$15µm which were present in all data sets. Two frames have been superimposed to illustrate the motion but constancy in distribution of landmarks for the first frame in which the tissue is relaxed (*red*) and a later frame in which there is a contraction (*green*). Four landmarks have been highlighted in colour to indicate their respective positions in the relaxed and contracted frames. (B) The entire first frame is scanned by a window of pixel size $(2r+1)\times(2r+1)$ where here $r=3$. The quality of fit of each window to a 2D Gaussian (see insets) is then evaluated by their crosscorrelation. The distribution of correlations for each window in the first frame comprises two components - one for windows not containing landmarks (black) and one for windows with landmarks (red). These latter windows are selected by fitting the total correlation distribution to two normal distributions (blue curves). (C) The initial frame with landmarks identified (red $*$).

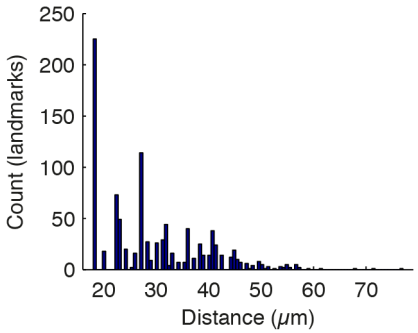

Figure 3.3: **Spatial distribution of landmarks** Histogram of distance of landmarks to nearest neighbour for data in Fig. 3.2.

contraction-relaxation cycle is spatially heterogeneous, meaning that characteristics of outlier trajectories will vary across the slice. This is highlighted in the two magnified panels in Fig. 3.4C: the motion trajectories vary dramatically between the two panels, and also more gradually within each panel. The algorithm makes no distinction between periods of global motion and quiescent periods, but this contributes to the difficulty in automating the identification of outliers, as characteristics of local motion, such as velocity, differ significantly between the two distinct phases.

The contracting muscle tissue remains in tact throughout all contraction-relaxation cycles, i.e., the motion we see is that of a continuous medium. For this reason we expect to see good correlation in the movement between locally neighbouring trajectories. At both high and low temporal resolution the direction of locally neighbouring trajectories should be consistent, and where the trajectories of landmarks violate this consistency, we assume that they have not been well tracked; i.e., are outliers that should be removed. A certain amount of high temporal resolution noise, due to the recording equipment and the tracking method, is to be expected; some of this will be smoothed out during the extrapolation process. In the left magnified panel in Fig. 3.4C the consistency in shape of locally neighbouring trajectories and the smooth change in shape across the panel suggests that the majority of these landmarks have been well tracked. A notable exception can be seen in the top left of the panel; here we appear to see the trajectories of two or more landmarks; one whose trajectory is consistent with neighbouring landmarks and one whose overall motion goes against that of nearby landmarks.

In the right magnified panel in Fig. 3.4C we see a number of trajectories that violate the consistency of local motion. The partially shown trajectory in the bottom left goes against the flow of motion of neighbouring trajectories. Additionally, there appear to be a number of areas where the trajectories of multiple landmarks meet;

i.e., a trajectory whose shape is consistent with neighbouring landmarks is overlaid with motion that is inconsistent. Close examination of these trajectories reveals that they often represent one well tracked landmark, and one or more trajectories where the landmark has not been well-tracked and at some point the algorithm has jumped to track a new landmark.

It should be noted that the image frame captures a two-dimensional view of a three-dimensional object. The assumption of continuous motion in the two-dimensional image frame is a good approximation when there is little change in the thickness of the tissue. However, this approximation will fail in highly contractile regions of the tissue, i.e., myocyte bundles, where the contraction of the cells causes significant and heterogenous changes in the thickness of the tissue. In such regions we can expect that there will be breaks in the continuous motion represented in two-dimensions. The primary goal of the algorithm in this work is to best approximate the motion of the tissue over the entire image frame, thus improving the spatial resolution of calcium signals that can be extracted. For this purpose, it was found to be better to remove false positive trajectory outliers than to retain false negative outliers; an erratic and badly tracked landmark has a significant impact on the stability of the resulting images. This motivation underlies the development of the outlier detection method detailed below; however we recognise that the process used necessarily discards a significant amount of information. In Chapter 5 we illustrate some of the kinematic information that is contained within the description of tissue motion. Here we begin to examine characteristics of the motion trajectories. One future direction for development of this work would be to explicitly consider the trajectories as two-dimensional representations of three-dimensional motion to investigate contractile properties of the tissue in all three dimensions.

A common method for detecting spurious vectors in particle image velocimetry (PIV) data is the local median test (Westerweel, 1994; Westerweel and Scarano, 2005). PIV is a method for the optical visualisation of flow in fluids: tracer particles are introduced into the fluid and their motion is used to obtain properties of the flow such as velocity measurements. In the local median test, a scalar residual (r^*) describing a normalised difference between each displacement vector over a single frame and the median displacement of its neighbouring displacement vectors is found. Landmarks for which this residual exceeds a certain threshold (r_{th}) are considered to be outliers.

We wanted to see whether the local median test could successfully identify outliers in our datasets. As described in Section 3.3, the Gaussian-fitting tracking method locates the position of each landmark to subpixel resolution. This means

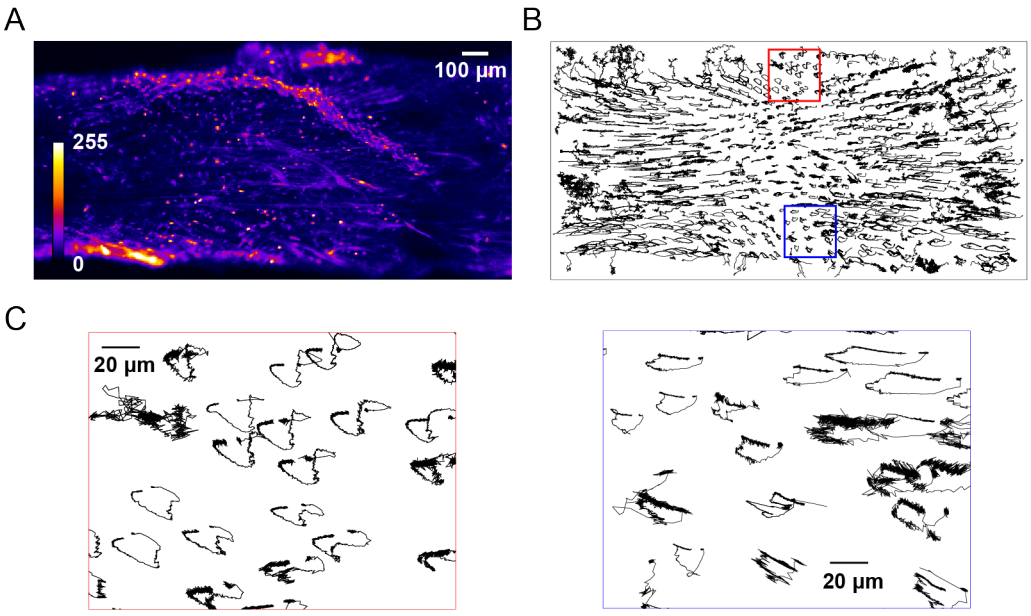

Figure 3.4: **Motion trajectories of tracked landmarks must be filtered for outliers** (A) Raw fluorescence image of a Fluo-4 loaded myometrial slice. (B) Trajectories of landmarks from (A) tracked over a single contraction-relaxation cycle, including outliers. (C) Magnification of two panels highlighted in (B).

that at high temporal resolution (i.e, between two consecutive frames) the motion trajectories are noisy even after smoothing; this is illustrated in Fig. 3.5D, where the raw trajectory (left panel) and the smoothed trajectory (right panel) of a faithfully tracked landmark over a contraction-relaxation cycle is shown. The trajectories were smoothed using local linear regression: for each data point a linear function is fitted to s neighbouring points using a weighted least squares method, with more weight given to points closer to the data point being considered. For our data, we smoothed the trajectories independently in each dimension using local linear regression and $s = 5$. In Fig. 3.5B, the velocity vectors of all landmarks between two consecutive frames during the tissue contraction further illustrate the high temporal resolution noise in our data. This high temporal resolution noise means that an outlier detection method based on inter-frame motion will not be effective in removing spurious motion trajectories in our data.

We tried implementing a low temporal resolution adaptation of the local median test on our data (Fig. 3.7). Instead of using inter-frame displacement vectors, we looked at the total displacement vectors between the first and last frames for all landmarks over a single contraction-relaxation cycle (Fig. 3.7B). For each landmark, we then computed the median total displacement vector of all neighbouring

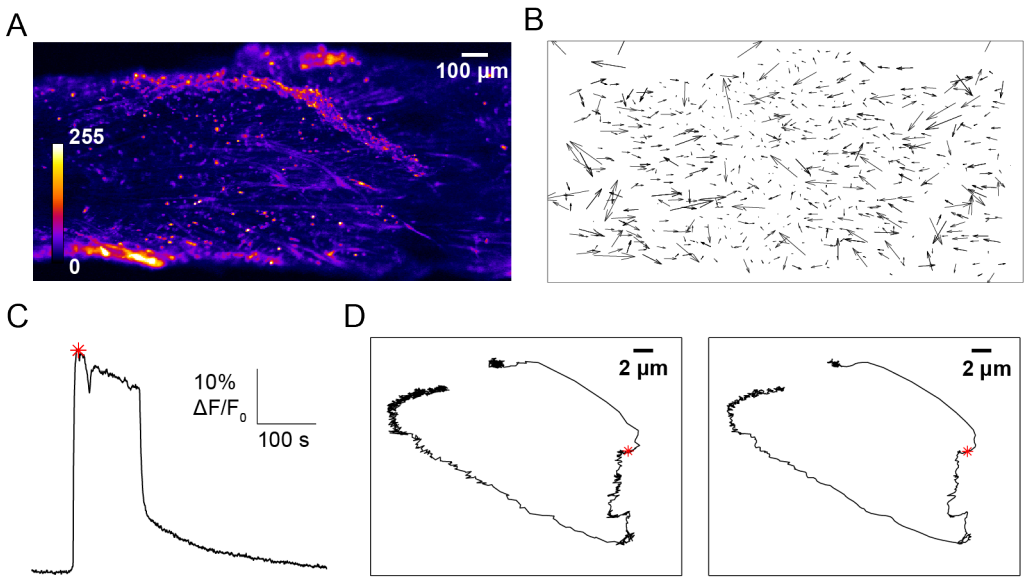

Figure 3.5: **Noise in trajectories prevents use of high temporal resolution outlier detection method** (A) Raw fluorescence image of a Fluo-4 loaded myometrial slice (B) Inter-frame velocity vectors for all tracked landmarks during contractile motion of tissue. Note that for clarity the vectors have been stretched by a factor of 3. (C) The tissue-averaged change in baseline fluorescence (ΔF) for the image sequence. The time at which the velocity vectors in (B) have been taken is indicated (*red* $*$). (D) Raw trajectory (*left panel*) and trajectory after spatial smoothing (*right panel*) of single reliably tracked landmark over contraction-relaxation cycle. Again the time at which the velocity vectors in (B) have been taken is indicated (*red* $*$)

landmarks, where a neighbourhood was defined as a circle centred on the landmark with a radius of $2\lambda_c$. λ_c is the characteristic length scale of the tissue: the length below which tissue deformation during a contraction is local homogeneous (see Section 3.5). This suggests that the trajectories of landmarks within a circle of radius λ_c will be similar and this would therefore be a suitable radius for the local median test. In PIV data, typically the eight neighbouring data points are used in this calculation. We examined the number of neighbours for landmarks contained within circles with a range of radii (Fig. 3.6). For a radius of λ_c the minimum number of neighbours over all landmarks was one; clearly the efficacy of the local median test will be severely comprised with so few neighbours. The minimum number of neighbours over all landmarks was eight when a radius of $2.6\lambda_c$ was used; however this covers an area much larger than the characteristic length scale and is likely to contain heterogeneous displacement vectors. We therefore selected a radius of $2\lambda_c$ to maximise information within the circle while minimising heterogeneity of motion between landmarks.

The scalar residual, r^*, describing the normalised difference between the landmark displacement vector and the median displacement of its neighbouring displacement vectors was computed. The displacement was normalised by the median residual of all neighbouring landmarks. Namely, for a landmark with displacement vector U_0, consider the n displacement vectors of all landmarks within a $2\lambda_c$ neighbourhood of our landmark $\{U_1, U_2, \ldots, U_n\}$. The median displacement vector U_m is calculated using $\{U_1, U_2, \ldots, U_n\}$ and the residual r_i, is calculated for all landmark displacements, excluding our landmark:

$$r_i = |U_i - U_m| \quad \{U_i \mid i = 1, \ldots, n\}. \tag{3.11}$$

The median r_m of $\{r_1, \ldots, r_n\}$ is used to normalise the scalar residual r^* of our landmark:

$$r^* = \frac{|U_0 - U_m|}{r_m}. \tag{3.12}$$

PIV data, for which the local median test is generally successful in identifying outliers, typically comprises high density velocity vectors, with a low proportion of spurious vectors ($\sim$5%, Westerweel, 1994). When the low temporal resolution local median test was applied to our data, it was evident that a far larger proportion than 5% of the trajectories represented unreliable tracks. All tracked landmarks over a contraction-relaxation cycle are shown in Fig. 3.7B (right panel), as are the associated total displacement vectors (left panel). The landmarks with the top 5%

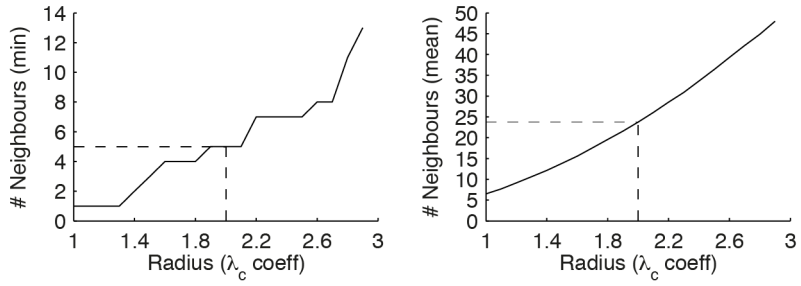

Figure 3.6: **Density of distribution of landmarks** (*Left*) Minimum and (*right*) mean number of landmarks within local neighbourhoods defined by a circle of varying radius. Minimum and mean values are over all landmarks in dataset used in Fig. 3.7

of r^* values are indicated in red. The high number of displacement vectors whose magnitude and direction is inconsistent with the displacement of neighbouring vectors but whose r^* values do not fall within the top 5% illustrates that a significantly higher proportion of the trajectories in this dataset are spurious. This is reinforced by examining the complete trajectories of the landmarks after the the removal of those with the top 5% of r^* values (Fig. 3.7D). Clearly there remains a large number of outlier trajectories which exhibit differences in shape and increased noise compared to neighbouring faithful trajectories. A histogram of the values of r^* for the displacement vectors is shown in Fig. 3.7C, where the top 5% of values are again indicated in red. In their analysis of the local median test applied to PIV data, Westerweel and Scarano (2005) found that a threshold of $r_{th} = 2$ effectively filtered the data for outliers. Whilst we may not need to have such a stringent cut off as this, clearly a significant proportion of the trajectories have a r^* value much larger than 2.

The efficacy of the local median test is severely compromised when a significant proportion of the displacements are unreliable. With this in mind, we implemented a four-stage filtering process, with the low temporal resolution local median test forming the final stage, when the data has been sufficiently filtered such that the proportion of outliers does not compromise its efficacy. The four-stage process is outlined below.

3.4.2 Four-stage outlier detection

Stage one

The first stage identifies landmarks whose trajectories meet during the tracking process and end up at the same location (Fig. 3.10A). In such cases, it is assumed

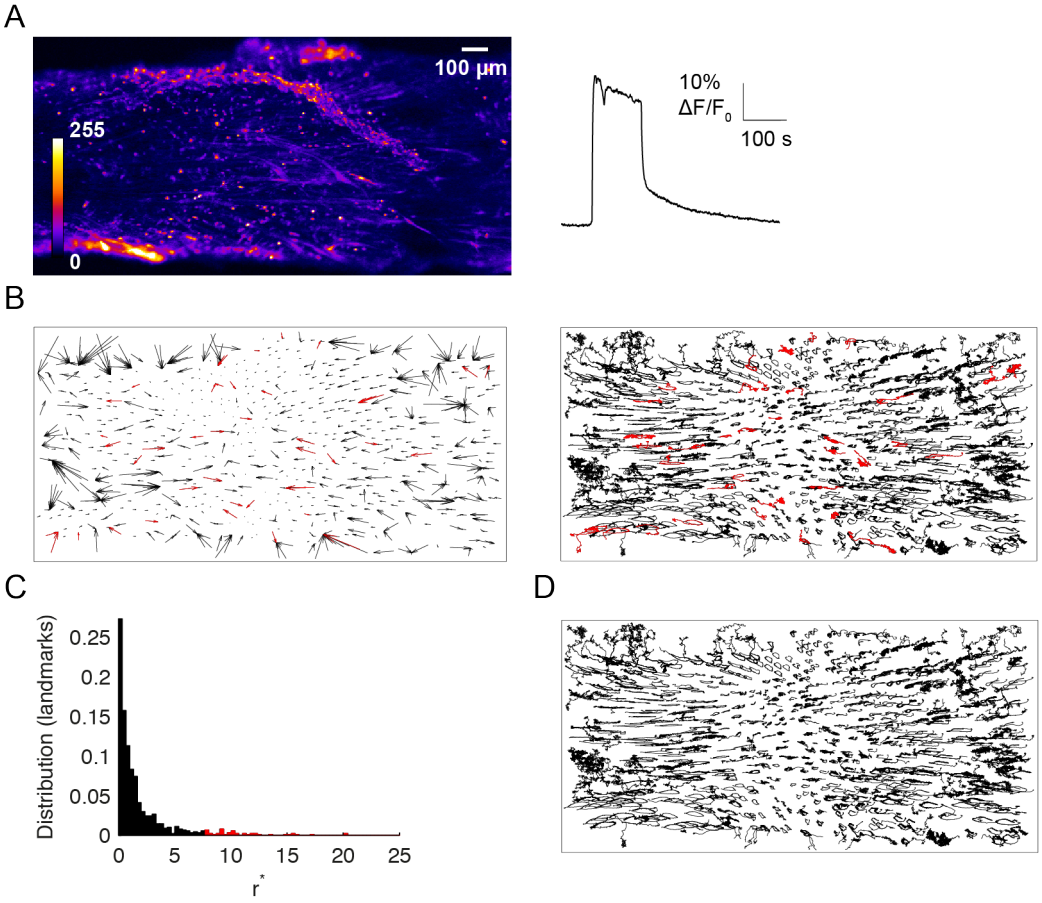

Figure 3.7: **Relatively high proportion of spurious trajectories compromises efficacy of low resolution local median test** (A) Raw fluorescence image of a Fluo-4 loaded myometrial slice (*left panel*) and the tissue-averaged change in baseline fluorescence (ΔF) for the image sequence (*right*). (B) Total displacement vectors for landmarks (*left panel*) and motion trajectories of landmarks (*right panel*) between first and last frames. Landmarks with top 5% of r^* values indicated in red. (C) Histogram of r^* values for landmarks in (B). (D) Remaining trajectories after removal of landmarks with top 5% of r^* values.

that one of the landmarks has been reliably tracked throughout, and the remaining track(s) correspond to landmark(s) that have not been well tracked and therefore 'jump' during the tracking process to follow a more robust trajectory. This jump will be reflected as a change in the velocity in the period before and after the meeting point. The average speed of each of the landmarks whose trajectories intersect is computed separately for the ten frames before and after the meeting point (where the average speed after meeting will be the same for each landmark, as the trajectories are the same). The magnitude of the difference in speed is calculated for each landmark, and the landmark whose average speed changes most is removed. In cases where more than two landmarks meet, this process is repeated for the landmark with the least change in speed at each additional meeting point. In Fig. 3.10A all intersecting trajectories are shown, with the rejected landmark trajectories indicated in magenta.

Stage two

The second stage of filtering identifies landmarks where the average distance travelled between two consecutive frames is greater than the mean plus one standard deviation of the average inter-frame distance for all landmarks. In Fig. 3.8 the distributions of inter-frame distances for landmarks during a quiescent period (left) and a contraction (right) are shown for one dataset. The cut-off of the mean plus one standard deviation was chosen as a stringent threshold, with the recognition that a number of false positive outliers may be discarded at this stage. As indicated above, the motivation behind each of the outlier detection stages was to best approximate the motion of the tissue over the entire image frame, thus improving the spatial resolution of calcium signals that can be extracted. This somewhat crude stage of the process was required to remove trajectories where the landmark being tracked was lost and large jumps occurred. However, we appreciate that deeper analysis of the inter-frame distance distributions and fine tuning of this stage could be incorporated in future work to minimise information loss. In Fig. 3.10B, the landmarks removed based on average inter-frame distance are shown in light blue.

Stage three

In all regions of the tissue, the local velocity should be smooth in space. This means that the configuration of landmarks within a local region relative to each other should not change significantly between the start frame and end frame of a tracking period, whether this period covers a phase of global motion or a quiescent phase (or both).

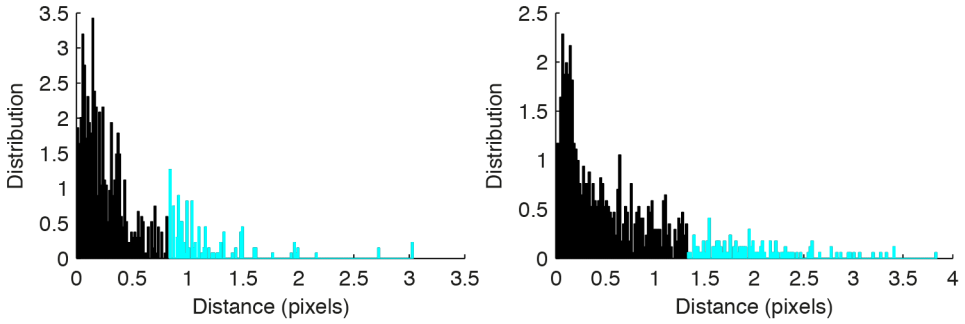

Figure 3.8: **Distributions of inter-frame distances** Distribution of distances travelled by landmarks between two consecutive frames for one dataset during a quiescent period (*left*) and a contraction (*right*). A stringent threshold of the mean plus one standard deviation was chosen to remove outlier trajectories at this stage (*light blue*).

The third stage of filtering removes landmarks whose position changes relative to their neighbours.

For each landmark l, let M be the set of m landmarks (including l) within a $2\lambda_c$ radius of l in the first frame ($l \in M$). Define C_1, an $m \times m$ matrix where each entry $c_1(i,j)$ is the distance between landmarks $i, j \in M$ in the first frame, and similarly, C_F, where each entry $c_F(i,j)$ is the distance between landmarks $i, j \in M$ in the final frame . Define C_{diff}, where each entry $c_{\text{diff}}(i,j) = |c_1(i,j) - c_F(i,j)|$ is the magnitude of the difference in distance between landmarks i, j in the first and last frames. The change in configuration of l relative to its neighbours, δ, is defined as the ratio between the mean magnitude of the difference in distance between our landmark l and all other landmarks and the mean magnitude of the difference between all other landmarks and each other:

$$\delta = \frac{(m-2)^2}{(m-1)} \frac{\sum_i c_{\text{diff}}(l,i)}{\sum_i \sum_{j \neq i} c_{\text{diff}}(i,j)} \tag{3.13}$$

where $i, j \in M$, $i, j \neq l$. Here the pre-factor comes from summing over $(m-1)$ entries in the numerator and over $(m-2)^2$ in the denominator. It is expected that if the motion of l is consistent with its neighbours (and therefore reliably tracked), $\delta \simeq 1$, and for motion inconsistent with neighbours $\delta \gg 1$. For each l we therefore define a configuration change factor ξ which will have a value close to zero for landmarks whose motion is consistent with that of near neighbours:

$$\xi = \frac{m}{L}(\delta - 1). \tag{3.14}$$

Here L is the total number of landmarks. We expect larger values of δ to more

reliably detect outliers where a higher number of neighbouring landmarks have been used and therefore ξ is weighted by the coefficient m/L. This scaling factor also restricts the range of l: $l \in (-1, 1)$. l is removed if ξ exceeds a threshold ξ_{th}. Fig. 3.10C illustrates this stage of filtering. A threshold of $\xi_{th} = 0.05$ was identified by eye to be the optimal value across all datasets tested. Fig. 3.10C (right panel) shows the trajectories of all landmarks following the first stage of filtering, with landmarks for which $\xi > \xi_{th}$ indicated in blue. A histogram of the values of ξ for all landmarks is given in Fig. 3.10C (left), where landmarks with values of $\xi > \xi_{th}$ are again shown in blue.

As previously discussed, we chose the radius of our circle enclosing neighbours used in this outlier detection step and the local median test step (to follow) as a compromise between maximising the amount of local information contained within the circle and minimising the expected heterogeneity of motion within the circle. This compromise meant that although the density of landmarks within our neighbourhood was generally in line with typical PIV data for which the local median test was designed (≥ 8 landmarks), some landmarks were more isolated and outliers amongst these landmarks may be missed by these two detection methods. Fig. 3.9 shows the number of neighbours for landmarks contained within circles with a range of radii following the first two outlier detection stages. For the radius chosen ($2\lambda_c$) the minimum number of landmarks within a neighbourhood was two (Fig. 3.9; left panel). At this stage we also removed landmarks where it was felt that there was insufficient local information for the two local outlier detection steps to reliably perform; i.e., landmarks with less than three neighbours (Fig. 3.10C (left panel, green)). It is recognised that in removing these landmarks we are potentially discarding valuable information; however, as previously discussed, we found that a bias towards removing false positive outliers was preferable over keeping false negatives. An extension to this work could see the further development of this multistage outlier detection process to minimise information loss.

Stage four

Finally, the low temporal resolution adaptation of the local median test is applied to the remaining landmarks (Fig. 3.10D), as previously described. The total displacement vectors (top left panel) and the complete trajectories (bottom left panel) between the first and last frames for landmarks following the first three stages filtering are shown, with landmarks with top 5% of r^* values indicated in red. This time the proportion of landmarks for which the trajectories are spurious is much closer to 5%, and the maximum r^* value for the remaining landmark trajectories is much

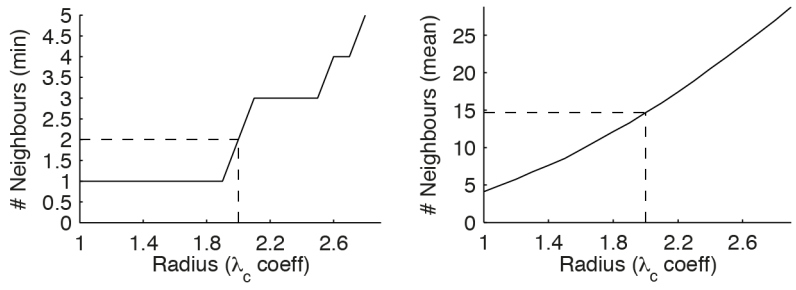

Figure 3.9: **Density of distribution of landmarks following first two outlier detection stages** (*Left*) Minimum and (*right*) mean number of landmarks within local neighbourhoods defined by a circle of varying radius. Minimum and mean values are over all landmarks following first two stages of outlier detection in dataset used in Fig. 3.7

closer to 2 (Fig. 3.10D, top left graph). In practice in our datasets, we found using a threshold of $r_{th} = 3$ to be a sufficiently stringent choice; lower values were found to filter reliable trajectories and reduce the data from which to extrapolate tissue-wide motion. Fig. 3.10D (bottom left panel shows the trajectories remaining after the four stages of filtering for outlier removal.

3.5 Characteristic length scale and motion corrected images

Having obtained the trajectories of each landmark and filtered for outliers it remains to estimate the movement of the tissue between landmarks; this is the final step of the motion-correction algorithm leading to the data presented in Fig. 3.1D. This extrapolation is achieved through an optimal distance-weighted average of nearby landmark trajectories. Consider the displacement from the initial position in the first frame of a particular landmark, which we will label l

$$D_l = (d_x, d_y), \tag{3.15}$$

where

$$d_x = (0, x_2 - x_1, x_3 - x_1, \ldots, x_N - x_1)^T \tag{3.16}$$

$$d_y = (0, y_2 - y_1, y_3 - y_1, \ldots, y_N - y_1)^T, \tag{3.17}$$

and N is the total number of frames over which the landmark has been tracked. The displacement D_p of the tissue under one of the pixels in the first image will be similar to that of nearby landmarks. If the displacement of only the nearest landmark

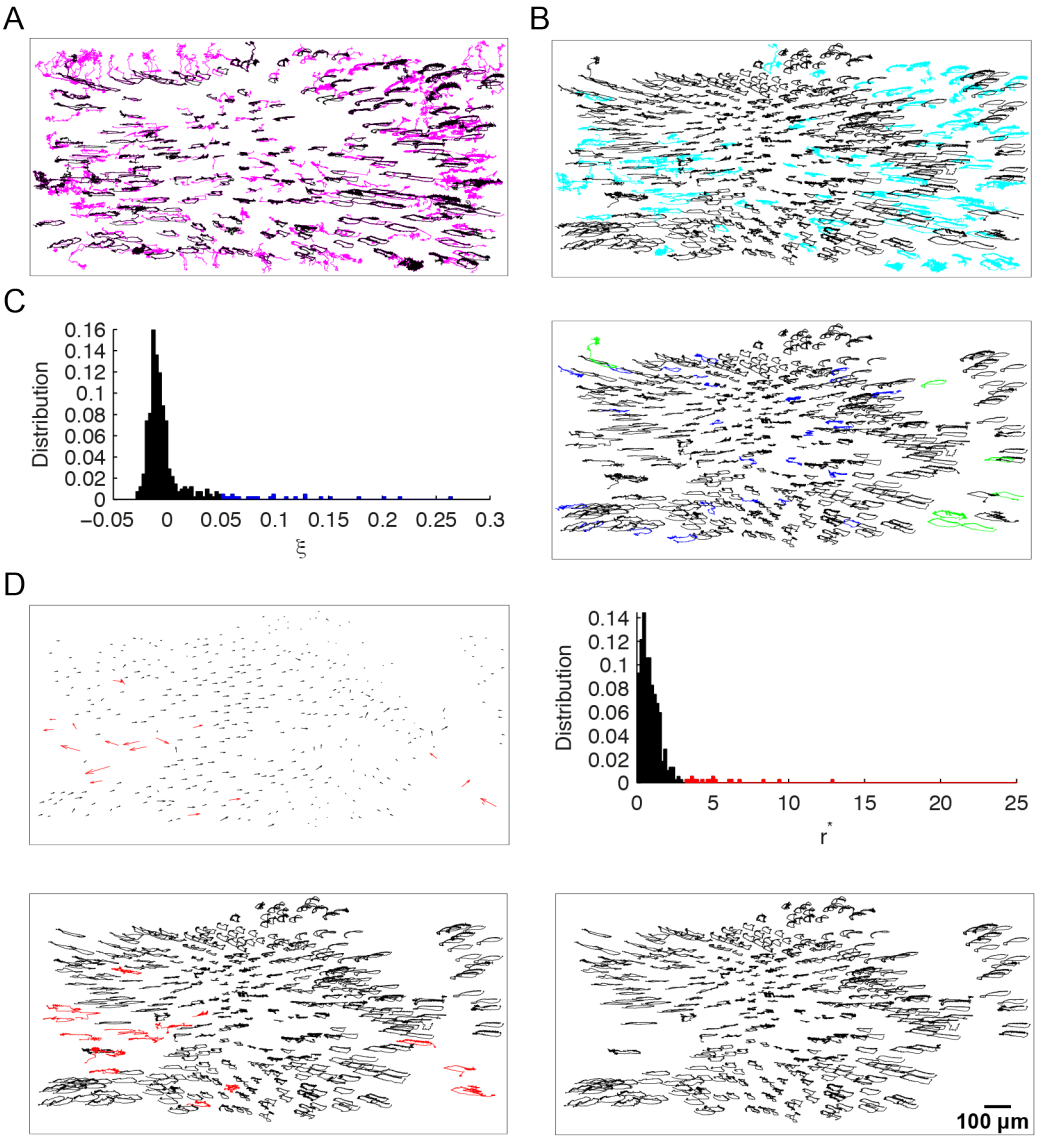

Figure 3.10: **Outlier trajectories are removed using a four-stage filtering process** (A) First stage of filtering. Intersecting trajectories filtered based on speed before and after time of convergence. Only intersecting trajectories are shown; trajectories to be removed indicated (*magenta*). (B) Second stage of filtering. Trajectories following first stage of filtering are shown; trajectories with high average inter-frame distance to be removed (*light blue*). (C) Third stage of filtering. *Left:* Histogram of ξ values, where landmarks with $\xi > \xi_{th}$ indicated (*blue*, $\xi_{th} = 0.05$). *Right:* Trajectories of landmarks following first 2 stages of filtering. Landmarks with $\xi > \xi_{th}$ removed (*blue*), where ξ represents relative change in configuration of each landmark between first and last frame. Isolated landmarks with less than 3 local neighbours also removed (*green*). (D) Fourth stage of filtering. *Top left:* Total displacement vectors for landmarks between first and last frame following first 3 stages of filtering. *Top right:* Histogram of r^* values for landmarks. *Bottom right:* Complete trajectories of landmarks. Landmarks with top 5% of r^* values indicated (*red*). *Bottom left:* Trajectories of remaining landmarks following four stages of filtering for outliers.

is used to estimate D_p there will be a discontinuity between displacements of adjacent pixels with different nearest landmarks. At the other extreme, if an unweighted average over all landmarks were used regardless of distance then all pixel displacements would be identical. There must therefore exist an optimal length scale, within which contracting tissue motion is locally homogeneous, for the estimation of D_p from nearby landmark displacements. We will call this the *characteristic length scale* for myometrium: though it is required for the motion correction, it is a key biophysical characteristic of the tissue structure because it gives the scale below which the tissue remains homogeneous under contraction. If we call ϕ_{pl} the distance between the tissue under a pixel p and a landmark l in the first image frame, then the weighting function $W_{pl}(\lambda) = \exp(-\phi_{pl}/\lambda)$ can be introduced where λ is the length scale that must be optimised. We can write the distance-weighted estimate for the displacement $D_p(\lambda)$, for a particular guess of the scale λ, as

$$D_p(\lambda) = \frac{\sum W_{pl}(\lambda) D_l}{\sum W_{pl}(\lambda)}, \tag{3.18}$$

where the sums are over all tracked landmarks. It now remains to find the optimal value of λ. This is straightforwardly achieved by comparing the prediction of equation (3.18) when the pixel p is a landmark itself (for which the displacement is known) for a range of different λ. The value which gives the best prediction of the known landmark displacements, using a weighted average of the other landmarks, we call the characteristic length (λ_c) of myometrial tissue.

In this work we chose λ to be isotropic. This choice of λ reflects the primary motivation behind the motion-correction algorithm in this thesis: i.e., to best approximate the motion of the tissue over the entire image frame and therefore stabilise the images. The image sequences we processed in this thesis often comprised multiple myocyte bundles of varying alignment contracting simultaneously and producing spatially heterogeneous movements within the field of view. The contractile and mechanical properties of the tissue will vary significantly between highly contractile myocyte bundles and passive connective tissue. An isotropic λ was chosen to best capture the average characteristic length scale of this highly heterogenous tissue.

An interesting direction for further work would be to examine whether other, non-isotropic values of λ can be found to characterise more localised regions of tissue. For example, given the spindle-shaped structure of myocytes and their parallel alignment within bundles, it seems likely that the contractile properties within bundles may be governed by two perpendicularly aligned values of λ. It would be

interesting to examine whether the contractile properties of myocyte bundles can be well captured by two perpendicularly aligned characteristic length scales. The deformation of the connective tissue in between myocyte bundles is dependent on the alignment and proximity of neighbouring myocyte bundles. As the connective tissue is not active in the tissue contraction, we would expect the motion in these regions to be best described by isotropic value of λ, such as implemented in this work.

Once found the displacements given in equation (3.18) are computed using the optimal λ_c. To find the position in a subsequent frame of the tissue which was under a particular pixel in the first frame, all that is required is to add its initial co-ordinates in the first frame to the displacements D_p. Finally, the motion-corrected image sequence can now be constructed by mapping the intensity value found at a position in any later frame back to its point of origin in the first frame. As tissue positions are at subpixel resolution bilinear interpolation is used to assign intensity value.

3.6 Significant reduction of motion artifacts

Our algorithm processes calcium-image sequences of contracting myometrium for removal of motion artifacts by tracking the movement of identifiable landmarks and extrapolating to obtain a complete description of the tissue-wide motion. This description is then used to produce a new 'static' image sequence in which the contractile motion has been removed. The algorithm was tested on over twenty datasets of imaged myometrium. In all of the datasets tested processing the images resulted in a significant, if not complete, reduction of the motion artifacts over multiple contraction-relaxation cycles and across the entire imaged slice. Fig. 3.11 illustrates the reduction of motion in one spontaneously contracting imaged myometrial slice. In Fig. 3.11A the maximum intensity projections (each pixel takes its maximum value over the entire image sequence) for a single contraction-relaxation cycle are presented for the raw and processed data. In the raw dataset the trajectories of high $[Ca^{2+}]_i$ intensity regions are clearly evident as they move into areas previously occupied by the lower intensity intercellular matrix (Fig. 3.11A, left panel). After processing, the effects of motion are significantly reduced across all areas of the image (Fig. 3.11A, right panel). The tissue-averaged change in baseline fluorescence (ΔF) is shown to the right of the top two panels, indicating the time frame over which the maximum intensity projection was calculated (one contraction-relaxation cycle). In Fig. 3.11B a single frame of the imaged tissue in a contracted state (green)

is superimposed upon a single frame of the tissue in a relaxed state (red) for both the raw (left panel) and processed (right panel) datasets. The positions of the two frames in the contraction-relaxation cycle are indicated in the tissue-averaged $\triangle$F signal (right, red and green $*$). A significant improvement in the alignment of the two frames of imaged tissue can be seen in the processed data compared to the raw data. Consistent throughout all datasets was the ability of the algorithm to reliably reduce motion artifacts in all regions of the image where the tissue was intact and in focus. Lower quality of correction can be seen towards the bottom of the processed superimposed images in Fig. 3.11B where the edge of the imaged tissue has curled over and so was out of focus.

3.7 Comparison with Horn-Schunck method

We compared our method of motion-correction with the Horn-Schunck optical flow method (Fig. 3.12). We found that both methods were effective at reducing motion artifacts, evidenced by the alignment between frames taken immediately before and after the $[Ca^{2+}]_i$-mediated action potential (Fig. 3.12A, B, top left panel). However, we found that images processed using the Horn-Schunck method suffered a loss of fine resolution detail; the architecture of the tissue slices becomes warped (Fig. 3.12B). This is particularly evident in the two magnified panels. The myocyte bundle in the upper left corner of the panels loses its form in the images processed using the Horn-Schunck method; the individual myocytes and myocyte bundles remains intact after processing using our method (Fig. 3.12A).

3.8 Comparison of tracking methods

We compared the simple and extended Lucas-Kanade registration algorithms and the Gaussian-fitting method for tracking identified landmarks (Figs. 3.13 and 3.14). We used each method to track the landmarks in a single dataset and used our algorithm detailed above to remove outliers, extrapolate the trajectories and process the images for motion correction. We found that the simple Lucas-Kanade method was better suited to our data than the extended version, with a slight improvement in outcome and a significant improvement in speed of performance (Fig. 3.13). We found little difference between the simple Lucas-Kanade registration algorithm and the Gaussian-fitting method for landmark tracking performance, as illustrated in Fig. 3.14. The maximum intensity projections show no evidence of motion artifacts

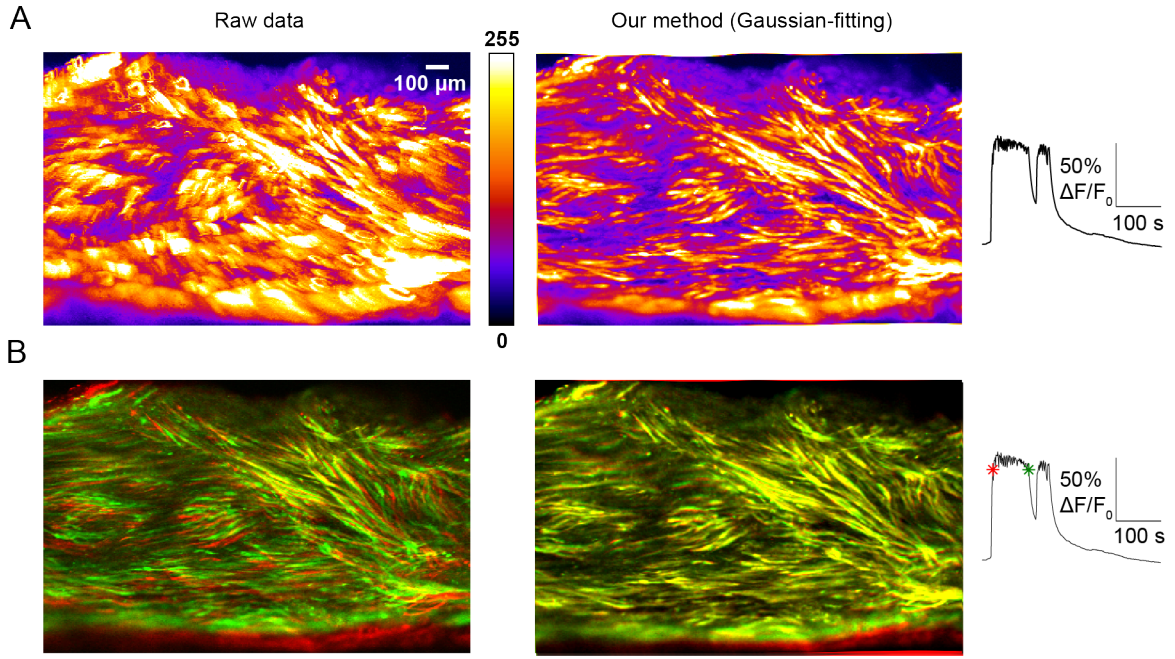

Figure 3.11: **Elimination of motion artifacts in images of contracting myometrium** (A) Maximum intensity projection of the image sequence over a contraction-relaxation cycle was calculated for the raw (*left panel*) and processed (*right panel*) data. As can be seen, the trajectories of high intensity regions in the raw images are significantly reduced in the processed images. The tissue-averaged change in baseline fluorescence (ΔF) over the contraction-relaxation cycle used in the maximum intensity projection calculation is shown to the right of the two panels. (B) Raw fluorescence images (*left panel*) and images processed for movement reduction (*right panel*) showing the Fluo-4 loaded tissue slice in a contracted state (*green*) superimposed upon the imaged slice in a relaxed state (*red*). Improved alignment between the two frames can be seen in the processed images compared to the raw images. The positions of the two frames in the contraction-relaxation cycle are indicated in the tissue-averaged ΔF timecourse (*far right, red and green* $*$*).*

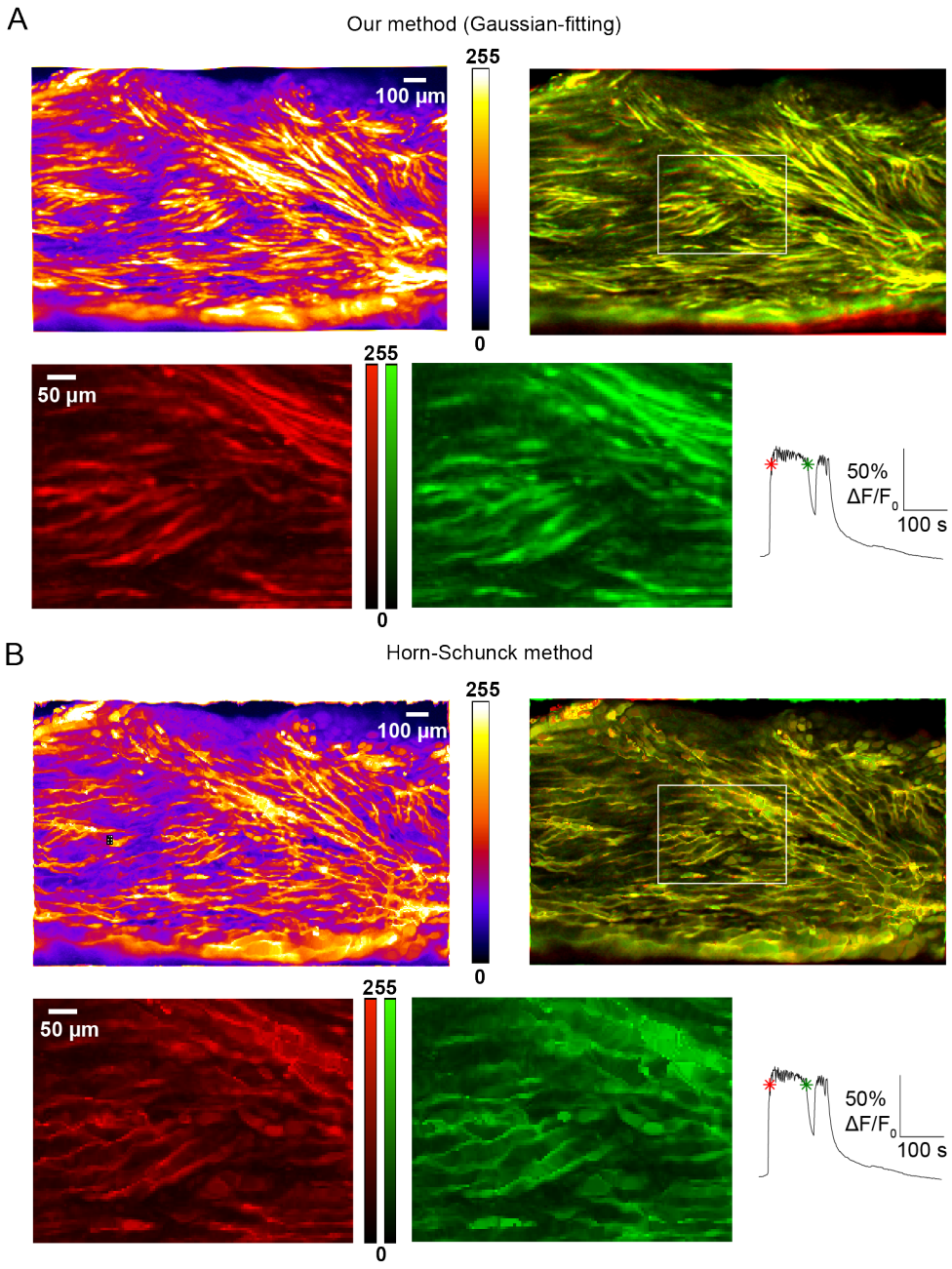

Figure 3.12: **Our method of motion-correction outperforms Horn-Schunck method** (A) Our method. (B) Horn-Schunck method. (A, B) *Top left:* Maximum intensity projection of the image sequence over a single contraction-relaxation cycle. *Top right:* Images processed for motion-correction showing the Fluo-4 loaded tissue slice in a contracted state (*green*) superimposed upon the imaged slice in a relaxed state (*red*). Good alignment can be seen between the two images processed using both methods. *Bottom:* Magnified subsection of two frames used in superimposition. Images processed using the Horn-Schunck method suffer a loss of fine resolution detail (see particularly the myocyte bundle in the top left of the magnified frames). The tissue-averaged change in baseline fluorescence (ΔF) is shown to the right of the panels. The frames used in the superimposition are indicated (*red and green* $*$).

(Fig. 3.14A) and there is good alignment between the two frames taken immediately before and after the $[Ca^{2+}]_i$-mediated action potential (Fig. 3.14B). However, we found that the Lucas-Kanade registration algorithm was over four times slower than the Gaussian-fitting algorithm for identifying landmarks and slightly slower for landmark tracking (Fig. 3.14D). There is an additional advantage of using the Gaussian-fitting method of landmark tracking: the tracked landmarks are biologically identifiable: they represent small cell bodies - most likely invading leukocytes and myocytes damaged by the slice-cutting procedure.

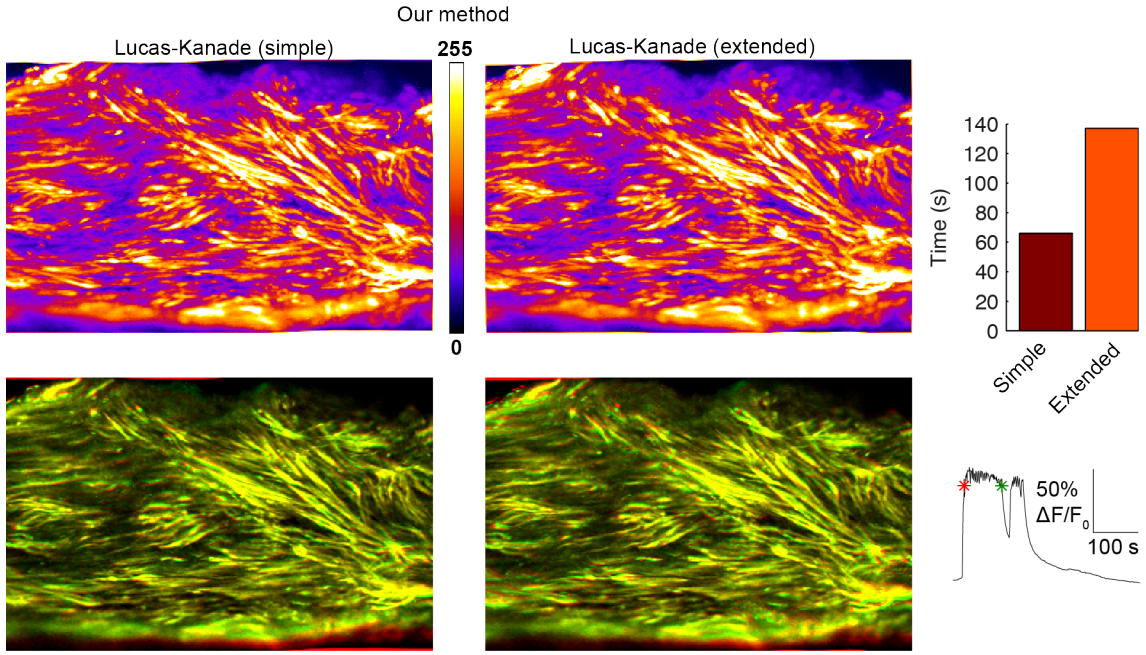

Figure 3.13: **Simple Lucas-Kanade method is better suited to our data than the extended version** *Top panels:* Maximum intensity projection of the image sequence over contraction-relaxation cycle was calculated for the images processed using our method with simple (*left panel*) and extended (*right panel*) Lucas-Kanade landmark tracking. *Top right:* Simple Lucas-Kanade method is significantly faster than extended version. Plot shows typical processing speed for tracking motion of landmarks between two frames. *Bottom panels:* Images processed using simple (*left panel*) and extended (*right panel*) Lucas-Kanade landmark tracking showing the Fluo-4 loaded tissue slice in a contracted state (*green*) superimposed upon the imaged slice in a relaxed state (*red*). Slight increased alignment can be seen between the two frames in the simple Lucas-Kanade (see particularly top left and bottom right corners of images).

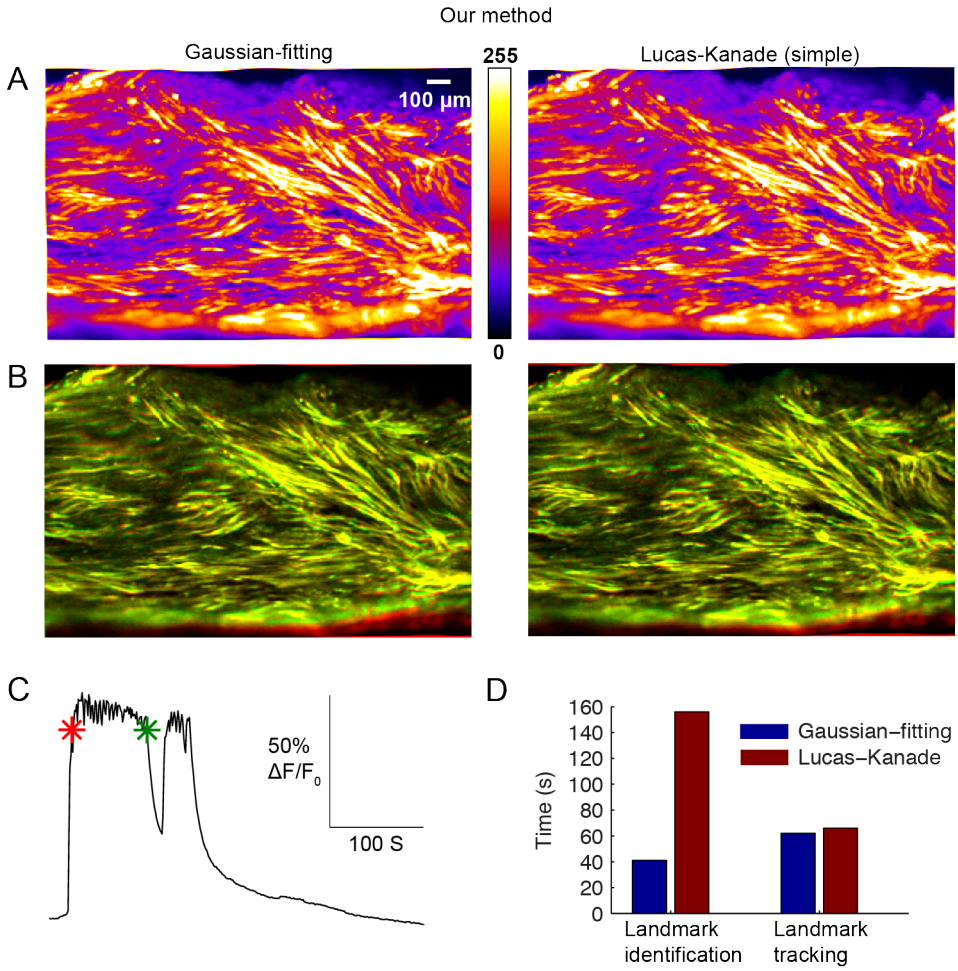

Figure 3.14: **Gaussian-fitting method is optimal for tracking landmarks in our data** (A) Maximum intensity projection of the image sequence over contraction-relaxation cycle was calculated for the images processed using our method with Gaussian-fitting (*left panel*) and simple Lucas-Kanade (*right panel*) landmark tracking. (B) Images processed using Gaussian-fitting (*left panel*) and simple Lucas-Kanade (*right panel*) landmark tracking showing the Fluo-4 loaded tissue slice in a contracted state (*green*) superimposed upon the imaged slice in a relaxed state (*red*). There is good alignment between the two frames in both cases. (C) The positions of the two frames in the contraction-relaxation cycle are indicated in the tissue-averaged ΔF timecourse (*red and green* $*$). (D) Gaussian-fitting is faster than simple Lucas-Kanade method for landmark identification and tracking. Plots show typical processing speed for landmark identification and time taken to track motion of landmarks between two frames.

Chapter 4

Analysis of calcium signals

Calcium indicator fluorescence imaging of intact human and rat myometrium is a favoured method for investigating the processes underlying excitation-contraction coupling. The intracellular contractile machinery is activated by a Ca^{2+} -mediated action potential, meaning that $[Ca^{2+}]_i$ measurements can be used as a proxy for electrical activity (Taggart et al., 1996; Noble and Wray, 2002; Jones et al., 2004; Nobel et al., 2014). While $[Ca^{2+}]_i$ entry via voltage-gated L-type channels is well established as the primary source of $[Ca^{2+}]_i$ required for calmodulin-mediated activation of crossbridge cycling and cell contraction, elucidation of other pathways involved in the process remain incomplete. For example, evidence for the mechanism governing the initial depolarisation of cells such that the L-type channels are activated - pacemaker activity - is currently lacking.

Ion channels provide a potential mechanism by which cells may depolarise prior to action potential-driven contractions; it has been suggested that voltage-activated T-type calcium channels (Blanks et al., 2007) and calcium-activated chloride channels (Jones et al., 2004) may contribute to pacemaker depolarisation. There is significant variability in expression of these channels between individual myocytes; T-type calcium and calcium-activated chloride currents were found in 55% and 30% of pregnant human and rat myometrium respectively. Such heterogeneity between individual cells highlights the importance of multiple single-cell measurements taken from relatively large tissue samples.

The complexity of the structure of the myometrium means that there is variation in the propagation as well as in the initiation of action potential spikes. Electromyogram recordings (Lammers et al., 2008) and calcium indicator fluorescence recordings (Burdyga et al., 2009; Bru-Mercier et al., 2012) of intact myometrium as well as mathematical models (Young and Barendse, 2014) have found variable ini-

tiation sites and direction of propagation of electrical activity during myometrial contractions. The motion artifacts in contracting tissue have previously set spatiotemporal limitations on $[Ca^{2+}]_i$ recordings: single-cell $[Ca^{2+}]_i$ measurements could only be taken during quiescent phases; during contraction-relaxation cycles spatial averages had to be used.

In this chapter, using motion-corrected images we show for the first time that unrestricted single-cell $[Ca^{2+}]_i$ measurements can be taken from myometrial tissue slices over multiple contraction-relaxation cycles. We see spatial heterogeneity in $[Ca^{2+}]_i$ signals which support there being variable initiation sites for action potential propagation. We examine $[Ca^{2+}]_i$ signals between contractions to see if pacemaker activity can be identified through increases in single-cell $[Ca^{2+}]_i$ signals. Finally we compare single-cell $[Ca^{2+}]_i$ dynamics in control and oxytocin-treated myometrium. We begin by illustrating the improvement in spatial resolution in images of contracting myometrium processed using our motion-correction algorithm.

4.1 Improvement in spatial resolution

To quantify the improvement in spatial resolution that our algorithm affords, we tracked the centre of a high fluorescence feature over a contraction-relaxation cycle in both raw and processed images (Fig. 4.1). The identified feature (Fig. 4.1A, arrow) of diameter $\sim$20μm maintained a stable fluorescence level throughout the contraction-relaxation cycle. In Fig. 4.1B, the tracked centre of the feature is shown (black line) on a maximum intensity projection of the raw (top panel) and processed (bottom panel) images. The horizontal and vertical displacements of the centre of the feature were reduced from 71 pixels to 1 pixel and 24 pixels to 1 pixel, respectively following processing for motion reduction (Fig. 4.1C). In all datasets tested, processing the images for motion reduction resulted in an improvement in the spatial resolution down to pixel level (1-4.5μm in our image sets).

4.2 Increased spatiotemporal information

The $\sim$50-fold improvement in spatial resolution allows for the detection and measurement of fine detail in local $[Ca^{2+}]_i$ signals that would otherwise be missed or corrupted by neighbouring signals. In Fig. 4.2 a magnified subsection of images of oxytocin-induced contracting tissue taken at four different time points over a single contraction-relaxation cycle is shown for both the raw (Fig. 4.2A) and processed (Fig. 4.2B) data. Four regions of interest (ROIs) have been highlighted, and the

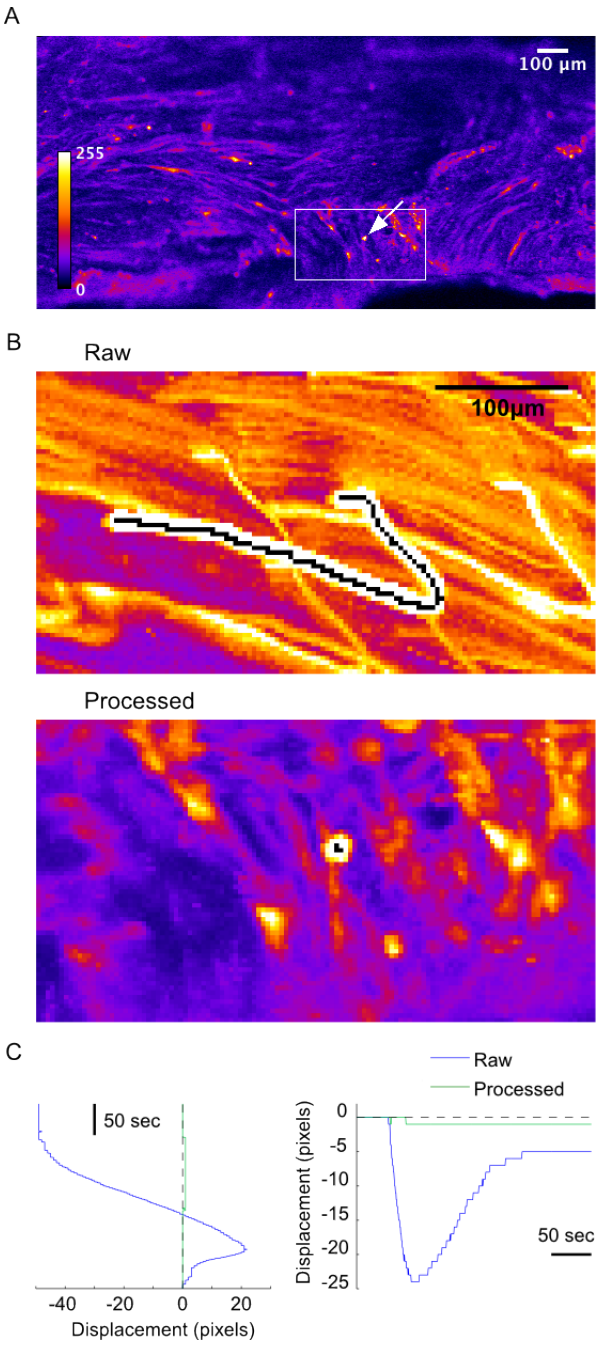

Figure 4.1: **Improvement in spatial resolution down to pixel scale** (A) A feature of high intensity is identified (*arrow*) in the raw fluorescence image of a Fluo-4 loaded myometrial slice. (B) The centre of the feature in (A) was tracked over a contraction-relaxation cycle in both the raw (*top panel*) and processed (*bottom panel*) images. Tracks are shown (*black lines*) on the maximum intensity projections of each image stack over contraction-relaxation cycle. (C) Horizontal (*left*) and vertical (*right*) displacements of the feature centre for raw and processed data. Total displacement is reduced to a single pixel in both horizontal and vertical directions in the processed images.

ΔF time course from within these ROIs is plotted in Fig.4.2C. The improved spatial resolution permits measurement of fine temporal detail, as is particularly evident in the ΔF signal for ROI3, where the region encompasses a micro vessel with high frequency fluctuations of $[Ca^{2+}]_i$. Micro vessels look like elongated conglomerates of small(ish) cells (vascular smooth muscle cells plus vascular endothelial cells) that move together as one structure when the slice contracts but may exhibit $[Ca^{2+}]_i$ oscillations that are smaller in amplitude and are not synchronized between individual members of that conglomerate. When an ROI is positioned above this conglomerate, the global high-amplitude $[Ca^{2+}]_i$ transients may appear to be superimposed on the smallish asynchronous oscillations due to the light leaking from neighboring uterine myocytes.

4.3 Spatial heterogeneity of calcium signals

In spontaneously contracting myometrium, cells in which $[Ca^{2+}]_i$ levels fluctuate between contractions have been identified in rat and human tissue (Burdyga et al., 2009; Bru-Mercier et al., 2012). Previously, it has not been possible to directly compare the calcium transients of cells exhibiting fluctuating behaviour within a contracting tissue slice due to the associated motion. Using our algorithm, we compared the transients of all subregions of tissue visually identified as exhibiting $[Ca^{2+}]_i$ fluctuations between contractions in a dataset in which the tissue was spontaneously contracting.

Fig. 4.3 shows the signals extracted from ROIs encompassing subregions that are quiet between contractions (ROIs 1-3) or show fluctuating $[Ca^{2+}]_i$ levels (ROIs 4-12; see also Fig. 4.4). The ΔF signals reveal significant spatial heterogeneity of $[Ca^{2+}]_i$ activity between and during contractions. There are clear correlations between the activity of some subregions that are not just limited to the peaks associated with global contractions, for example the similarity in the patterns of activity between ROI 11 and ROI 12 indicates a strong electrical connection between these two transversely neighbouring cells. The high spatiotemporal detail revealed in the motion-corrected data allows detection of local contractions occurring between global contractions: two such local contractions have been highlighted in Fig. 4.3 for ROIs 7 and 8. Local activity is frequently seen to precede a global contraction (e.g. in ROIs 9-11) suggesting the identified regions might act as pacemakers, recruiting the remaining tissue during each contraction. The variability in the timing and location of this activity supports the view that there is no fixed anatomical site for pacemaker activity in the myometrium. A noteworthy waveform is that of ROI 6,

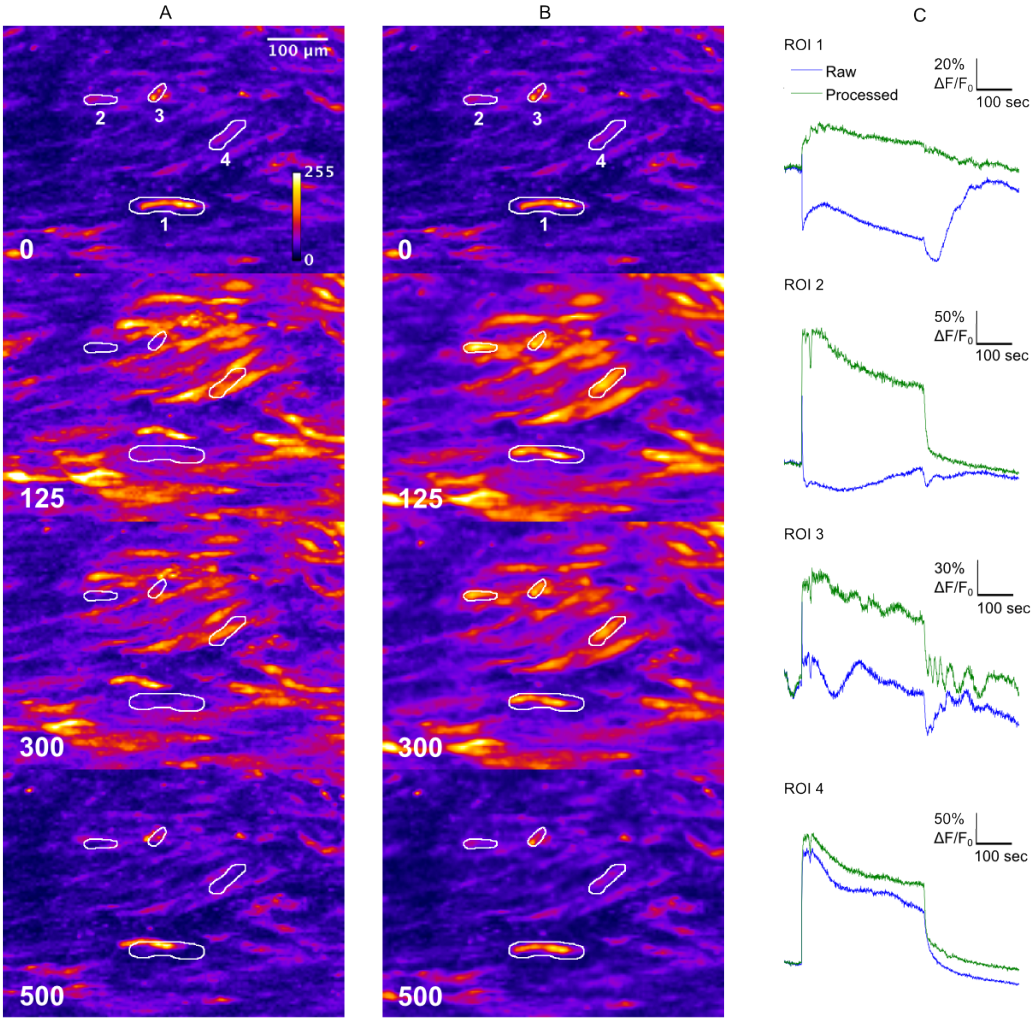

Figure 4.2: **Fine spatiotemporal detail of $[Ca^{2+}]_i$ signals revealed by motion correction** (A,B) Magnified subsection of imaged tissue taken at times indicated (sec) showing raw (A) and corrected (B) images over a contraction-relaxation cycle. Four regions of interest (ROIs) have been highlighted to illustrate the motion correction. (C) Time course of change in baseline fluorescence (ΔF) for the four ROIs for the raw and corrected images over contraction-relaxation cycle.

which exhibits high frequency oscillations throughout the image sequence. These appear to be independent of the activity in other regions and may be indicative of the physiological behaviour of a myocyte in the cell cycle or a damaged cell.

The $[Ca^{2+}]_i$ activity between contractions in Fig. 4.3 is suppressed by application of 1μM nifedipine, an L-type calcium channel blocker, providing evidence that L-type Ca^{2+} currents are one mechanism underlying the $[Ca^{2+}]_i$ fluctuations. However, in agreement with Bru-Mercier et al. (2012) many of the $[Ca^{2+}]_i$ fluctuations in Fig. 4.4 are insensitive to nifedipine, suggesting that at least two different mechanisms contribute to single-cell fluctuations in $[Ca^{2+}]_i$ between contractions. The sarcoplasmic reticulum (SR) provides a source of internal Ca^{2+} and it is also possible that Ca^{2+} unloaded from the SR by passive leak could contribute to fluctuations in $[Ca^{2+}]_i$. If the Ca^{2+} concentration in the SR is greater than that of the $[Ca^{2+}]_i$ then a slow passive Ca^{2+} leak retains the steady state Ca^{2+} level within the lumen of the SR (Camello et al., 2002). Further research is required to examine the role of Ca^{2+} leak in regulating SR-mediated $[Ca^{2+}]_i$ activity in myometrial cells and whether this could produce local fluctuations in $[Ca^{2+}]_i$ (Shmygol and Wray, 2004).

It is likely that the asynchronous $[Ca^{2+}]_i$ activity we see in ROI4-8 in Fig. 4.4 are recordings from vascular smooth muscle cells rather than myometrial cells. Vascular smooth muscle cells are not electrically coupled to myometrial myocytes; however light leaking from neighbouring myocytes may contribute to the peaks in $[Ca^{2+}]_i$ associated with global myometrial contractions in the recordings in Fig. 4.4.

4.4 Calcium activity prior to contractions

Pacemaker locations were recently identified in a study analysing the contractile and electrical spontaneous activity in the isolated uteri of pregnant rat and guinea pig at term (Lammers et al., 2015). This study revealed that in both rat and guinea pig uteri there is no specific pacemaker site, and that electrical activity may arise from any site. However, the mechanisms underlying pacemaker activity in the myometrium remain unclear. It has been suggested that T-type Ca^{2+} channels, which were found in $\sim$50% of isolated human myometrial cells, may contribute to the slow depolarisation of a subset of cells that then trigger action potentials (Blanks et al., 2007; Bru-Mercier et al., 2012).

We examined the $[Ca^{2+}]_i$ activity of a large number of myocytes prior to a contraction. Fig. 4.5 illustrates this for the same dataset as shown in Fig. 4.3, in which the tissue undergoes four spontaneous contractions. The average intensity signals for the cells identified in the image in the eight seconds prior to each contrac-

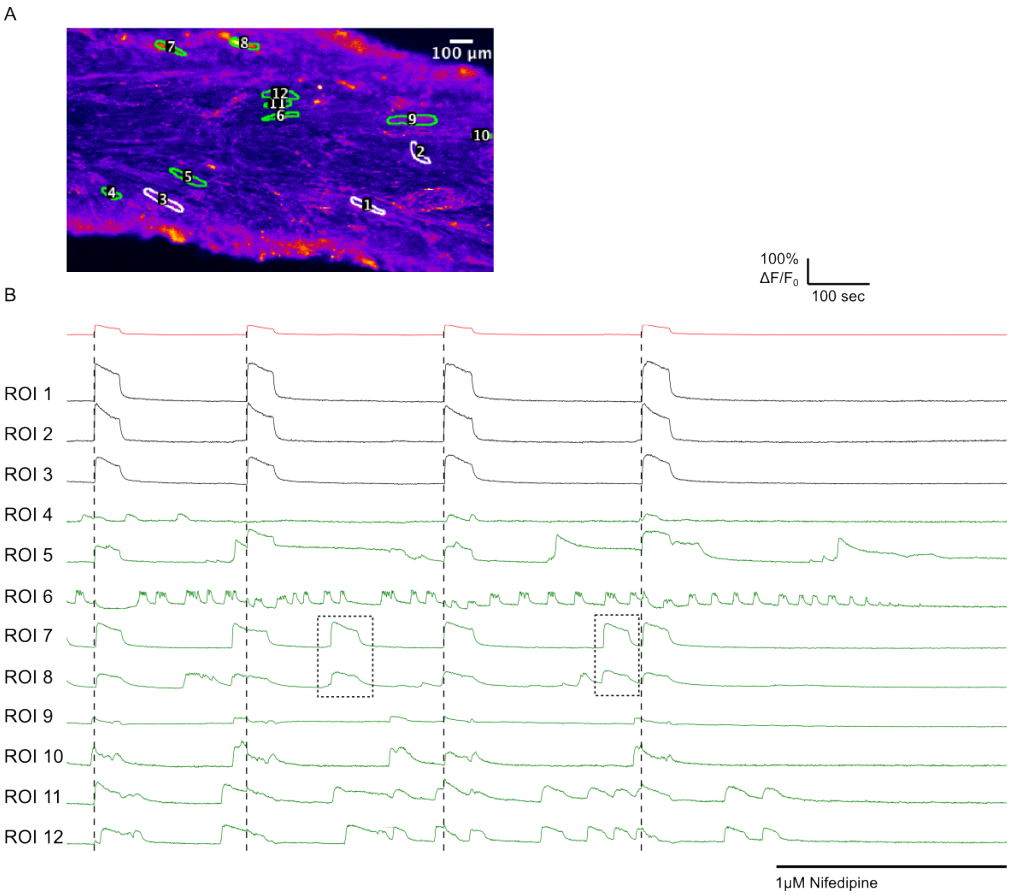

Figure 4.3: **Spatial heterogeneity of $[Ca^{2+}]_i$ activity in contracting myometrium** (A) ROIs encompassing subregions of tissue that exhibit periods between global contractions with either non-fluctuating (*white*) or fluctuating (*green*) $[Ca^{2+}]_i$ levels. (B) Change in baseline fluorescence (ΔF) over multiple contraction-relaxation cycles: averaged over entire tissue (*red*) and for the ROIs in (A) (non-fluctuating ROIs 1-3 *black*, and fluctuating ROIs 4-12 *green*). The onsets of global contractions are marked (*vertical dashed lines*). Note that the full contractile waveforms can be seen at intermediate times in a subset of the ROIs (7 and 8, *dotted rectangles*) and also that a subset of ROIs (e.g. 9, 10, 11) frequently show activity that proceeds a global contraction. Application of nifedipine resulted in the eventual cessation of global contractions and all heterogeneous activity.

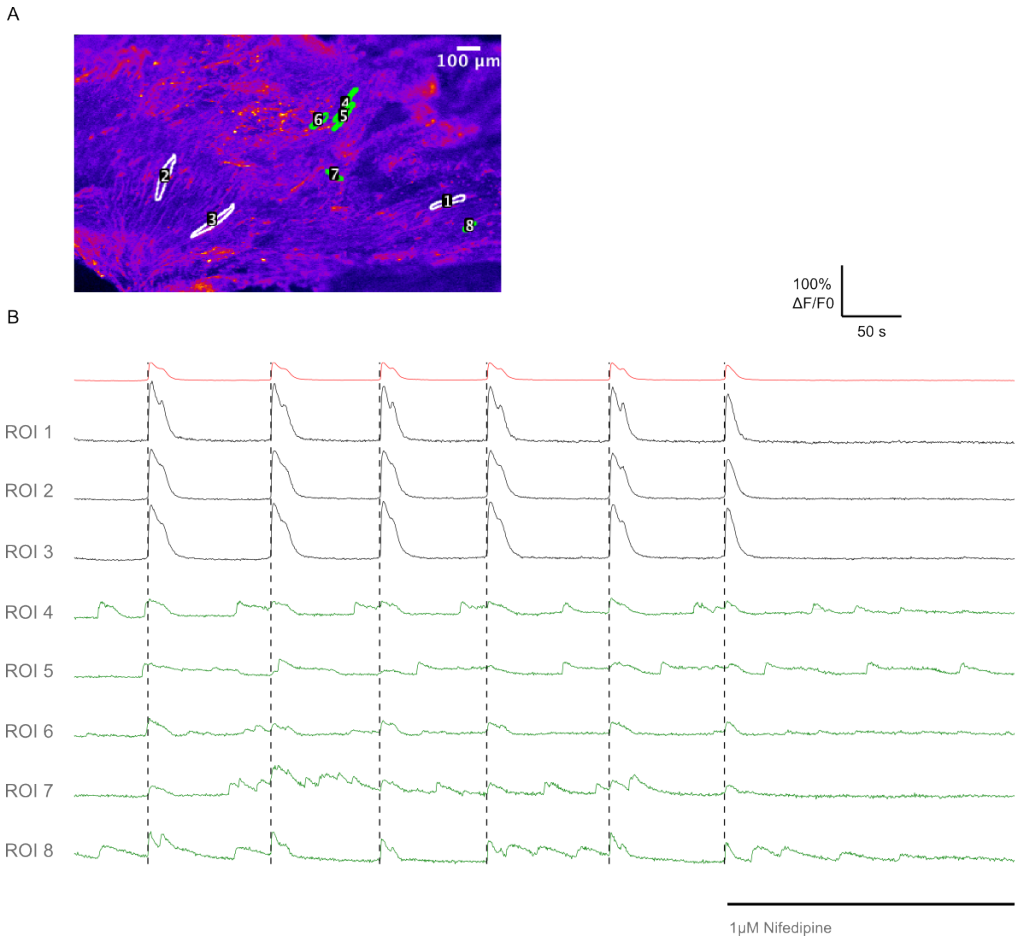

Figure 4.4: **Local $[Ca^{2+}]_i$ activity in spontaneously contracting myometrium** (A) ROIs encompassing cells exhibiting fluctuating (*green*) and non-fluctuating (*white*) levels between contractions. (B) Change in baseline fluorescence (ΔF) averaged over entire tissue (*red*) and for ROIs in (A) over multiple contraction-relaxation cycles (fluctuating cells *green*, non-fluctuating cells *white*). The start of global contractions have been highlighted (*vertical dashed lines*). Application of nifedipine resulted in the eventual cessation of all global contractions and in some but not all local $[Ca^{2+}]_i$ fluctuations.

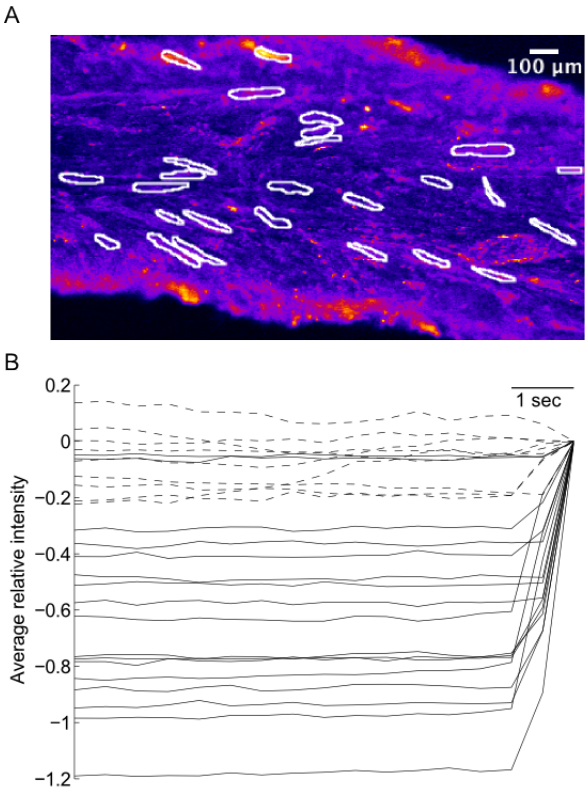

Figure 4.5: **$[Ca^{2+}]_i$ preceding contractions.** (A) ROIs encompassing cells are identified. (B) Average trace prior to contraction for each ROI. All traces have been normalised to equal zero just after the increase in $[Ca^{2+}]_i$ associated with a global contraction. Traces for cells exhibiting oscillatory behaviour indicated (*dashed lines*). Rise in $[Ca^{2+}]_i$ occurs within one second window for non-oscillating cells.

tion are shown. Each signal is the average of four pre-contraction signals, and has been normalised to have a value of zero just after the increase in $[Ca^{2+}]_i$ associated with a global contraction. The signals for the cells identified as exhibiting oscillatory behaviour in Fig. 4.3 are shown as dotted lines. The remaining ROIs encompass cells that did not exhibit visually obvious oscillations in intensity in between global contractions. There is little variation in the shape of the average intensity signals for these cells, with the suggestion that their $[Ca^{2+}]_i$ levels remain constant until a sharp rise occurs within a one second window for each cell as an action potential occurs. This behaviour is consistent with the finding of multiple and variable pacemaker sites, with no one area exhibiting consistent increases in $[Ca^{2+}]_i$ activity prior to contractions.

4.5 Oxytocin-induced single-cell signalling

In Section 1.1.3 we outlined the importance of the uterotonic hormone oxytocin in the myometrial excitation-contraction-relaxation cycle. Studies using microelectrodes (Nakao et al., 1997) and microfluorimetry combined with mechanography (Luckas et al., 1999; Longbottom et al., 2000) on strips of myometrium can demonstrate that oxytocin stimulates the myometrium by increasing the frequency, duration and force of contractions. Ca^{2+} imaging of cultured uterine myocytes have revealed oxytocin-induced repetitive $[Ca^{2+}]_i$ oscillations in individual cells (Young and Hession, 1996; Fu et al., 2000; Young and Zhang, 2001). Motion artifacts occurring in contracting tissue have meant that it has not previously been possible to investigate the relationship between the oxytocin-induced $[Ca^{2+}]_i$ oscillations in individual cells and the augmentation of phasic myometrial contractions. We conclude this chapter with analysis of single-cell calcium signalling in motion-corrected images of control and oxytocin stimulated slices . For the first time we present evidence that oxytocin induces asynchronous $[Ca^{2+}]_i$ oscillations which are similar to those observed in cultured cells. These oscillations occur between synchronous action potential driven $[Ca^{2+}]_i$ transients but appear to be unrelated to contractions.

We examined the single cell $[Ca^{2+}]_i$ dynamics in motion-corrected images of spontaneously contracting strips of myometrium over multiple contraction-relaxation cycles in control conditions (Fig. 4.6) and after application of 10nM oxytocin (Figs. 4.7 and 4.8). As a measure of the time course of contraction an ROI was placed over the moving edge of the slice in the corresponding uncorrected image sequence. The mean intensity obtained is proportional to the displacement of the slice as it moves in and out of the ROI during contraction-relaxation cycles. This displacement (L) was normalised to the highest values of intensity between contractions when the slice was fully relaxed (L_0).

The single-cell $[Ca^{2+}]_i$ dynamics in the tissue under control conditions reveal global $[Ca^{2+}]_i$ transients accompanied by contractions in all cells within the field of view (Fig. 4.6). In a small number of cells low amplitude $[Ca^{2+}]_i$ oscillations in between global $[Ca^{2+}]_i$ transients were observed. These oscillations did not propagate to neighbouring cells and had no visible impact on mechanical activity (Fig. 4.6B).

Application of 10nM oxytocin immediately and significantly increased the amplitude and duration of the global $[Ca^{2+}]_i$ transients (Figs. 4.7A and 4.8A). These changes were maintained over multiple contraction-relaxation cycles and were still evident after one hour of treatment with oxytocin (Figs. 4.7B and 4.8B). In some but not all cells, application of oxytocin also induced $[Ca^{2+}]_i$ oscillations, similar to

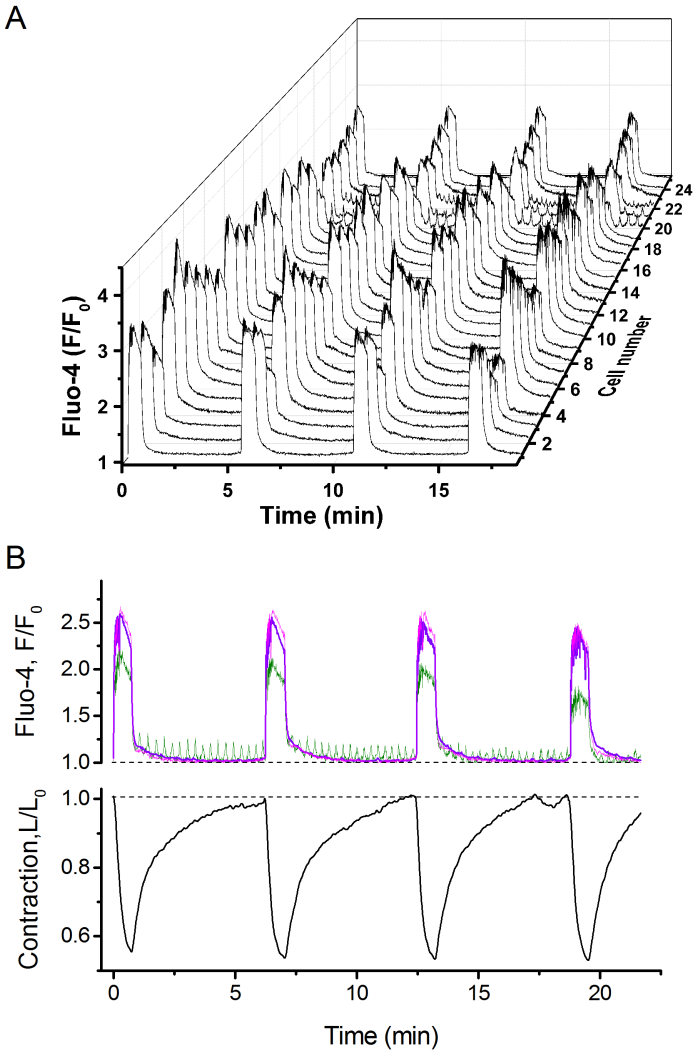

Figure 4.6: **Single cell $[Ca^{2+}]_i$ transients in spontaneously contracting human myometrium** (A) $[Ca^{2+}]_i$ transients recorded from 25 cells during four consecutive contraction-relaxation cycles (representative of 6 experiments). (B) *Upper panel:* Averaged $[Ca^{2+}]_i$ curve (*magenta trace*; average of all cells in (A)) superimposed with traces from an oscillating cell (*green trace*; cell 22 in (A)) and non-oscillating cell (*violet trace*; cell 23 in (A)). *Lower panel:* Slice displacement curve representing contractile activity.

those observed in cultured cells (Figs. 4.7A and 4.8A; Young and Hession, 1996; Fu et al., 2000; Young and Zhang, 2001). These oscillations progressively dampened and after one hour of treatment had completely disappeared (Figs. 4.7B and 4.8B). These results suggest that it is unlikely that the $[Ca^{2+}]_i$ oscillations are related to the oxytocin-induced augmentation of $[Ca^{2+}]_i$ transients; the oscillations only occur in a subset of cells and disappear while the amplitude of transients is still increasing.

In agreement with other studies (McKillen et al., 1999; Shmygol et al., 2006) the rate of tissue relaxation is significantly reduced after incubation in oxytocin (Fig. 4.8). Furthermore the rate reduction in tissue relaxation far exceeds any rate reduction in the decrease of $[Ca^{2+}]_i$. This result supports the role of oxytocin in Ca^{2+}-sensitisation of the contractile apparatus. Ca^{2+}-sensitisation occurs when inhibition of myosin light chain phosphatase (MLCP) prolongs the phosphorylation of myosin light chain (MLC), leading to enhanced tension in a Ca^{2+}-independent manner (and therefore reduced rate of relaxation).

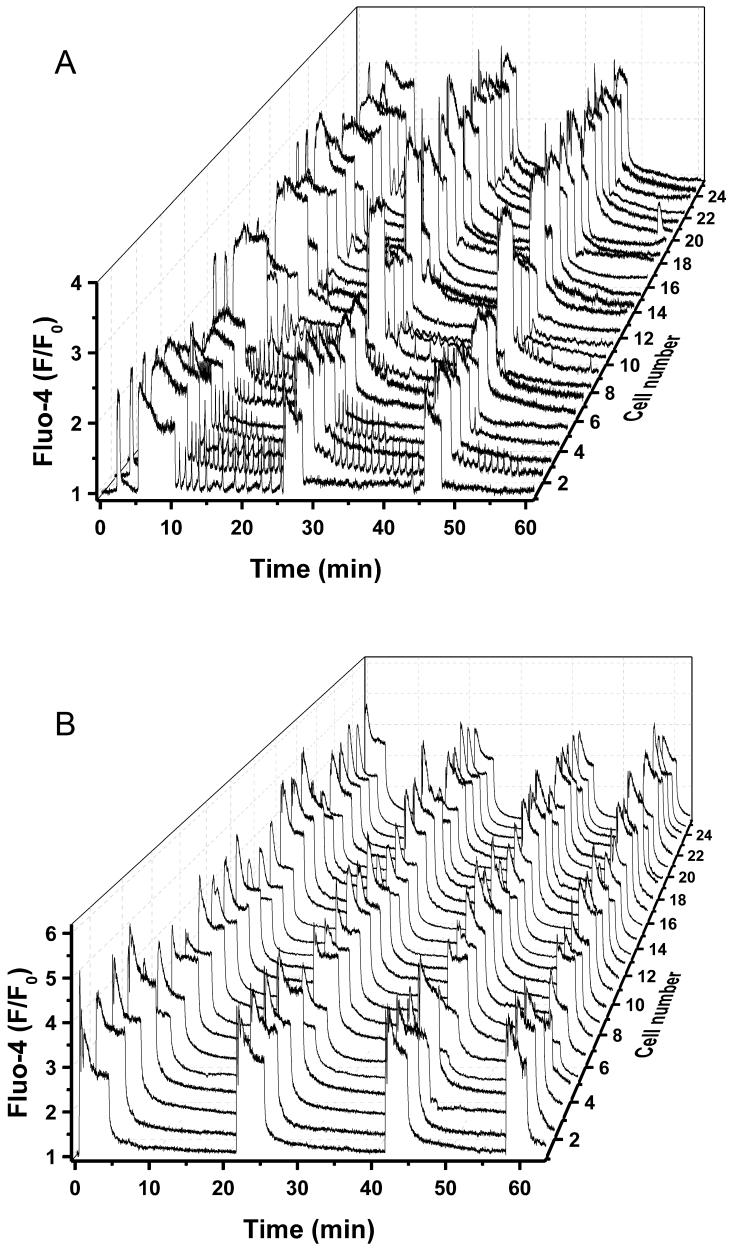

Figure 4.7: **Effects of oxytocin on $[Ca^{2+}]_i$ in myometrial slice** (A) Immediate effects of oxytocin: increase in amplitude and duration of global $[Ca^{2+}]_i$ transients and induction of $[Ca^{2+}]_i$ oscillations in some cells. Application of 10nM oxytocin started at 5min and maintained throughout. Note that the first peak is a spontaneous contraction before the oxytocin was applied. (B) Established effect of oxytocin: augmentation of global $[Ca^{2+}]_i$ transients and cessations of $[Ca^{2+}]_i$ oscillations. Same slice as in (A) after being incubated in 10nM oxytocin for one hour.

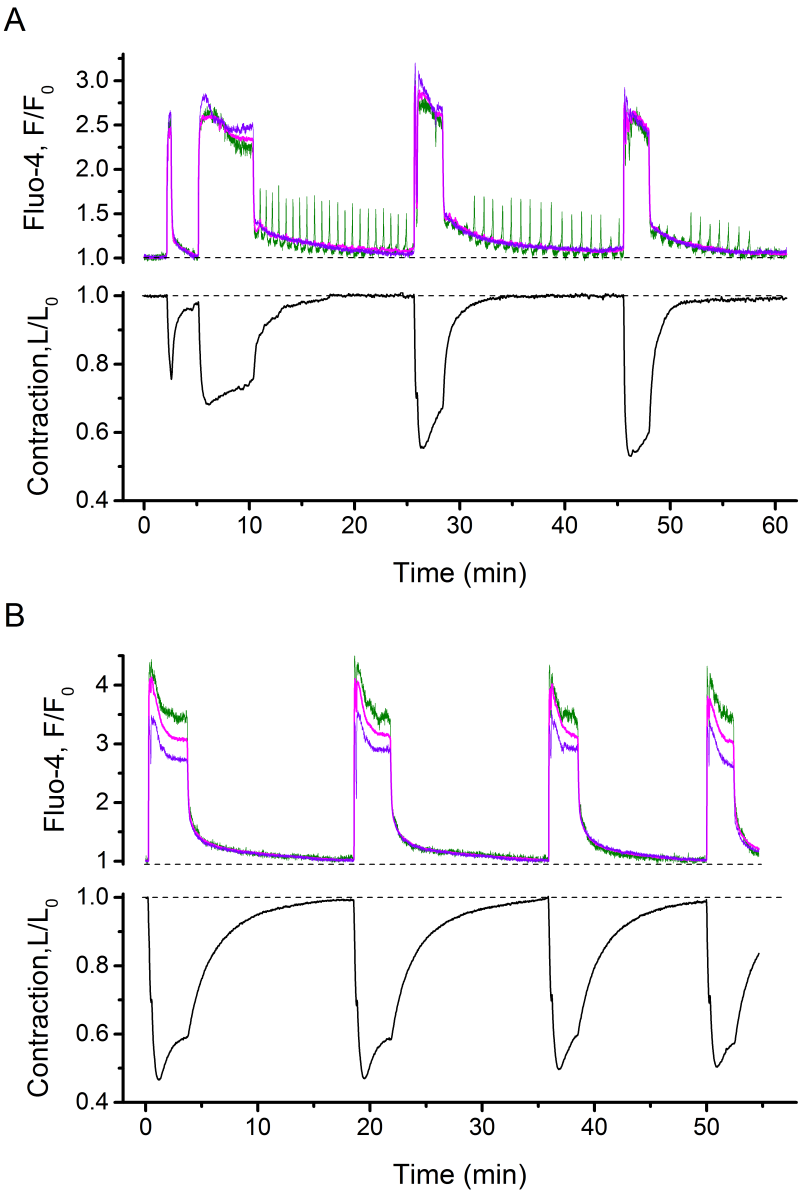

Figure 4.8: **Oxytocin-induced $[Ca^{2+}]_i$ oscillations in individual cells are short-lived but potentiation of global $[Ca^{2+}]_i$ transients and phasic contractions is long-lasting** (A) Immediate effects of oxytocin; application of 10nM oxytocin started at 5min and maintained throughout. (B) Established effect of oxytocin; same slice as in (A) after being incubated for one hour. (A, B) *Upper panels:* averaged $[Ca^{2+}]_i$ curve (*magenta trace*; averaged from all cells in Fig 4.7) superimposed with traces from an oscillating cell (*green trace*; cell 2 in Fig. 4.7 and non-oscillating cell (*violet trace*; cell 16 in Fig. 4.7). *Lower panels:* Slice displacement curve representing contractile activity.

Chapter 5

Tissue kinematics

A complete understanding of human labour requires the integration of electrical, chemical and mechanical activity at cellular, intercellular and tissue level. An integrated approach to cardiac research has lead to the development of models of cardiac contraction used clinically as diagnostic tools and to assess the effectiveness of heart operations and treatments (see Bassingthwaighte et al., 2009; Nordsletten et al., 2011 for reviews). Work has been done to model the electrodynamics of human labour, incorporating cellular and tissue level dynamics (Aslanidi et al., 2011). A similar approach integrating single cell, fasciculi and tissue level mechanics is required to effectively model the biomechanics of contracting myometrium.

A number of models have been proposed to capture the mechanics of the uterus, including single cell contraction using the Hai and Murphy (1988) model of crossbridge cycling (Bursztyn et al., 2006), fasciculus contraction (Miftahof and Nam, 2011) and organ-level contraction using various approaches, including continuum mechanics (Mizrahi et al., 1978; Irfanoglu and Karaesmen, 1993), phenomenological (Vauge et al., 2000) and finite element-based models (Weiss et al., 2004). Plausible biomechanical models of the human uterus require experimental parameters, for example stress-strain relationships. Passive mechanical properties of contracting myometrium recorded using strips of myometrium reveal nonlinear viscoelastic properties of the tissue (Conrad et al., 1966; Conrad et al., 1966; Pearsall and Roberts, 1978). There is currently a sparsity of data characterising kinematic properties and active stress-strain relationships which are needed for tissue- and organ-level modelling of contracting myometrium (Miftahof and Nam, 2011).

In this chapter we demonstrate how our motion-correction algorithm can be used to inform about kinematic properties of contracting myometrium. We exam-

ine the tissue level kinematics over multiple contraction-relaxation cycles and compare the trajectories of landmarks between different contraction-relaxation cycles and between different stages of the contraction-relaxation cycle using quantitative tracking measures. We illustrate that the data produced by our motion-correction algorithm can be used to compare the spatiotemporal profiles of tissue contraction and calcium signals. We begin by identifying a *characteristic length scale*, a key biophysical property of contracting myometrium which can inform tissue- and organ-level modelling.

5.1 Characteristic length scale

During myometrial contractions, cells structurally deform neighbouring tissue and are themselves affected by nearby contracting cells. The elastic properties, spatial organisation and force produced by contracting myocytes set the characteristic length scale λ_c below which tissue deformation during a contraction is locally homogeneous. In Section 3.5 we introduced λ_c as a spatial weighting parameter used in the extrapolation of landmark motion trajectories to estimate the movement of tissue between landmarks. Here we illustrate that the characteristic length scale is consistent across multiple datasets and therefore represents a key biophysical characteristic of contracting myometrium.

Recall that the displacement of a landmark l from its initial position in the first frame can be expressed:

$$D_l = (d_x, d_y), \tag{5.1}$$

where

$$d_x = (0, x_2 - x_1, x_3 - x_1, \ldots, x_N - x_1)^T \tag{5.2}$$

$$d_y = (0, y_2 - y_1, y_3 - y_1, \ldots, y_N - y_1)^T, \tag{5.3}$$

The distance between the tissue under a pixel p and a landmark l in the first image frame is called ϕ_{pl} and the weighting function is given by $W_{pl}(\lambda) = \exp(-\phi_{pl}/\lambda)$. A distance-weighted estimate for the displacement of the tissue under a pixel is calculated as

$$D_p(\lambda) = \frac{\sum W_{pl}(\lambda) D_l}{\sum W_{pl}(\lambda)}, \tag{5.4}$$

where the sums are over all tracked landmarks. The optimal value of λ (λ_c) is found

by comparing the prediction of equation (5.4) when the pixel p is a landmark itself for a range of different λ.

We compared the error between the known displacement of a landmark and the estimated displacement computed as a distance-weighted average of all remaining landmark displacements for a range of λ values for all landmarks in fifteen datasets (Fig. 5.1). The root-mean-square error for all landmarks over each dataset is shown for each λ value. The datasets include a number of magnifications, with pixel size between 1.76 and 4.5μm. While there is some variation in the shape of the curves, the value of λ for which the error is minimum shows much less variation between datasets.

In Fig. 5.2A the displacement of a landmark from a single dataset over 100 frames is plotted (black line) along with its displacement computed as a weighted average for three values of λ ($\lambda = 2$, 45, 1024μm; red, blue, green lines, respectively). The root-mean-square error for displacements of all landmarks in this dataset for a range λ values is shown in Fig. 5.2B, with the values used for plots in Fig. 5.2A indicated ($*$). In Fig. 5.2C the mean total error per dataset for displacements of all landmarks was computed for each λ for all datasets in Fig. 5.1, revealing a minimum total error when $\lambda = \lambda_c \sim 40$μm. Interestingly, this scale is less than the typical diameter of myocyte bundles of 100-300μm (Young and Hession, 1999), which indicates that the tissue is significantly deformed during a contraction at the scale of bundles. An illustration of the range of characteristic length is shown by the circle plotted in Fig. 5.2D which is centred around a pixel located inside ROI3 from Fig. 4.2. .

5.2 Kinematics of tissue contraction

The description of local motion at all points within an imaged tissue slice, required for the motion-correction process, contains a wealth of information about the contractile properties of the tissue. We examined the kinematics of the tissue motion over multiple contraction-relaxation cycles for datasets in which the tissue was initially allowed to spontaneously contract for four cycles and was subsequently treated with 10nM oxytocin. In Fig. 5.3A-B the trajectories of initially evenly distributed points are shown over the course of five contraction-relaxation cycles. The associated ΔF signal, averaged over the whole imaged slice is shown in Fig. 5.3E for reference. The tissue followed surprisingly stereotypical local paths for the spontaneous contractions (Fig. 5.3D, first four contraction-relaxation cycles). The application of oxytocin to the tissue in Fig. 5.3 caused a prolonged increase in $[Ca^{2+}]_i$ levels, which

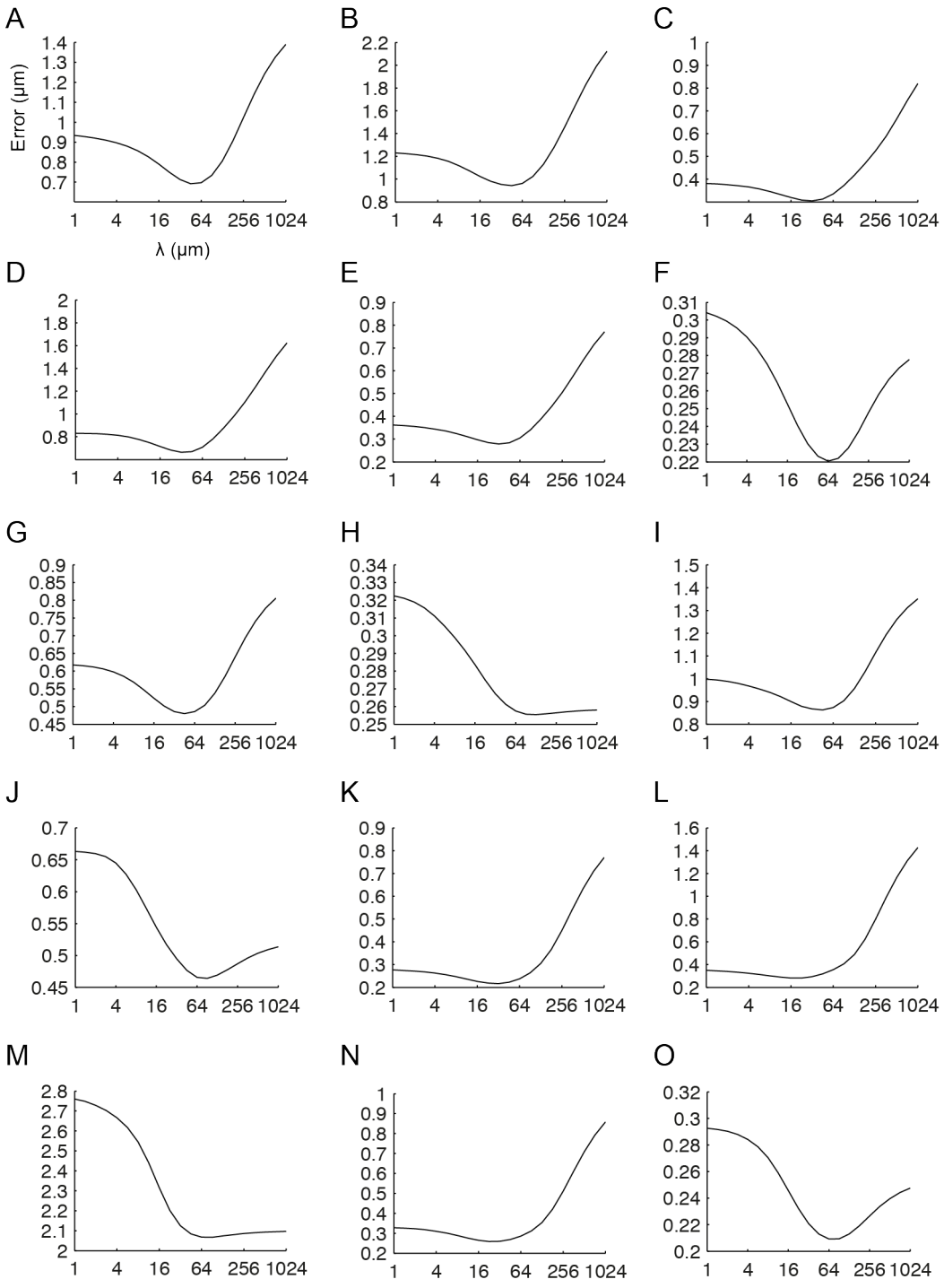

Figure 5.1: **Computation of contractile length λ_c for fifteen datasets.** (A-O) Root-mean-square error per frame for displacements of landmarks computed as weighted average of all remaining landmark displacements for each λ value. Pixel width for datasets between 1.76 and 4.5µm.

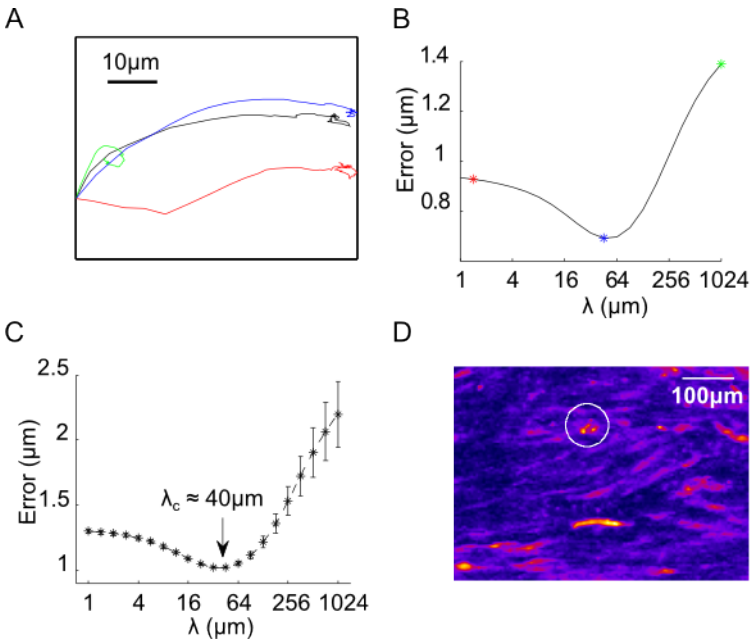

Figure 5.2: **Characteristic length scale λ_c of myometrium** (A) Displacement of a landmark from Fig. 3.1 over 100 frames (*black line*) and distance-weighted estimate of displacement computed for $\lambda = 2$, 45, 1024µm (*red, blue, green lines*, respectively). (B) Error for distance-weighted estimate computed for a range of λ values, averaged over all landmarks in Fig. 3.1. Values of λ used for plots in (A) indicated ($*$). (C) Normalised mean error per dataset for displacements of landmarks computed as weighted average of all remaining landmark displacements for variety of λ values, with a minimum at λ_c. (D) Visualisation of contractile length scale (40µm) centred around ROI3 from Fig. 4.2.

is reflected in protracted motion trajectories in some areas of the tissue (Fig. 5.3B-D). This reproducibility for the spontaneous contractions was seen in three of four datasets examined (Figs. 5.4 and 5.5). In the fourth dataset, the local contraction paths were similar for three spontaneous contractions; in the remaining cycle, a local contraction which did not propagate across the entire slice preceded the global contraction (Fig. 5.6). This local contraction initiated motion along the same local paths, but the tissue relaxed back before completing the contractile motion. Interestingly, the tissue motion during the global contraction then followed the local trajectories from midway through the contraction-relaxation cycle. The detailed measurements of local tissue trajectories that our method provides reflects the two-dimensional movement of the tissue slices comprising contractile motion and also motion artifacts resulting from the recording set-up, such as slippage of the tissue slice. However, the uniformity of motion seen in the majority of spontaneous contractions across datasets indicates a consistency in the underlying contractile mechanisms, both at cellular and network level within the tissue slice. Of further

note is the relative smoothness of motion of the tissue during the contraction phase when compared to the subsequent relaxation phase (Fig. 5.3C). Analysis of the rough, stochastic paths could potentially yield further information on the distribution and interaction of cellular mechanisms underlying muscle contraction and relaxation mechanics. In Section 5.4 we provide some examples of quantitative analysis that can be performed on the motion trajectories.

5.3 Calcium and kinematics

We used the kinematics of local motion to calculate the spatiotemporal structure of tissue contraction and compare this to the local $[Ca^{2+}]_i$ dynamics. We calculated the contraction of each 10×10μm region of tissue by using the measure $\Delta K = K_0 - K$ where K is the deformed area and K_0 the original area ($K_0 = 100\mu m^2$). Fig. 5.7 provides an example of a comparison of tissue contraction and $[Ca^{2+}]_i$ dynamics. Significant increases in ΔF (Fig. 5.7A top panels) are evident just before the accompanying changes in ΔK (Fig. 5.7A bottom panels). This can be clearly seen for a ROI (Fig. 5.7B) in which the dynamics of the $\Delta F/F_0$ signal during the rise to peak occur at a faster time scale than the $\Delta K/K_0$ dynamics (first contraction-relaxation cycle: 3 s for 20-80% $\Delta F/F_0$ compared with 9 s for $\Delta K/K_0$). It can also be noted that the onset of decrease in ΔF is evident before ΔK decreases and furthermore that the rate of decay of ΔK is significantly slower than that of ΔF (Fig. 5.7B, first contraction-relaxation cycle: 25 s for 80-20% $\Delta F/F_0$ compared with 88 s for $\Delta K/K_0$). The complexity of the structure of myometrium and the contribution this plays in the contraction of the tissue is highlighted in Fig. 5.7A: while there is broad spatial correlation between changes in fluorescence and tissue contraction, the regions exhibiting the greatest change in fluorescence are not always matched with those having the greatest levels of contraction.

The characteristics of the ΔF and ΔK transients can inform about the rates at which $[Ca^{2+}]_i$ levels increase and decrease and the associated rates of contraction and relaxation. We compared the rise and decay time constants (τ_r and τ_d respectively) of ΔF and ΔK over multiple contraction relaxation cycles for two ROIs encompassing cells (Fig. 5.8). τ_r was computed by fitting $x = A(1 - \exp\{-(t - t_0)/\tau_r\})$ to the data $x = \Delta F/F_0$ and $x = \Delta K/K_0$ for each rise to peak (Fig. 5.8A, dotted coloured lines), where t_0 is the time of rise onset and A is a constant. We found that ΔK consistently exhibited a slower rate of increase than ΔF over all contractions for both ROIs (Fig. 5.8B, ROI 1: $\tau_r = 9.88 \pm 3.05$ sec for $\Delta K/K_0$ compared with $\tau_r = 1.49 \pm 0.25$ sec for $\Delta F/F_0$; ROI 2: $\tau_r = 6.48 \pm 1.54$ sec for $\Delta K/K_0$ compared with

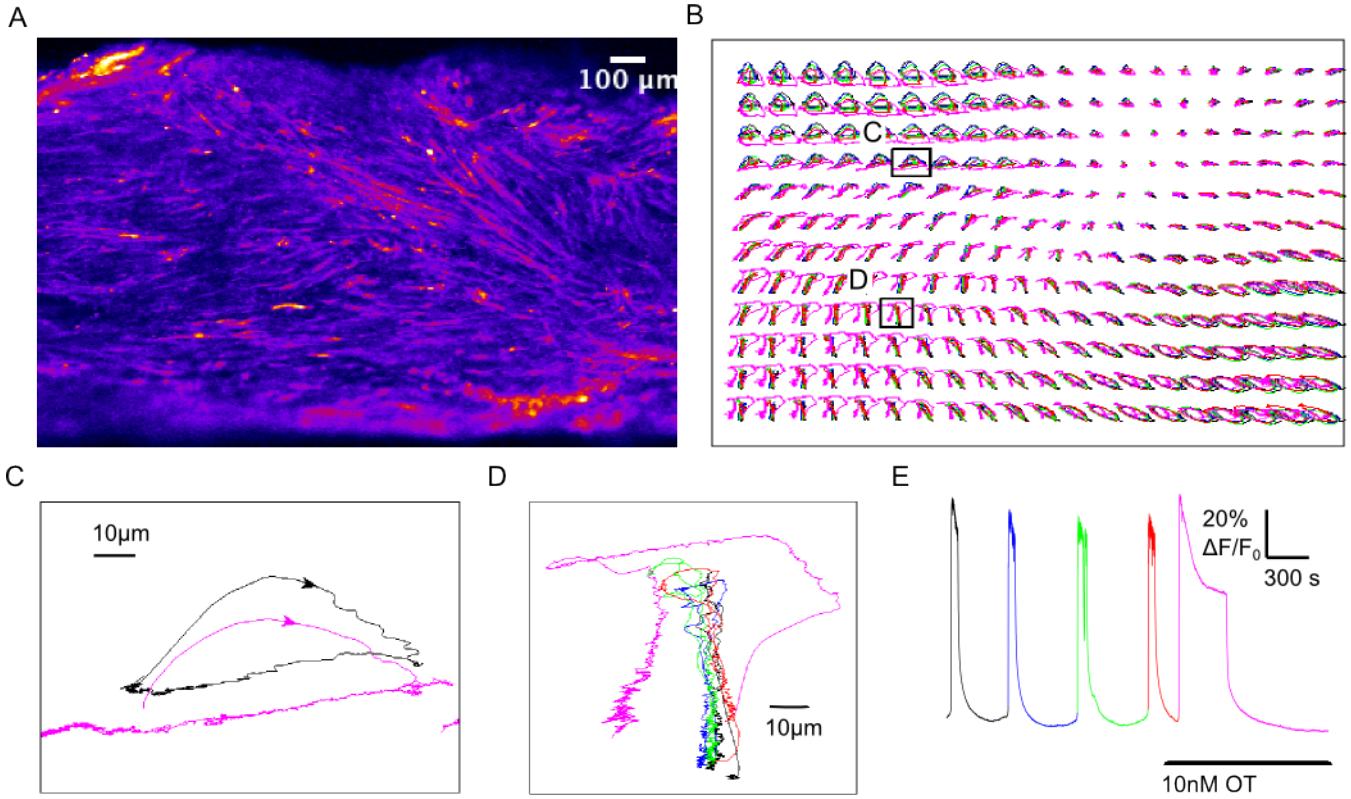

Figure 5.3: **Kinematics of local tissue motion** (A) Raw fluorescence image of a Fluo-4 loaded myometrial slice. (B) Paths of motion for evenly distributed points for five contraction-relaxation cycles. (C) Magnified subsection of panel B showing first and last contraction fields, with arrows indicating direction of motion. Note that the trajectories are smoother during the contraction phase than the relaxation phase. (D) A second magnified subsection of panel B demonstrating path consistency across the first four spontaneous contractions with a wider path taken by the stronger oxytocin-induced contraction. (E) Timecourse of the fluorescence (ΔF) averaged over entire tissue slice.

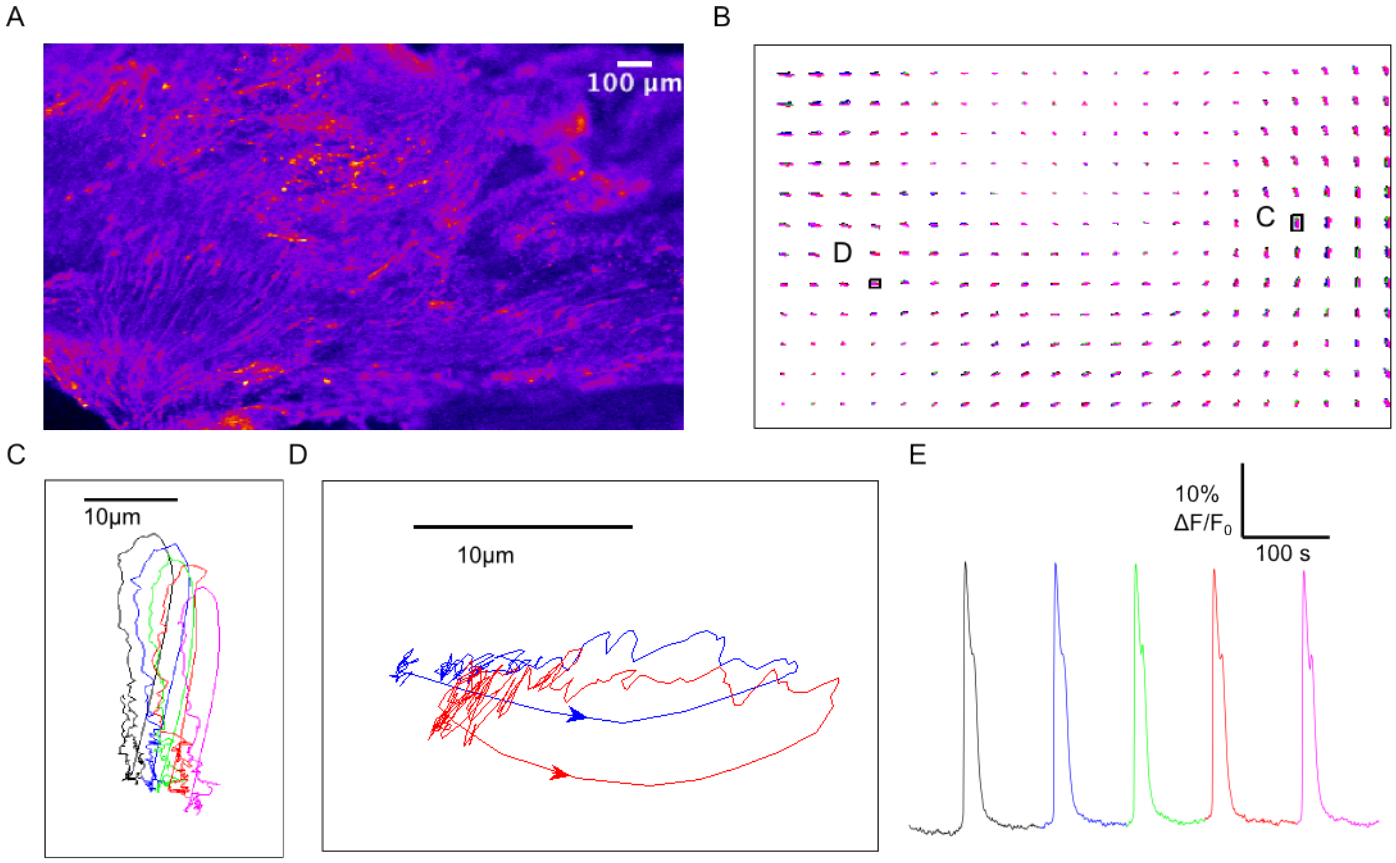

Figure 5.4: **Contraction fields in spontaneously contracting tissue** (A) Raw fluorescence image of a Fluo-4 loaded myometrial slice. (B) Paths of motion for evenly distributed points over five contraction-relaxation cycles. (C) Magnified subsection of (B). (D) Magnified subsection of (B) showing second and third contraction fields, with arrows indicating direction of motion. The motion trajectories are smoother during the contraction phase than in the subsequent relaxation phase. (E) Change in baseline fluorescence (ΔF) averaged over entire tissue slice.

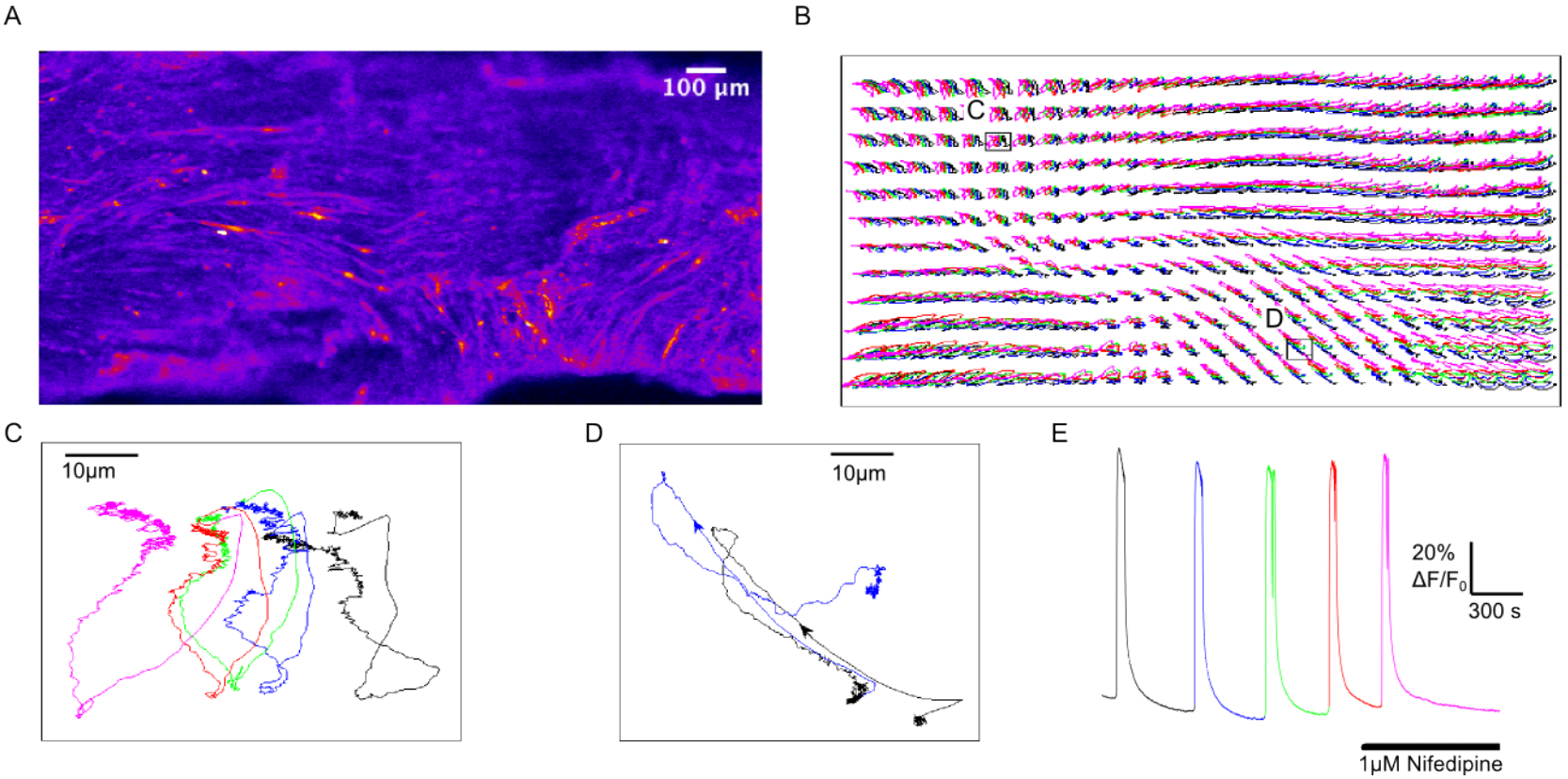

Figure 5.5: **Contraction fields in spontaneously contracting tissue** (A) Raw fluorescence image of a Fluo-4 loaded myometrial slice. (B) Paths of motion for evenly distributed points over five contraction-relaxation cycles. (C) Magnified subsection of (B). (D) Magnified subsection of (B) showing first and second contraction fields, with arrows indicating direction of motion. The motion trajectories are smoother during the contraction phase than in the subsequent relaxation phase. (E) Change in baseline fluorescence (ΔF) averaged over entire tissue slice.

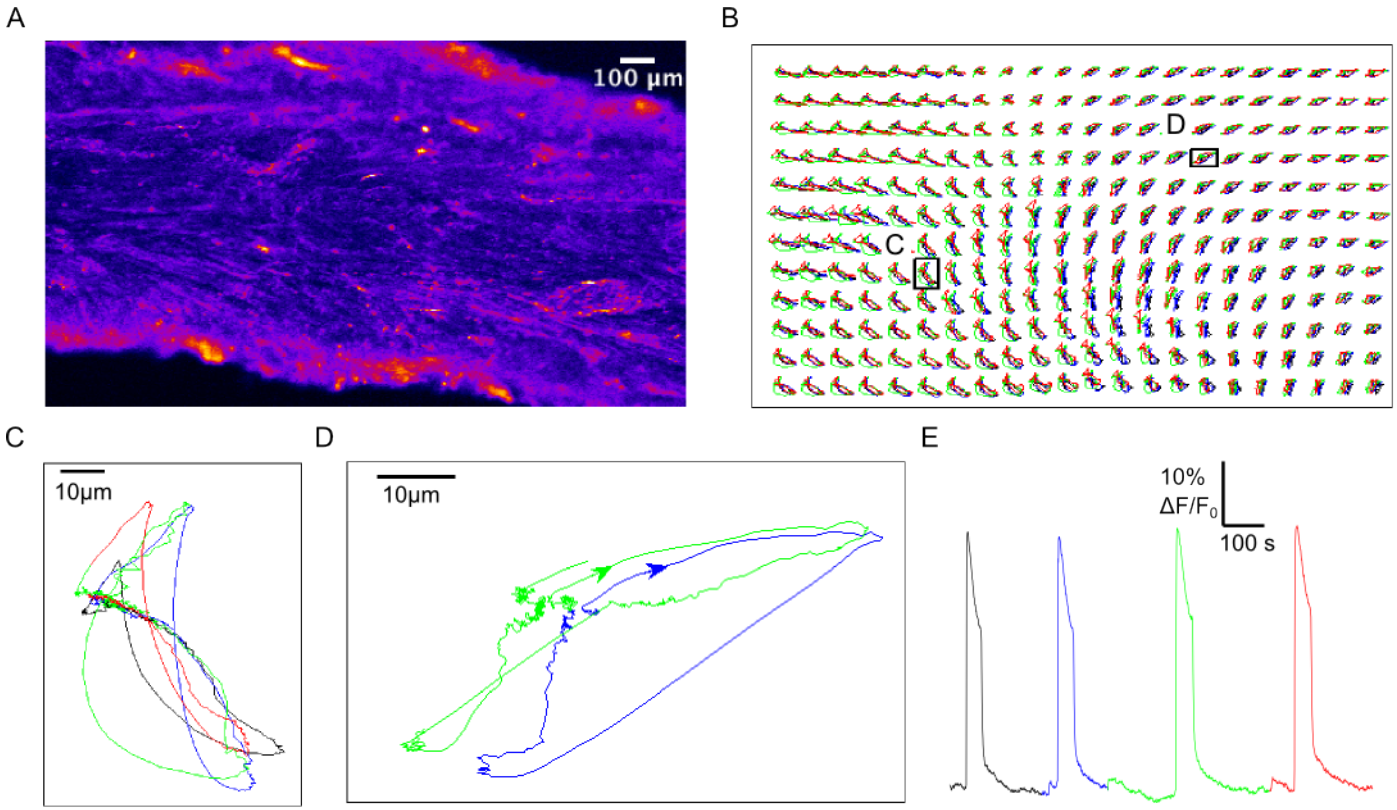

Figure 5.6: **Contraction fields in spontaneously contracting tissue** (A) Raw fluorescence image of a Fluo-4 loaded myometrial slice. (B) Paths of motion for evenly distributed points over 4 contraction-relaxation cycles. (C) Magnified subsection of (B). (C) Magnified subsection of (B) showing second and third contraction fields, with arrows indicating direction of motion. In this tissue slice, a contraction which did not propagate globally preceded the third contraction. (E) Change in baseline fluorescence (ΔF) averaged over entire tissue slice.

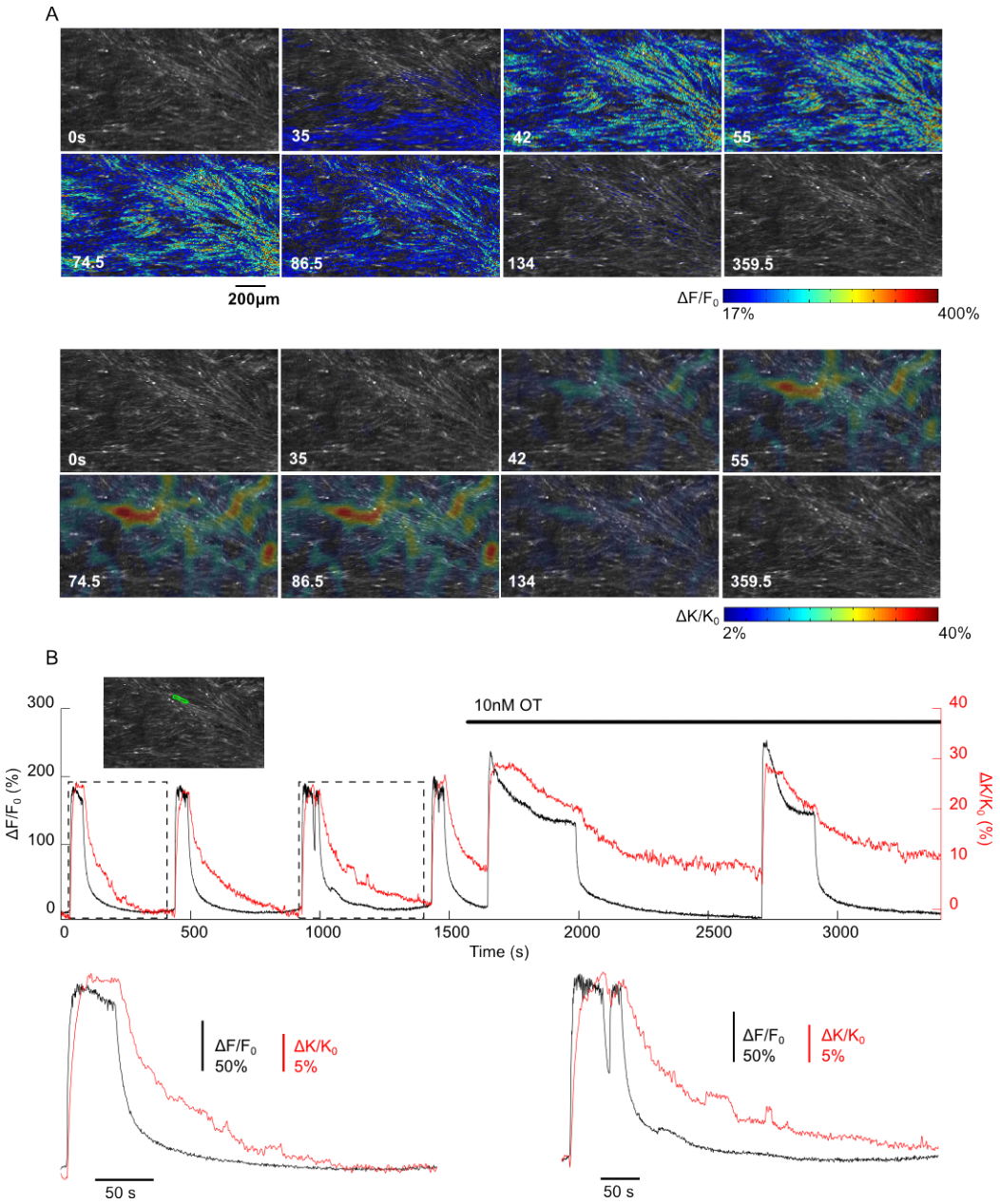

Figure 5.7: **Comparison of $[Ca^{2+}]_i$ signals and spatiotemporal contraction field** (A) Change in baseline fluorescence $\Delta F/F_0$ (*top panels*) and tissue contraction $\Delta K/K_0$ (*bottom panels*) for spontaneously contracting tissue over single contraction-relaxation cycle. Changes shown for $\Delta F/F_0 \geq 17\%$ and $\Delta K/K_0 \geq 2\%$, where thresholds are means + SDs of data in quiescent period preceding contraction. (B)Time course of $\Delta F/F_0$ and $\Delta K/K_0$ over multiple contraction-relaxation cycles for a ROI (*inset, green*). Two contraction-relaxation cycles are magnified in the two bottom panels.

$\tau_r = 1.49 \pm 0.31$ sec for $\Delta F/F_0$; data are means $\pm$ SDs for 6 contractions). There was greater variation in τ_r for ΔK between different contraction-relaxation cycles compared with ΔF for both ROIs. The rate of increase for ΔF and ΔK appeared to be unaffected by the application of oxytocin to the tissue slice for both ROIs.

The decreases in ΔF and ΔK following a contraction exhibit multicomponent exponential decays; an initial fast component followed by a slower second component. We examined the second slower time constant, τ_d, by fitting $x = \exp\{-(t - t_0)/\tau_d\}$ to the data $x = \Delta F/F_0$ and $x = \Delta K/K_0$ for the second phase of decay following the peak associated with contractions (Fig. 5.8A, solid coloured lines). The time period chosen was the one that produced the best fit to the exponential decay function; t_0 is the time selected for onset of the second decay component. Note that prior to analysis, the ΔF signals were processed to reduce the decay in the signal caused by photobleaching (by dividing ΔF by an exponential decay function, with time constant approximated by fitting an exponential decay to quiescent periods prior to contractions). Despite this pre-processing, the ΔF traces sometimes drop below the baseline (F_0), particularly in ROI2.

Across all contractions and for both ROIs, ΔK exhibited a slower rate of decay compared with ΔF (Fig. 5.8C). The rate of decay of ΔF for ROI1 appeared to be unaffected by the application of oxytocin, but ΔK exhibited a slower rate of decay in the two contractions following application of oxytocin than in the four contractions prior to application (Fig. 5.8C, upper right panel). This change in the $[Ca^{2+}]_i$-contraction relationship in the falling but not rising phase of contraction following application of oxytocin is in agreement with experimental results (Thornton et al., 1998), and supports the role of oxytocin in increasing the sensitivity of the contractile machinery to $[Ca^{2+}]_i$. ROI1 is located in the middle of a large myocyte bundle, and therefore the kinematics and calcium signals in this region are largely governed by the active contractile cells. In ROI2 the rate of decay of ΔF increases slightly in the two contractions following application of oxytocin and there is no difference in τ_d for ΔK before or after oxytocin application (though there is significant variation in τ_d over all contractions). ROI2 is located at the edge of a myocyte bundle, and the kinematics and calcium signals in this region will be governed both by the active contractile cells and the passive connective tissue. This may account for the increased variation of τ_d for both ΔF and ΔK in this region.

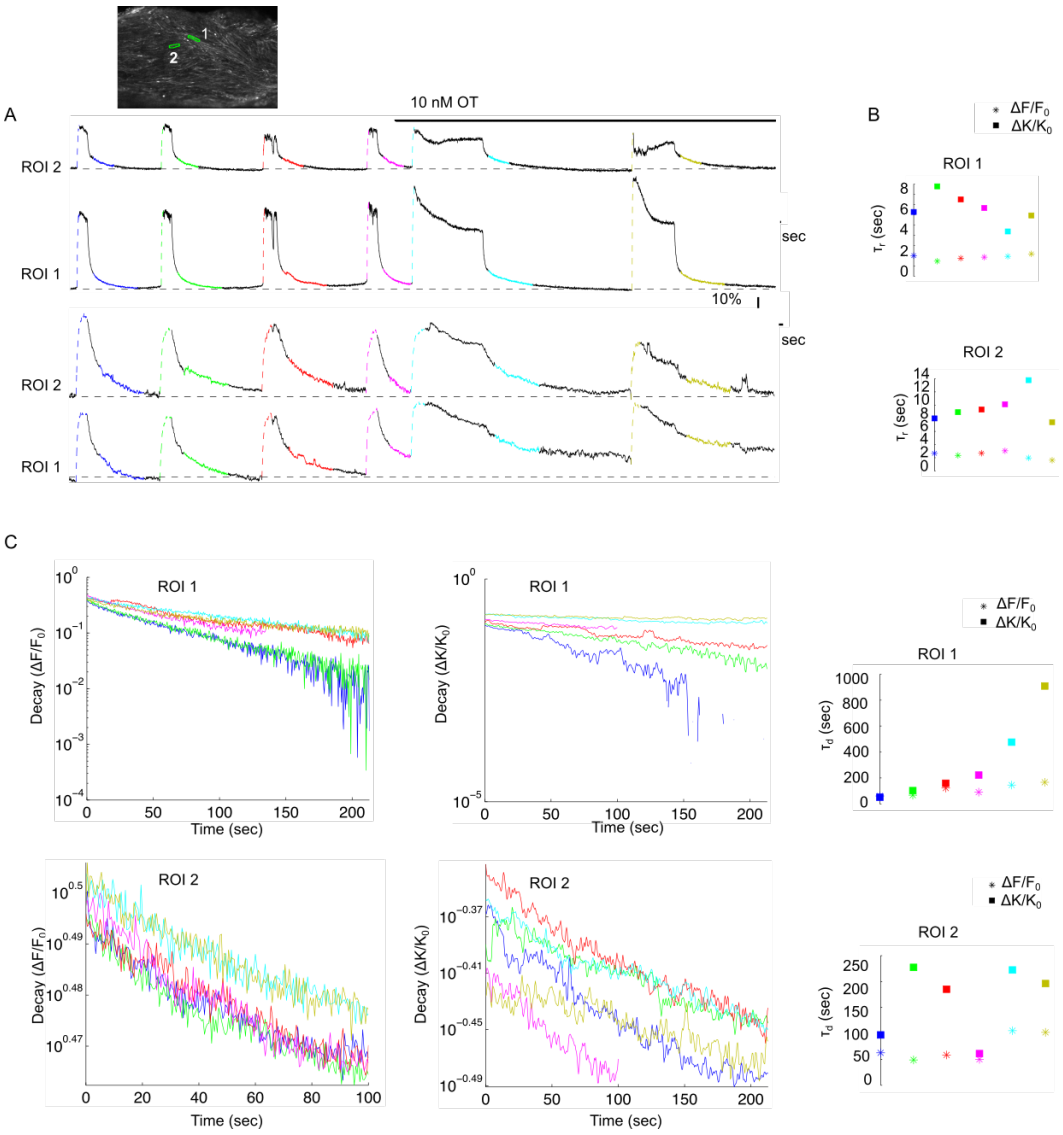

Figure 5.8: **Characteristics of $[Ca^{2+}]_i$ and contraction transients.** (A) Time course of change in baseline fluorescence $\Delta F/F_0$ (*top two plots*) and tissue contraction $\Delta K/K_0$ (*bottom two plots*) over multiple contraction-relaxation cycles for two ROIs highlighted (*top image, green ROIs*). Periods of rise to peak and decay from peak used in (B) and (C) highlighted for each contraction-relaxation cycle (*dashed coloured lines* and *solid coloured lines*, respectively). (B) Time constant τ_r governing rise to peak for $\Delta F/F_0$ and $\Delta K/K_0$ for 2 ROIs over 6 contraction-relaxation cycles (coloured coded as in (A)). $\Delta K/K_0$ exhibits slower rate of increase than $\Delta F/F_0$ over all contractions for both ROIs. (C) Decay from peak for $\Delta F/F_0$ (*left*) and $\Delta K/K_0$ (*middle*) and time constant τ_d governing decay from peak (*right*) for 2 ROIs over 6 contraction-relaxation cycles (colour-coded as in (A)). $\Delta K/K_0$ exhibits slower rate of decrease than $\Delta F/F_0$ over all contractions for both ROIs.

Measure	Definition
Total distance travelled	$d_{tot} = \sum_{i=1}^{N-1} d(\mathbf{p}_i, \mathbf{p}_{i+1})$
Net distance travelled	$d_{net} = d(\mathbf{p}_1, \mathbf{p}_N)$
Maximum distance travelled	$d_{max} = \mathsf{max}_i d(\mathbf{p}_1, \mathbf{p}_i)$
Confinement ratio	$r_{con} = d_{net}/d_{tot}$
Stochasticity ratio	$r_{stoc} = d_{max}/d_{tot}$
Mean curvilinear speed	$\bar{v} = d_{tot}/t_{tot}$
Mean straight-line speed	$v_{lin} = d_{net}/t_{tot}$

Table 5.1: **Quantitative tracking measures** The point $\mathbf{p}_i = (x_i, y_i)$ is the location of a landmark at frame $i \in \{1 : N\}$ and the distance $d(\mathbf{p}_i, \mathbf{p}_j)$ between two points $\mathbf{p}_i$ and $\mathbf{p}_j$ is taken as the Euclidean norm.

5.4 Analysis of landmark trajectories

In Section 3.8 we indicated that one of the advantages of the Gaussian-fitting method over the Lucas-Kanade template registration method for tracking landmarks is that the landmarks tracked using Gaussian-fitting are biologically identifiable; i.e., they represent small cell bodies (most likely invading leukocytes and/or myocytes damaged by slice-cutting procedure). In this section we use a number of quantitative tracking measures to compare the trajectories of these small cell bodies both between contraction-relaxation cycles and between different phases within a single contraction-relaxation cycle. The majority of the tracking measures can be found in Meijering et al. (2012); we introduce the *stochasticity ratio* as an additional measure of the noise within the trajectories (Table 5.1).

5.4.1 Comparison between contraction-relaxation cycles

We examined the trajectories of landmarks in one dataset over six contraction-relaxation cycles (Fig. 5.9). The first four contractions were spontaneous (blue tones), and the final two followed application of 10nM oxytocin (red tones). We computed the quantitative tracking measures in Table 5.1 for each of the six cycles (Figs. 5.10, 5.11 and 5.12). The landmark trajectories were produced directly using our motion-tracking algorithm, which refreshes after each contraction-relaxation cycle. Therefore while many landmarks are tracked over each cycle, there is some variability in landmark selection between cycles. All landmarks were used in the distributions shown in Figs. 5.10, 5.11 and 5.12 (top rows); for statistical analysis only the landmarks tracked over all cycles were used (bottom rows).

We found that the total distance and net distance travelled by landmarks over one cycle increased significantly following the application of oxytocin (Fig. 5.10A,

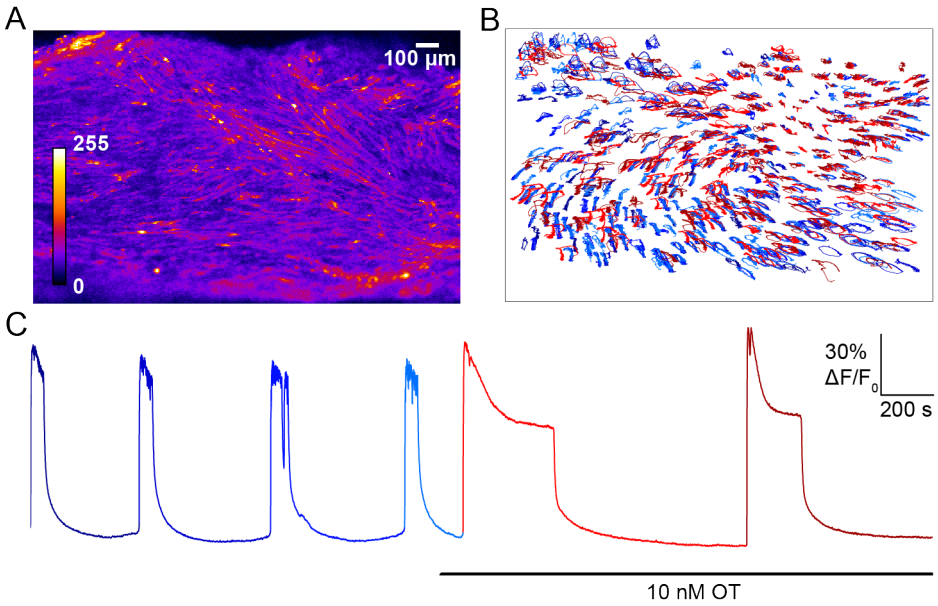

Figure 5.9: **Trajectories of landmarks tracked over six contraction-relaxation cycles.** (A) Raw fluorescence image of a Fluo-4 loaded myometrial slice. (B) Trajectories of all landmarks tracked over six contraction-relaxation cycles, colour-coded according to cycle number. Note that the as the algorithm refreshes after each contraction-relaxation cycle, there is variability between landmarks identified for tracking over each cycle. (C) Change in baseline fluorescence (ΔF) averaged over entire tissue slice, colour-coded as in (B). Note that spontaneous contractions are shown in blue tones and oxytocin-induced contractions are shown in red tones.

B). This is in agreement with the protracted motion trajectories seen in Fig. 5.3 following oxytocin application. This is further supported by a decrease in the stochasticity ratio following application of oxytocin; a higher stochasticity ratio measured over a contraction-relaxation cycle represents a more direct trajectory. The total distance travelled by landmarks during the spontaneous contraction immediately preceding oxytocin application is significantly less than the distance travelled during the first three spontaneous contractions. The net distance travelled by landmarks during this cycle is significantly greater than during the first three cycles, indicating that the end position of the landmarks is further away from their starting point. Together these results suggest that this tissue has not fully relaxed in the fourth cycle when the application of oxytocin induces the next contraction. The confinement ratio (Fig. 5.11A) when taken over an entire contraction-relaxation cycle provides another indication of how far a landmark's end point is to its start point; the higher the ratio, the greater the distance between the two points. The confinement ratio for the fourth spontaneous contraction is significantly higher than for the first three spontaneous contractions, further supporting that the tissue does not completely relax during this cycle. This result supports previous experiments showing incomplete tissue relaxation following oxytocin application (Shmygol et al., 2006).

The total distance travelled by landmarks during the first oxytocin-induced contraction is significantly greater than the distance travelled during the second oxytocin-induced contraction (Fig. 5.10A). This is not surprising, as the contraction-relaxation cycle lasts longer in the first oxytocin-induced cycle than the second (see ΔF plot in Fig. 5.9C). The area under the ΔF curve is much greater for the first oxytocin-induced contraction, and this is associated with the increase in $[Ca^{2+}]_i$ and greater force behind oxytocin-induced contractions (Nakao et al., 1997). The net distance travelled in the first oxytocin-induced contraction is higher than in the second and the confinement ratio for the first cycle is higher (Figs .5.10, 5.11). This could be due to experimental conditions (e.g., tissue slippage) or it may represent a biophysical property of oxytocin-induced contractions. The tissue in the first contraction may have not relaxed back to its pre-contraction state, or the extra force generated during this contraction may deform the tissue slightly. There is also significant variation between the net distances and the confinement ratios in the first three spontaneous contractions; further analysis would be required to investigate whether this variation is found within other datasets.

There is no significant change in the mean curvilinear speed between all spontaneous contractions and oxytocin-induced contractions or within each group (Fig. 5.12A). This would suggest that the increase in force generated by oxytocin-

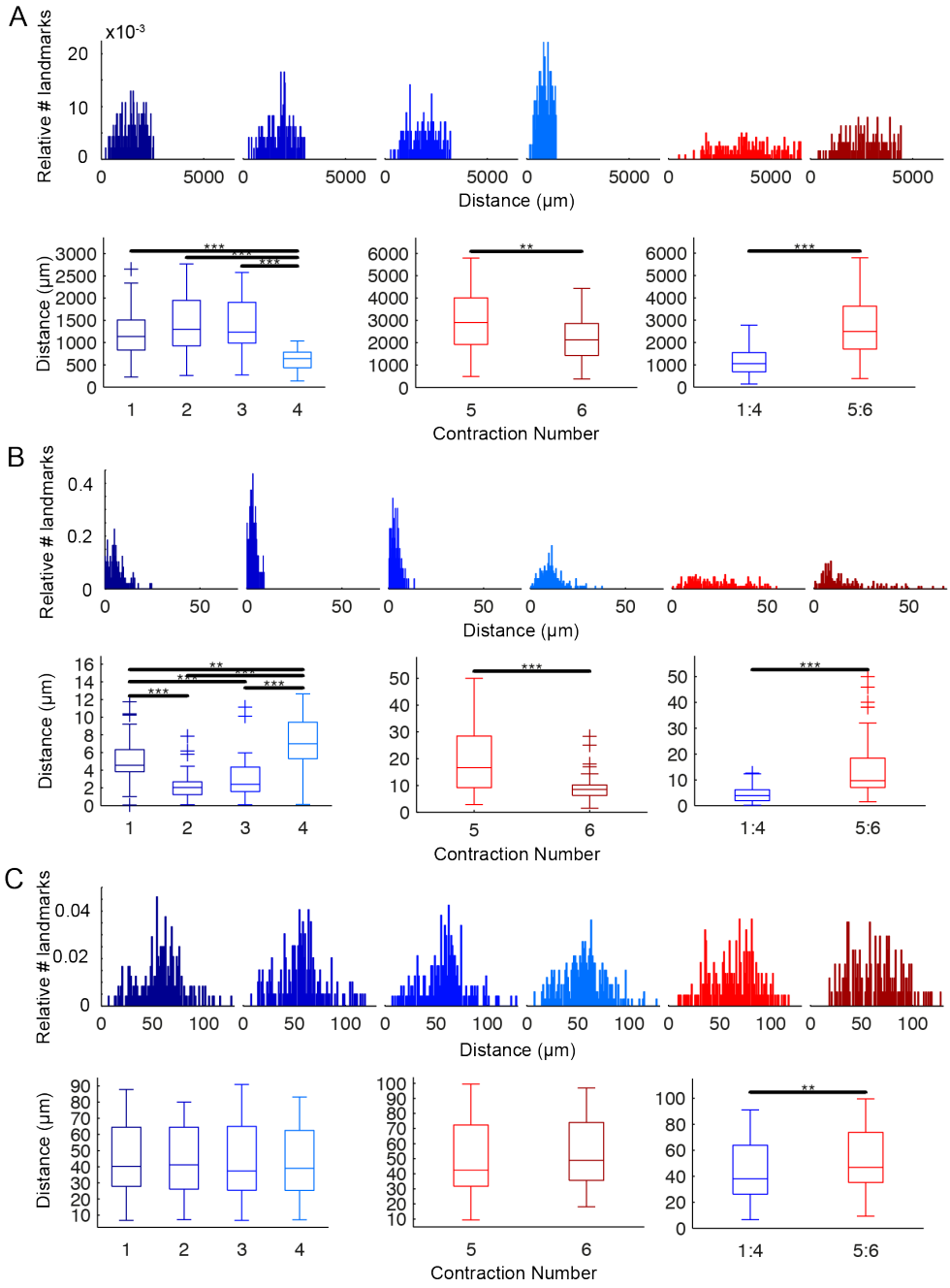

Figure 5.10: **Increase in distance travelled by landmarks during oxytocin-induced contractions** Statistics showing (A) total distance (B) net distance and (C) maximum distance travelled during six contraction-relaxation cycles. (A, B, C) *Top:* Distributions of landmark distances over six contraction-relaxation cycles. *Bottom:* Comparison of distance travelled by the same 36 landmarks (*left*) between first four spontaneous contraction-relaxation cycles; (*middle*) between two contraction-relaxation cycles following application of 10nM OT; and (*right*) between all spontaneous cycles and all oxytocin-induced cycles. *$P < 0.05$, **$P < 0.01$, ***$P < 0.001$, Wilcoxon rank-sum test.

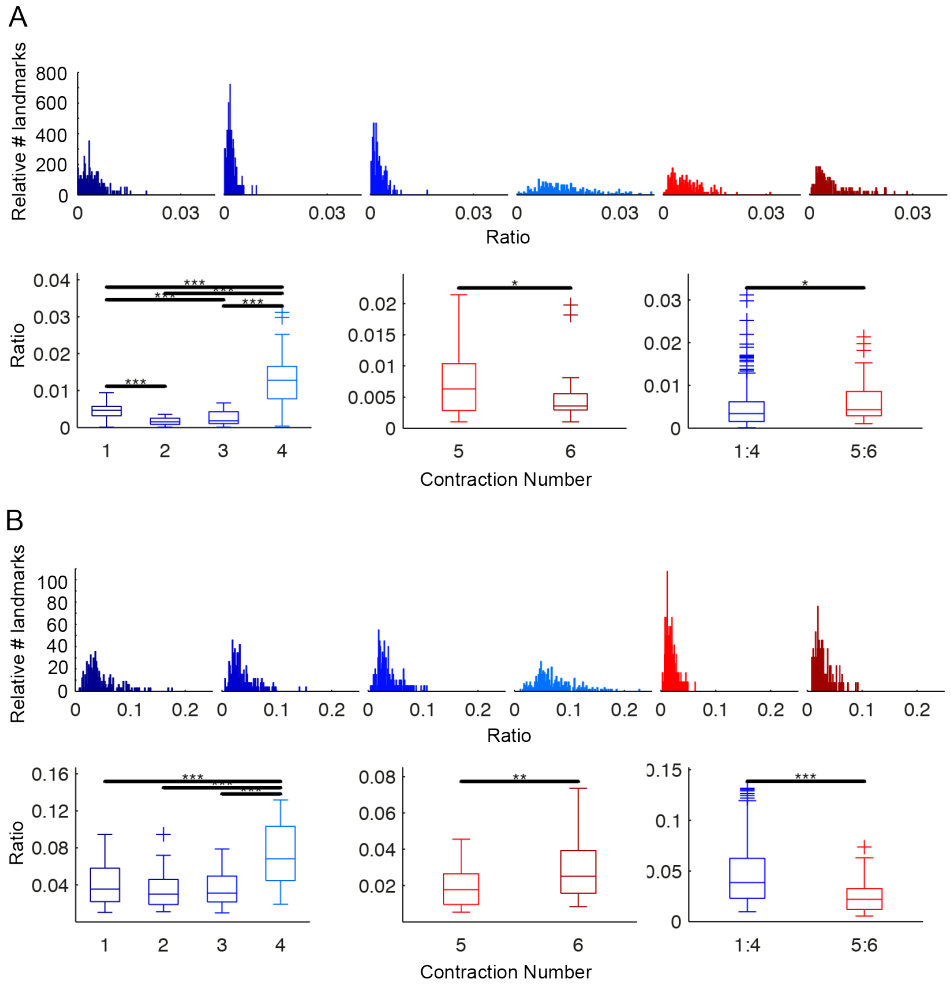

Figure 5.11: **Landmark trajectories are less direct and end further away from starting point in oxytocin-induced contraction-relaxation cycles** Statistics showing (A) confinement ratio and (B) stochasticity ratio for landmarks during six contraction-relaxation cycles. (A, B, C) *Top:* Distributions of landmark ratios over six contraction-relaxation cycles. *Bottom:* Comparison of ratios by the same 36 landmarks (*left*) between first four spontaneous contraction-relaxation cycles; (*middle*) between two contraction-relaxation cycles following application of 10nM OT; and (*right*) between all spontaneous cycles and all oxytocin-induced cycles. *$P < 0.05$, **$P < 0.01$, ***$P < 0.001$, Wilcoxon rank-sum test.

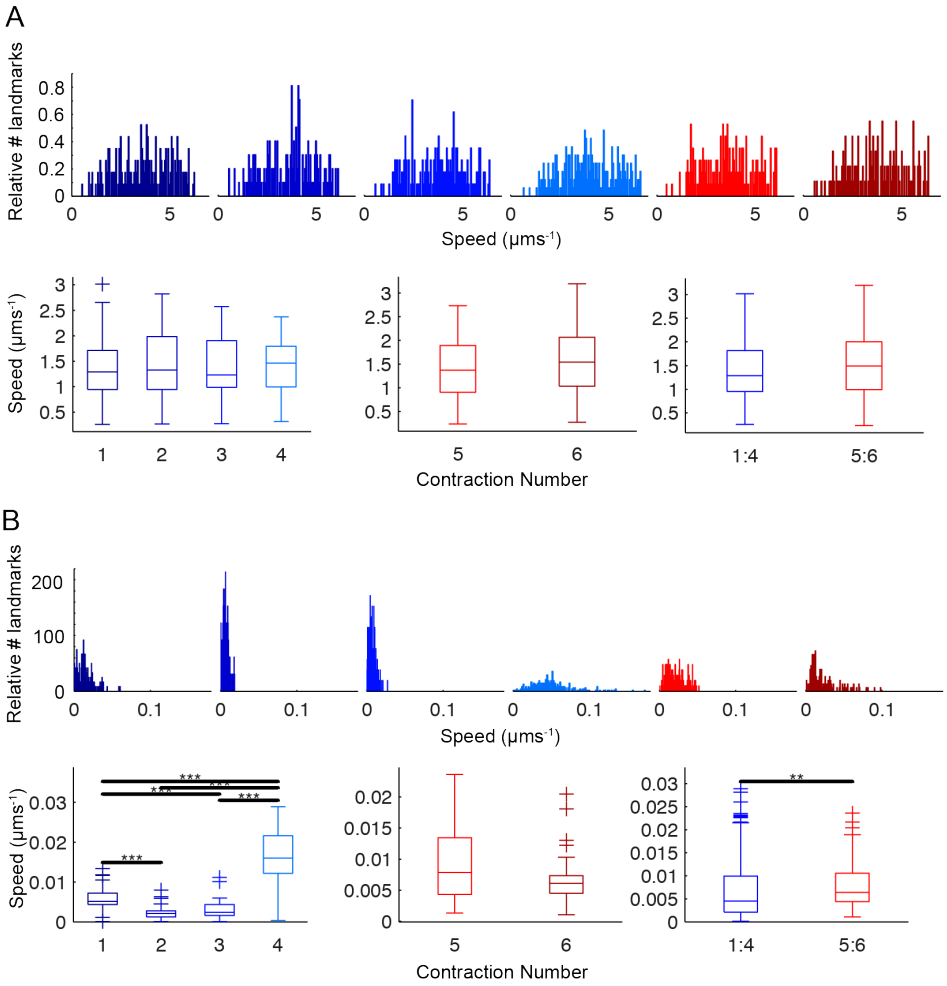

Figure 5.12: **No change in average speed of landmarks between spontaneous and oxytocin-induced contractions** Statistics showing (A) mean curvilinear speed and (B) mean straight-line speed for landmarks during six contraction-relaxation cycles. (A, B, C) *Top:* Distributions of landmark speeds over six contraction-relaxation cycles. *Bottom:* Comparison of speeds by the same 36 landmarks (*left*) between first four spontaneous contraction-relaxation cycles; (*middle*) between two contraction-relaxation cycles following application of 10nM OT; and (*right*) between all spontaneous cycles and all oxytocin-induced cycles. *$P < 0.05$, **$P < 0.01$, ***$P < 0.001$, Wilcoxon rank-sum test.

Measure	Definition
Instantaneous speed	$v_i = d(\mathbf{p}_{i-1}, \mathbf{p}_i)/\Delta t$
Instantaneous confinement ratio	$r_{con,i} = d(\mathbf{p}_1, \mathbf{p}_i)/\sum_{j=1}^{i-1} d(\mathbf{p}_j, \mathbf{p}_{j+1})$

Table 5.2: **Instantaneous tracking measures** The point $\mathbf{p}_i = (x_i, y_i)$ is the location of a landmark at frame $i \in \{2 : N\}$ and the distance $d(\mathbf{p}_i, \mathbf{p}_j)$ between two points $\mathbf{p}_i$ and $\mathbf{p}_j$ is taken as the Euclidean norm. Δt is the time interval in seconds between two consecutive frames.

induced contractions occurs only via protraction rather than protraction and an increase in the velocity of the contraction. However, these results include the entire contraction-relaxation cycle, and an increase in velocity of contraction may therefore not be detected. It would be interesting to apply quantitative measures to the contraction phase of the cycle only to elicit whether a change in velocity of contraction is detected following application of oxytocin.

5.4.2 Comparison between clusters

Myometrial tissue contains both the contractile myocytes and non-contractile connective tissue. The contractile elements will exhibit peaks in their ΔF traces associated with the influx of $[Ca^{2+}]_i$ triggering the contractile machinery. We used a shape-based clustering algorithm (Yang and Leskovec, 2011) to divide our landmarks into five clusters based on the ΔF transients of $(2r + 1) \times (2r + 1)$ pixel windows ($r = 3$) centred on each landmark over a single spontaneous contraction-relaxation cycle (Fig. 5.13). The contraction-relaxation cycle can be divided into phases to allow a comparison between the motion of landmarks between tissue contraction and relaxation. We used two instantaneous tracking measures, *instantaneous speed* and *instantaneous confinement ratio*, to split the the cycle into three distinct phases: an initial fast contraction phase; a slower contraction phase; and a long relaxation phase (Table 5.2, Fig. 5.14).

We compared the quantitative tracking measures in Table 5.1 for the landmarks in each cluster to see whether any differences emerged between the different clusters (Figs. 5.15, 5.16, 5.17). It is notable that the net distance and maximum distance travelled by landmarks in Cluster 2 (green) are significantly less than for landmarks in all other clusters during the first and third phases of the cycle (Fig. 5.15B, C). The ΔF traces for the landmarks in this cluster exhibit much less of a rise associated with the influx of $[Ca^{2+}]_i$ into myocytes than those in all other clusters (Fig. 5.13C). This suggests that the landmarks in Cluster 2 tend to belong to tissue that is less active in the contractile process. The total distance travelled by

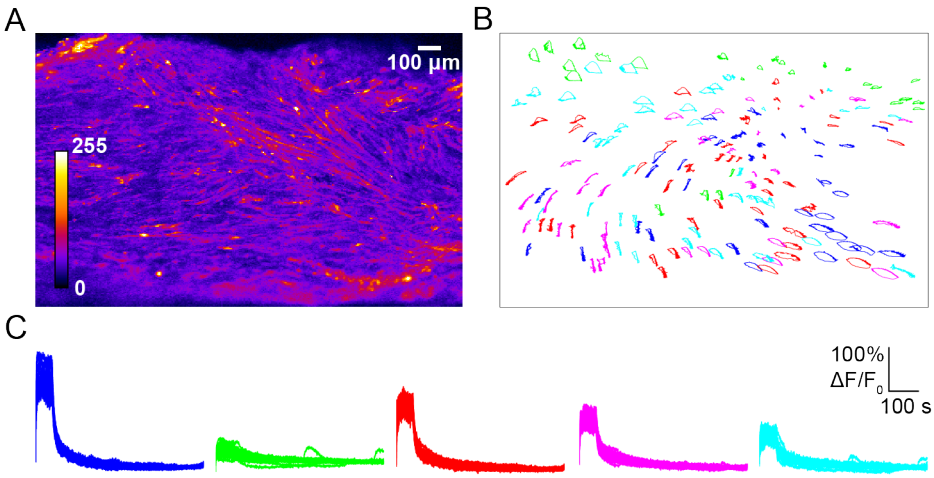

Figure 5.13: **Landmarks are grouped into clusters based on ΔF signal** (A) Raw fluorescence image of a Fluo-4 loaded myometrial slice. (B) Landmark trajectories over single spontaneous contraction-relaxation cycle, colour-coded according to cluster. (C) Change in baseline fluorescence (ΔF) of $(2r+1)\times(2r+1)$ pixel window surrounding each landmark ($r = 3$), grouped into five clusters. Colours as in (B).

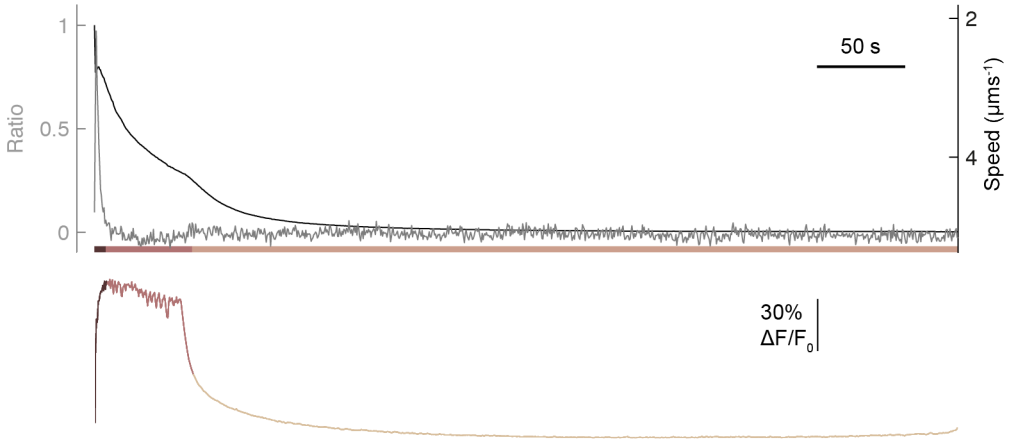

Figure 5.14: **Contraction-relaxation cycle is divided into three phases** *Top*: Mean instantaneous confinement ratio (*light grey*) and mean instantaneous speed (*dark grey*), averaged over all landmarks in Fig. 5.13 over one contraction-relaxation cycle. The cycle is divided into three phases, indicated by the colour-bar at the bottom of the plot: (L-R) fast contraction phase; slower contraction phase; and long relaxation phase. *Bottom:* Change in baseline fluorescence (ΔF) averaged over entire tissue, colour-coded according to phase.

landmarks belonging to this cluster is less than in the remaining clusters during the first and third phases of the cycle, but this is only significant for Cluster 1 (blue, first and third phases) and Cluster 3 (red, first phase). Together these results indicate that the landmarks in Cluster 2 are taking a less direct route during the first contraction phase and the relaxation phase than the landmarks in the remaining clusters. This is supported by looking at the mean straight-line speed; the speed of landmarks in Cluster 2 is significantly slower than that of landmarks in all other clusters (Fig. 5.17B, first and third phase). The movement of the tissue that is not active in the contractile process will be pulled by the surrounding contractile elements, and often in opposing directions. This may account for the trajectories of landmarks in Cluster 2 being less direct during the first and third phases. A smaller confinement ratio and stochasticity ratio would further support this claim; however there is no significant difference between the ratios of Cluster 2 and any of the other clusters. Further research would be required to determine whether these differences in distance and speed are linked to the differences in $\triangle$F signals.

The results show little variation between clusters during phase 2 for any of the tracking measures. This is not surprising; phase 2 represents the 'plateau' of the action potential, a period of stability between contraction and relaxation where the phosphorylation and dephosphorylation of myosin light chain is in equilibrium. During this time we would not expect to see a difference in the kinematic properties of the active and passive myometrial components.

In Section 5.2 we noted that the movement of the tissue appeared to be smoother during the contraction phase than during the subsequent relaxation phase. This is supported by a dramatic decrease in the confinement ratios and stochasticity ratios of all clusters between the first and third phases, indicating noisier less direct trajectories in the relaxation phase compared to the contraction phase. The mean straight-line speed decreases dramatically for all clusters between the first and third phase; the mean curvilinear speed drops between the first and third phase, but the drop is less dramatic than that of the mean straight-line speed. These results further support that the motion of the tissue is noisier during the relaxation phase than during the contraction phase.

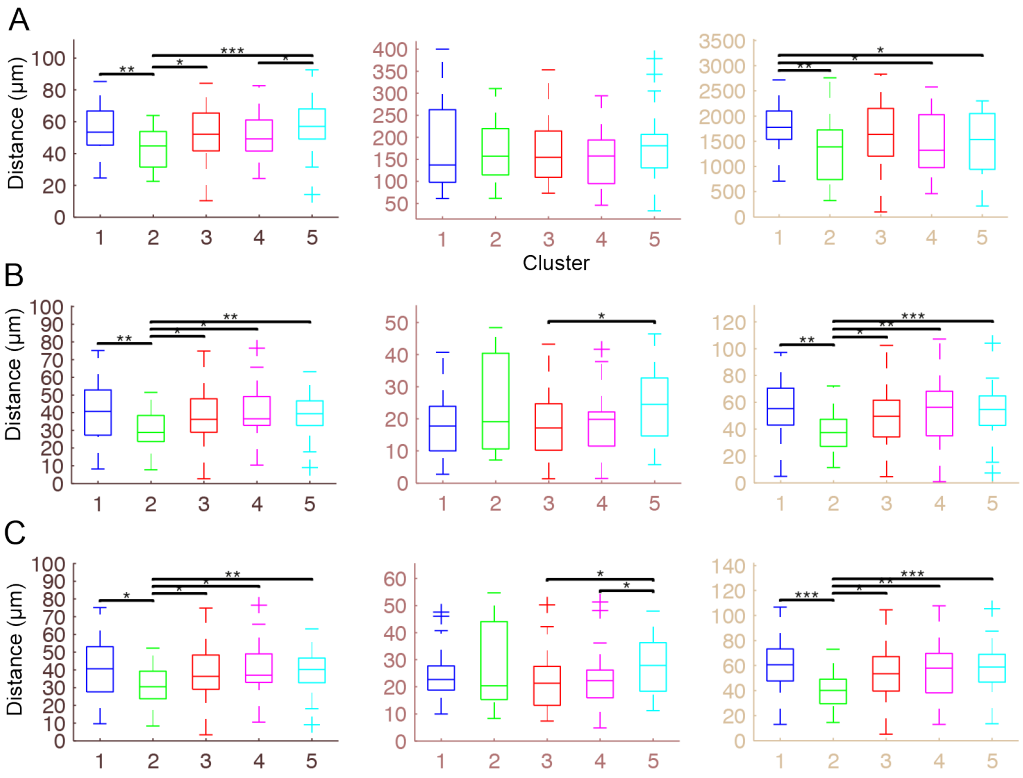

Figure 5.15: **Comparison of distance travelled by landmark clusters during three cycle phases** Box plots showing (A) total distance; (B) net distance; and (C) maximum distance of landmarks. Clusters are colour-coded as in Fig. 5.13. (L-R) fast contraction phase; slower contraction phase; and long relaxation phase. *$P < 0.05$, **$P < 0.01$, ***$P < 0.001$, Wilcoxon rank-sum test.

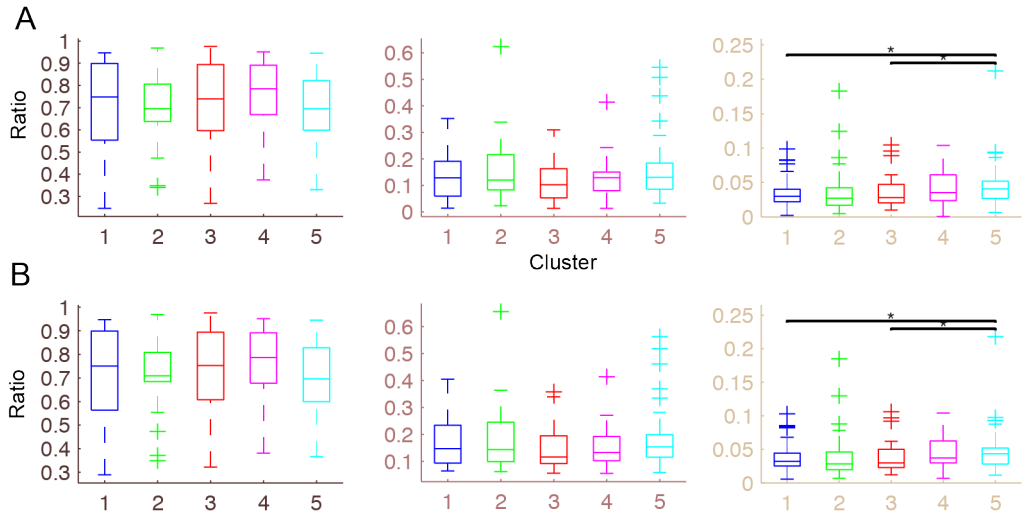

Figure 5.16: **Comparison of measures of noise in landmark trajectory clusters during three cycle phases** Box plots showing (A) confinement ratio and (B) stochasticity ratio for landmarks. Clusters are colour-coded as in Fig. 5.13. (L-R) fast contraction phase; slower contraction phase; and long relaxation phase. *$P < 0.05$, **$P < 0.01$, ***$P < 0.001$, Wilcoxon rank-sum test.

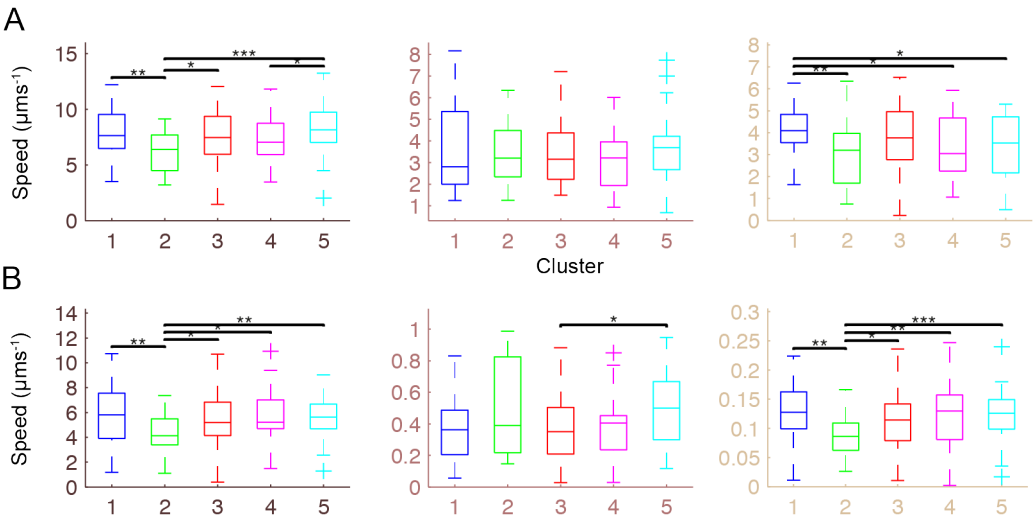

Figure 5.17: **Comparison of speed of landmark clusters during three cycle phases** Box plots showing (A) mean curvilinear speed and (B) mean straight-line speed for landmarks. Clusters are colour-coded as in Fig. 5.13. (L-R) fast contraction phase; slower contraction phase; and long relaxation phase. *$P < 0.05$, **$P < 0.01$, ***$P < 0.001$, Wilcoxon rank-sum test.

Chapter 6

Conclusions and further work

Preterm birth, uterine dystocia and postpartum haemorrhage remain significant risks during childbirth and the development of more successful treatments is critical for improved outcomes. Uterine contractility, its timing and regulation, underlies all of these problems. There has been significant progress in the understanding of uterine contractility, including the mechanisms governing contraction-initiating action potentials (Shmigol et al., 1998), the increased electrical connectivity between myocytes at term (Garfield et al., 1977) and the role of neurohypophysial hormones in parturition (Arrowsmith and Wray, 2014). However, a complete understanding of the electrical, chemical and mechanical processes governing the dynamic and complex process of uterine contractility is still a long way off. Identification of pacemaker activity and the mechanisms underlying the initial depolarisation of the cell sufficient for $[Ca^{2+}]_i$ mediated action potentials have yet to be elucidated (Duquette et al., 2005). Increased knowledge of these processes could allow better targeting for preterm and dysfunctional labour. Similarly a more complete picture of the role oxytocin plays in human parturition is essential for improvements in the success rate of its clinical application. Gaps in understanding of the structural, kinematic and mechanical properties of contracting myometrium limit the progress in development of plausible biophysical tissue-level and organ-level models required to better understand uterine contractility (Weiss et al., 2006; Miftahof and Nam, 2011)

In this thesis I address a major limitation of a key method for investigating the mechanisms underlying uterine contractility: the loss of spatial resolution caused by motion artifacts. I present an algorithm that tracks the motion of contracting myometrium during local $[Ca^{2+}]_i$ intensity changes. The imaged tissue slices used in this study contained multiple myocyte bundles separated by interstitial space and thus exhibited significant heterogeneity of movement. The method corrects mo-

tion artifacts down to the pixel level throughout the imaged slices, resulting in a 50-fold increase in effective spatial resolution. It therefore allows for a significant improvement in the quality of spatiotemporal information that can be extracted from contracting myometrium. I demonstrated how the method can be used to measure local changes in calcium indicator fluorescence, examine spatiotemporal correlations in these signals and identify heterogeneous behaviour within tissue, including inter-contraction oscillations and localised calcium increases in a subregion of the myometrium that do not trigger global contractions. As well as analysing the calcium signal itself, the motion-correction algorithm provides a full description of the kinematics of motion: a characteristic length scale λ_c $\sim$40μm below which the tissue remains locally homogeneous during a contraction was identified and spatiotemporal patterns of contraction intensity and their time courses were extracted and compared with the concurrent local calcium signals. The method makes possible novel analyses of calcium indicator fluorescence imaging data in greatly improved spatiotemporal detail. In the hope that it will be useful to researchers analysing these and similar datasets, freely modifiable code written in the MATLAB environment was published under the GNU General Public license (see Appendix).

6.1 Single-cell calcium signals

Understanding local heterogeneities in $[Ca^{2+}]_i$ activity in contracting myometrium may be key to elucidating the mechanisms governing the initiation of spontaneous contractions. Simultaneous measurements of local calcium indicator fluorescence transients taken from multiple regions of contracting tissue provide a way to characterise the spatial heterogeneity of $[Ca^{2+}]_i$ activity. Our method allowed us to measure calcium indicator fluorescence transients during and between contractions at the subcellular level, in which the choice of cells was not restricted by tissue motion. Care must be taken when interpreting calcium indicator fluorescence imaging data for contracting tissue: changes in tissue thickness and the effect of spatial averaging contribute to the challenge of reliably inferring relative changes in $[Ca^{2+}]_i$ from fluorescence changes. These limitations are discussed in more detail below. However, our measurements allowed us to detect both correlated and uncorrelated fluctuations in intensity between peaks associated with global contractions in different tissue regions, which provide information about the electrical connectivity of the network.

We found evidence that $[Ca^{2+}]_i$ entry through L-type channels is one, but not the only, mechanism underlying the asynchronous fluctuations in $[Ca^{2+}]_i$ occurring

in subpopulations of cells between global contractions (see also Bru-Mercier et al., 2012). It is possible that Ca^{2+} leak from the sarcoplasmic reticulum (SR) could play a role in local fluctuations in $[Ca^{2+}]_i$ (Shmygol and Wray, 2004). Our algorithm will permit further investigation of single cell $[Ca^{2+}]_i$ levels both between and during myometrial contractions.

Our results show preliminary analyses of multiple single-cell recordings, taken from selected cells and from a small number of datasets. Our method will permit further investigation of locally asynchronous $[Ca^{2+}]_i$ activity. Two recent studies in which whole brain activity in zebrafish was recorded using calcium indicator fluorescence imaging used various methods for spatial and temporal clustering of correlated activity patterns (Ahrens et al., 2013; Portugues et al., 2014). Such techniques can be used to analyse the calcium indicator fluorescence signals in motion-corrected myometrial tissue. For example, clustering tissue regions based on similarity of $[Ca^{2+}]_i$ signals would identify active contractile components and regions exhibiting fluctuations in $[Ca^{2+}]_i$ activity. Detailed analysis and comparison of spatiotemporal $[Ca^{2+}]_i$ signals from active regions of tissue within multiple datasets may reveal more about variability in initiation sites and direction of propagation of action potentials during contractions.

The recordings used in this thesis were made at a magnification suited to simultaneously capturing the $[Ca^{2+}]_i$ activity of multiple contracting myocytes from multiple myocyte bundles. It would be interesting to apply our motion-correction algorithm to images of contracting myometrium captured at a higher magnification; this may reveal spatiotemporal patterns of $[Ca^{2+}]_i$ activity within individual myocytes. A complete picture of uterine contractility requires an understanding of $[Ca^{2+}]_i$ dynamics at intra- and intercellular as well as at tissue and organ level. Both intra- and intercellular calcium waves have been seen in calcium images of cultured human myometrial myocytes (Young and Hession, 1996; Young and Zhang, 2001). Models of $[Ca^{2+}]_i$ activity within individual atrial myocytes have revealed spatiotemporal patterns of subcellular $[Ca^{2+}]_i$ activity that contribute to an understanding of mechanisms of cardiac dysfunction (Thul et al., 2012; Thul et al., 2012). Imaging and modelling of subcellular $[Ca^{2+}]_i$ activity in uterine myocytes could likewise further our understanding of uterine contractility.

6.2 The role of oxytocin

Oxytocin plays a central role in parturition and the activation and the inhibition of its receptor are targets in the management of preterm and dysfunctional labours

(Blanks and Thornton, 2003; Wedisinghe et al., 2008). The mechanisms mediating the effect of this hormone on uterine contractility are complex and varied, and have yet to be fully elucidated (Shmygol et al., 2006; Fomin et al., 2006). In agreement with other studies (Nakao et al., 1997; Shmygol et al., 2006), we showed that application of oxytocin to strips of human myometrium produced an increase in the amplitude and duration of $[Ca^{2+}]_i$ transients associated with contractions. The canonical pathway by which oxytocin is known to stimulate contractions is via IP activation of the $G\alpha_{q/11}$ protein. $G\alpha_{q/11}$ couples to phospholipase C-β (PLC-β), which catalyses the hydrolysis of phosphatidylinositol-bis-phosphate (PIP_2) into inositol-tris-phosphate (IP_3) and diacyglycerol (DAG). IP_3 triggers the release of Ca^{2+} from the sarcoplasmic reticulum (SR), resulting in an increase in $[Ca^{2+}]_i$ and activation of the contractile mechanisms.

However, Ca^{2+} entry from the extracellular space is also thought to play a role oxytocin-induced augmentation of myometrial contractions, as a reduction in the magnitude of oxytocin-induced contractions is seen in the absence of external Ca^{2+} reported in Luckas et al. (1999). The mechanism(s) by which Ca^{2+} enters the cell remain incompletely understood; indirect activation of L-type Ca^{2+} channels by depolarisation of the cell by Ca^{2+}-activated channels and capacitative Ca^{2+} are among the suggested contributory mechanisms (Shmygol et al., 2006; Arrowsmith and Wray, 2014). Oxytocin-induced oscillations in $[Ca^{2+}]_i$ have previously be seen in cultured myometrial cells and it was thought that these oscillations may contribute to the oxytocin-induced protraction of $[Ca^{2+}]_i$-mediated action potentials and contraction (Young and Hession, 1996; Fu et al., 2000; Young et al., 2001). In this study detailed analyses of single-cell $[Ca^{2+}]_i$ signals in control and oxytocin-treated myometrial slices provided evidence that protracted action potentials were independent of oxytocin-induced oscillations. Our data suggest that oxytocin-induced $[Ca^{2+}]_i$ oscillations are not relevant to the acute regulation of myometrial contractility but may play a role in longer-term regulatory processes, for example, by triggering gene expression.

Oxytocin is also thought to mediate myometrial contractions in a calcium-independent manner, via Rho kinase (ROCK) and protein kinase C (PKC) mediated inhibition of myosin light chain phosphatase (MLCP). Inhibition of MLCP prolongs the phosphorylation of myosin light chain (MLC), and results in enhanced tension in a Ca^{2+}-independent manner. Our results showed that the rate reduction in tissue relaxation exceeds any rate reduction in the decrease of $[Ca^{2+}]_i$ in myometrial strips treated with oxytocin, supporting Ca^{2+}-sensitisation as contributory mechanism to the augmentation of myometrial contractions. We also demonstrated that the kine-

matic information obtained as a byproduct of our motion-correction algorithm can be used to compare the motion of tissue in control and oxytocin-treated slices. More detailed analysis using more datasets could reveal the influence of oxytocin on the kinematic properties, for example the velocity of contraction.

6.3 Kinematics of contraction

The sparsity of experimentally recorded mechanical properties such as active stress-strain relationships in contracting myometrium is a limiting factor in the development of plausible biophysical models of uterine contraction (Miftahof and Nam, 2011). Our motion-correction algorithm produces a complete 2-D kinematic description of muscle contraction and relaxation in slices of myometrium for the first time. We illustrate how this information can be used to compare spatiotemporal profiles of $[Ca^{2+}]_i$ signals and tissue contraction. In this work we examine selected regions of tissue for this analysis; a more complete examination, for example clustering tissue regions based on similarity of $[Ca^{2+}]_i$ signals may reveal signatures of different constituent parts of the tissue - in either $[Ca^{2+}]_i$ or contraction activity, or both. It may then be possible to compare relative elastic properties of different parts of the tissue; such information would contribute to filling the gaps in experimentally recorded mechanical properties of contracting myometrium.

6.4 Limitations and further applications

Our method for processing calcium indicator fluorescence images of contracting myometrial tissue significantly increases the amount of information that can be extracted. There are, however, limitations associated with extracting local information about $[Ca^{2+}]_i$ activity from calcium indicator fluorescence images, both processed and unprocessed; we address three of these limitations below. Firstly, the 2-D images contain information taken from a 3-D structure, and therefore signals extracted from surface myocytes may be contaminated with $[Ca^{2+}]_i$ activity from other cells within the third dimension of the tissue. This issue can be addressed by ensuring that any conclusions from calcium indicator fluorescence imaging data about $[Ca^{2+}]_i$ activity are drawn only after measurements have been taken from multiple cells and multiple datasets. In allowing multiple simultaneous local measurements to be taken, our motion-reduction algorithm assists with this. Secondly, the datasets used in this study were images of myometrial tissue loaded with the calcium indicator Fluo-4. Local intensity signals measured in calcium indicator fluorescence im-

ages of contracting tissue will be affected by changes in the thickness of the tissue associated with contractions and relaxations. This contributes to the challenge of interpreting changes in intensity in such datasets. Use of a ratiometric fluorescence probe, such as Fura-2, would minimise the effect of changeable tissue thickness. However, it is difficult, if not impossible, to use Fura-2 in ratiometric mode on the confocal microscope as a result of restrictions on the available laser lines for dye excitation.

Our algorithm could equally well be used to process wide-field microscopy datasets; this may be a promising direction for the future of calcium indicator fluorescence imaging of contracting myometrial tissue. A drawback of wide-field microscopy, however, that would require attention is that image contrast is compromised by areas out of focus much more than in confocal microscopy. Finally, our algorithm allows calcium indicator fluorescence measurements to be taken from the same cell or subcellular compartment irrespective of its shift during contraction, but such measurements necessarily reflect a spatially averaged signal. Interpreting these signals can be complicated if the region contains a non-uniform distribution of Ca^{2+} ions, an issue that should be considered when inferring $[Ca^{2+}]_i$ activity from calcium indicator fluorescence intensity (Hyrc et al., 2007).

Keeping these limitations in mind, calcium indicator fluorescence imaging remains a vital tool for developments in the understanding of uterine contractility. We hope that our method for motion-correction will contribute to the significant developments in our knowledge of this field yielding increasingly successful interventions for dysfunctional and preterm labour.

Appendix A

Motion-correction code

The complete code for correcting motion artifacts in calcium images of contracting myometrial tissue was published under the GNU General Public license. The algorithm can therefore be freely used and modified, and has potential applicability for other biological tissue samples, for example, smooth muscle and neural tissue.

```
%%%%%%%%%%%%%%%%%%%%%%%%%%%%%%%%%%%%%%%%%%%%%%%%%%%%%%%%%%%%%%%%%%%%%%%%%%%%%%%%
%
% This file contains 1 main function LSRMOTIONCORRECTION that processes
% calcium imaging data of contracting myometrium for motion-correction and
% calls 23 functions.
% Runs in MATLAB environment.
%
% Called functions grouped by objective:
%
% i) CONVERT IMAGE DATA
% 1) IDENTIFICATION OF LANDMARKS
% 2) TRACKING MOTION OF LANDMARKS BETWEEN FRAMES
% 3) REMOVAL OF OUTLIERS
% 4) COMPUTATION OF TISSUE-WIDE MOTION
% 5) MOTION-CORRECTED IMAGES
%
%%%%%%%%%%%%%%%%%%%%%%%%%%%%%%%%%%%%%%%%%%%%%%%%%%%%%%%%%%%%%%%%%%%%%%%%%%%%%%%%
% COPYRIGHT: Fiona Loftus, Magnus Richardson (2014)
% This code is free software: you can redistribute it and/or modify
% it under the terms of the GNU General Public License as published by
% the Free Software Foundation, either version 3 of the License, or
% (at your option) any later version.
%
% This program is distributed in the hope that it will be useful,
% but WITHOUT ANY WARRANTY; without even the implied warranty of
```

```
% MERCHANTABILITY or FITNESS FOR A PARTICULAR PURPOSE.  See the
% GNU General Public License for more details.
%
% See <http://www.gnu.org/licenses/> for a copy of
% the GNU General Public License
%
%%%%%%%%%%%%%%%%%%%%%%%%%%%%%%%%%%%%%%%%%%%%%%%%%%%%%%%%%%%%%%%%%%%%%%%%%%%%%%%
% LSRMOTIONCORRECTION
%
% Input:     filename
%            fmt          - movie format (can be tif or any format supported
%                           by MATLAB VideoReader function)
%            PW           - pixel width (microns)
%            frames       - vector containing frame number for start of each
%                           contraction-relaxation cycle
%
% Motion-corrected movie saved as sequence of tif files in MCMovie folder
% Pixel displacements saved as 'DP_CXBYFZ.mat' in TissueMotion folder
% X contraction number, Y batch number, Z frame number
%
% Example dataset, call:
%
% LSRMotionCorrection('Supp2Movie2.avi','avi',4.5,[1 880])
%
%%%%%%%%%%%%%%%%%%%%%%%%%%%%%%%%%%%%%%%%%%%%%%%%%%%%%%%%%%%%%%%%%%%%%%%%%%%%%%%
%==========================================================================
function LSRMotionCorrection(filename,fmt,PW,frames)
%LSRMOTIONCORRECTION Motion-correction algorithm using Gaussian fitting
%   LSRMOTIONCORRECTION(FILENAME,FMT,PW,FRAMES,OPTIONS)
%   Process movie file FILENAME with extension FMT, pixel width in microns
%   PW. FRAMES vector of frame numbers.

% directories for motion-corrected movie and tissue motion array
movieDir = 'MCMovie';
motionDir = 'TissueMotion';
mkdir(movieDir)
mkdir(motionDir)

options=struct('r',3,'lambdaC',50,'filtParamSmall',5,'filtParamLarge',9,...
    'r_th',3,'nFrames',10,'xi_th',0.05,'batchSize',400);

% r - radius of window for Gaussian fitting (pixels) (Methods)
% lambdaC - characteristic length scale (microns) (Methods)
% filtParamLarge, filtParamSmall - parameters for bandpass filter (Methods)
% r_th - local median test outlier detection threshold (Sup Methods)
% nFrames - number frames used for average distance outlier detection (Sup
```

```
% Methods)
% xi_th - threshold for configuration change outlier detection (Sup
% Methods)
% batchSize - tissue displacement arrays saved in batches, up to batchSize
% frames in each array

% get information structure about movie file (needed for converting movie
% frames into matrices)
[movieStruct,nR,nC] = getMovieStructure(filename,fmt);

batchNum = 0;

if matlabpool('size')==0
    matlabpool open
end

% 1st for loop runs motion-correction algorithm over each
% contraction-relaxation cycle
for c = 1:length(frames)-1
    fC1 = frames(c);        % first frame in cycle
    fCEnd = frames(c+1);    % last frame in cycle

    % 1) identify landmarks for tracking in first frame
    % get first image frame as matrix
    imgfC1 = imageAsMatrix(filename,fmt,fC1,movieStruct);
    % coordinates of landmarks in first frame x1,y1
    [x1,y1] = landmarks(imgfC1,options.r,options.filtParamSmall,...
        options.filtParamLarge,nR,nC);

    % 2) track landmarks between f1 and fEnd
    % coordinates of landmarks in all frames xn, yn
    [xn,yn] = landmarkTracking(fC1,fCEnd,options.r,x1,y1,movieStruct,...
        filename,fmt);

    % 3) remove outliers
    [xn,yn] = removeOutliers(xn,yn,options.lambdaC,PW,options.nFrames,...
    options.xi_th,options.r_th);

    % 4) computation of tissue-wide motion
    fCs = frames(c+1)-frames(c)+1;          % number of frames in cycle
    bCs = ceil(fCs/(options.batchSize));    % number of batches in cycle

    % 2nd for loop computes tissue wide motion for each cycle in batches
    % (so as not to exceed max variable size)
    for b = 1:bCs
        batchNum = batchNum+1;
```

```
        % 1st and last 'time' index of tracked landmarks for current batch
        b1 = (b-1)*options.batchSize+1;
        bEnd = min(b1+options.batchSize-1,fCs);

        [Dp] = tissueWideMotion(xn(:,b1:bEnd),...
            yn(:,b1:bEnd),options.lambdaC,PW,nR,nC);

        % for batches>1 obtain motion relative to first frame
        if (b+c >2)
            Dp = motionFromFirstFrame(Dp,DpEnd,nR,nC);
        end

        % first frame in current batch
        fB1 = fC1 + b1 - 1;

        % remove overlap between batches
        if b == 1 && c ~= 1
            Dp = Dp(:,:,2:end);
            fB1 = fB1+1;
        end

        % save tissue motion array
        oldfolder = cd(motionDir);
        FileNameDisps = strcat('Dp_','C',int2str(c),'B',...
            int2str(batchNum),'F',int2str(fB1),'.mat');
        save(FileNameDisps,'Dp','-v7.3');
        cd(oldfolder);

        % 5) motion-corrected images
        mkNewImages(movieStruct,filename,fmt,fB1,Dp,nC,nR,movieDir)

        % store final displacements in batch
        DpEnd = Dp(:,:,end);
    end
end
matlabpool close
exit;
end
%--------------------------------------------------------------------------
%%%%%%%%%%%%%%%%%%%%%%%%%%%%%%%%%%%%%%%%%%%%%%%%%%%%%%%%%%%%%%%%%%%%%%%%%%%%
% i) CONVERT IMAGE DATA
%%%%%%%%%%%%%%%%%%%%%%%%%%%%%%%%%%%%%%%%%%%%%%%%%%%%%%%%%%%%%%%%%%%%%%%%%%%%
%==========================================================================
function [movieStruct,nR,nC] = getMovieStructure(filename,fmt)
% GETMOVIESTRUCTURE Gets info about movie file
%    [MOVIESTRUCT,NR,NC] = GETMOVIESTRUCTURE(FILENAME,FMT)
```

```
%   Get height NR, width NC and additional information about movie file
%   FILENAME, with any extension FMT, to be returned as a structure
%   MOVIESTRUCT

% convert file into object
if strcmp(fmt,'tif')
    movieStruct = imfinfo(filename);
    nR = movieStruct(1).Height;
    nC = movieStruct(1).Width;
else
    movieStruct = VideoReader(filename);
    nR = movieStruct.Height;
    nC = movieStruct.Width;
end
end
%=========================================================================
function img = imageAsMatrix(filename,fmt,frame,movieStruct)
% IMAGEASMATRIX Converts frame of movie into matrix
%   IMG = IMAGEASMATRIX(FILENAME,FMT,FRAME,MOVIESTRUCT)
%   Converts frame number FRAME of movie file FILENAME with extension FMT
%   and structure MOVIESTRUCT into double matrix, IMG

if strcmp(fmt,'tif')
    img = imread(filename, frame, 'Info', movieStruct);
    img = double(img);
else
    img = read(movieStruct,frame);
    img = img(:,:,1);
    img = double(img);
end
end
%-------------------------------------------------------------------------
%%%%%%%%%%%%%%%%%%%%%%%%%%%%%%%%%%%%%%%%%%%%%%%%%%%%%%%%%%%%%%%%%%%%%%%%
% 1) IDENTIFICATION OF LANDMARKS
%%%%%%%%%%%%%%%%%%%%%%%%%%%%%%%%%%%%%%%%%%%%%%%%%%%%%%%%%%%%%%%%%%%%%%%%
%=========================================================================
function [x1,y1] = landmarks(img,r,fpS,fpL,nR,nC)
%LANDMARKS Identifies landmarks to track
%   [X1,Y1] = LANDMARKS(IMG,R,FPS,FPL,NR,NC)
%   Vectors X1, Y1 of coordinates of landmarks for tracking in image frame
%   IMG identified by comparing every (2R+1)x(2R+1) window with equal-sized
%   Gaussian filter. Bandpass filter applied to image, filters small
%   objects up to 2*FPS pixels and large objects down to 2*FPL pixels.
%   Image frame size NRxNC.

[imgFilt] = bandpass(img,nR,nC,fpS,fpL);
```

```
[x1,y1] = GaussianCorrelation(imgFilt,r);
end
%-------------------------------------------------------------------------
%=========================================================================
function[imgFilt] = bandpass(img,nR,nC,fps,fpl)
% BANDPASS Bandpass filtered image
%   IMGFILT = BANDPASS(IMG,NR,NC,FPS,FPL)
%   Bandpass filter IMG size NRxNC, filter parameters FPS, FPL

%   cf Joachim Walter's FFT Filter plugin at
%   "http://rsb.info.nih.gov/ij/plugins/fft-filter.html"

% find smallest power of 2 larger than 2 dimensions
nMax = max(nC,nR);
power2vec = 2.^(1:ceil(nMax)/2);
index = find(power2vec>=1.5*nMax,1,'first');
newSize = power2vec(index);

% get mirrored and tiled new image
newImage = mirrorTile(img,newSize,nC,nR);

% forward transform
fht = fft2(newImage);

paramLarge = 2*fpl/newSize;
paramSmall = 2*fps/newSize;

[fht,~] = bpFilt(fht,paramLarge,paramSmall);

% reverse transform
rFFT = ifft2(fht,'symmetric');

imgFilt = rFFT(newSize/2 - ceil(nR/2):newSize/2 - ceil(nR/2)+nR-1,...
    newSize/2 - ceil(nC/2):newSize/2 - ceil(nC/2)+nC-1);
end
%-------------------------------------------------------------------------
%=========================================================================
function newImage = mirrorTile(image,newSize,nC,nR)
% MIRRORTILE image with mirror tiling at edges

%   cf Joachim Walter's FFT Filter plugin at
%   "http://rsb.info.nih.gov/ij/plugins/fft-filter.html"

newImage = zeros(newSize);
newImage(newSize/2 - round(nR/2):newSize/2 - round(nR/2)+nR-1,...
```

```
    newSize/2 - round(nC/2):newSize/2 - round(nC/2)+nC-1) = image;

for y = 1:newSize
    for x = 1:newSize
        if y < newSize/2-round(nR/2) && x < newSize/2-round(nC/2)
            newImage(y,x) = newImage((newSize/2 - round(nR/2)) +...
            (newSize/2 - round(nR/2))-y,(newSize/2 - round(nC/2)) + ...
            (newSize/2 - round(nC/2))-x);
        elseif y < newSize/2-round(nR/2) && x >= newSize/2-round(nC/2)
            newImage(y,x) = newImage(newSize/2 - round(nR/2) + ...
            newSize/2 - round(nR/2)-y,x);
        elseif x < newSize/2-round(nC/2) && y >= newSize/2-round(nR/2)
            newImage(y,x) = newImage(y,newSize/2 - round(nC/2) + ...
            newSize/2 - round(nC/2)-x);
        end
        if y >= newSize/2 + round(nR/2) && x >= newSize/2 + round(nC/2)
            newImage(y,x) = newImage(newSize/2 + round(nR/2)-1 + ...
            newSize/2 + round(nR/2)-y,newSize/2 + round(nC/2)-1 + ...
            newSize/2 + round(nC/2)-x);
        elseif y >= newSize/2 + round(nR/2) && x < newSize/2 + round(nC/2)
            newImage(y,x) = newImage(newSize/2 + round(nR/2) -1 + ...
            newSize/2 + round(nR/2)-y,x);
        elseif x >= newSize/2 + round(nC/2) && y < newSize/2 + round(nR/2)
            newImage(y,x) = newImage(y,newSize/2 + round(nC/2) -1 + ...
            newSize/2 + round(nC/2)-x);
        end
    end
end
end
%--------------------------------------------------------------------------
%==========================================================================
function [fht,BPfilt] = bpFilt(fht,paramLarge,paramSmall)
% BPFILT Bandpass filter

%   cf Joachim Walter's FFT Filter plugin at
%   "http://rsb.info.nih.gov/ij/plugins/fft-filter.html"

maxN = size(fht,1);

% create BPfilt
BPfilt = ones(maxN);

% calculate factor in exponent of Gaussian from paramLarge/paramSmall
scaleLarge = paramLarge^2;
scaleSmall = paramSmall^2;
```

```
% loop over rows
for j = 2:maxN/2
    row = j;
    backrow = (maxN-j)+2;
    rowFactLarge = exp(-((j-1)^2)*scaleLarge);
    rowFactSmall = exp(-((j-1)^2)*scaleSmall);

    % loop over columns
    for col = 2:maxN/2
        backcol = maxN-col+2;
        colFactLarge = exp(-((col-1)^2)*scaleLarge);
        colFactSmall = exp(-((col-1)^2)*scaleSmall);
        factor = (1-rowFactLarge*colFactLarge)*rowFactSmall*colFactSmall;

        fht(row,col) = fht(row,col)*factor;
        fht(backrow,col) = fht(backrow,col)*factor;
        fht(row,backcol) = fht(row,backcol)*factor;
        fht(backrow,backcol) = fht(backrow,backcol)*factor;
        BPfilt(row,col) = BPfilt(row,col)*factor;
        BPfilt(backrow,col) = BPfilt(backrow,col)*factor;
        BPfilt(row,backcol) = BPfilt(row,backcol)*factor;
        BPfilt(backrow,backcol) = BPfilt(backrow,backcol)*factor;
    end
end

% process meeting points
rowmid = (maxN/2)+1;
rowFactLarge = exp(-((maxN/2)^2)*scaleLarge);
rowFactSmall = exp(-((maxN/2)^2)*scaleSmall);

fht(maxN/2+1,1) = fht(maxN/2+1,1)*(1 - rowFactLarge)*rowFactSmall;
fht(1,maxN/2+1) = fht(1,maxN/2+1)*(1 - rowFactLarge) * rowFactSmall;
fht(maxN/2+1,maxN/2+1) = fht(maxN/2+1,maxN/2+1)*(1 - ...
    rowFactLarge*rowFactLarge)*rowFactSmall*rowFactSmall;
BPfilt(maxN/2+1,1) = BPfilt(maxN/2+1,1)*(1 - rowFactLarge)*rowFactSmall;
BPfilt(1,maxN/2+1) = BPfilt(1,maxN/2+1)*(1 - rowFactLarge)*rowFactSmall;
BPfilt(maxN/2+1,maxN/2+1) = BPfilt(maxN/2+1,maxN/2+1)*(1 - ...
    rowFactLarge*rowFactLarge)*rowFactSmall*rowFactSmall;

% loop along row 1 and maxN/2+1
rowFactLarge = exp(-((maxN/2+1)^2)*scaleLarge);
rowFactSmall = exp(-((maxN/2+1)^2)*scaleSmall);
for col = 2:maxN/2
    backcol = maxN-col+2;
    colFactLarge = exp(-((col-1)^2)*scaleLarge);
    colFactSmall = exp(-((col-1)^2)*scaleSmall);
```

```
    fht(col) = fht(col)*(1 - colFactLarge) * colFactSmall;
    fht(backcol) = fht(backcol)*(1 - colFactLarge) * colFactSmall;
    fht(rowmid,col) = fht(rowmid,col)*(1 - colFactLarge*rowFactLarge)...
        * colFactSmall*rowFactSmall;
    fht(rowmid,backcol) = fht(rowmid,backcol)*(1 - ...
        colFactLarge*rowFactLarge) * colFactSmall*rowFactSmall;
    BPfilt(1,col) = BPfilt(1,col)*(1 - colFactLarge) * colFactSmall;
    BPfilt(1,backcol) = BPfilt(1,backcol)*(1 - colFactLarge) * ...
        colFactSmall;
    BPfilt(rowmid,col) = BPfilt(rowmid,col)*(1 - ...
        colFactLarge*rowFactLarge) * colFactSmall*rowFactSmall;
    BPfilt(rowmid,backcol) = BPfilt(rowmid,backcol)*(1 - ...
        colFactLarge*rowFactLarge) * colFactSmall*rowFactSmall;
end

% loop along column 1 and maxN/2+1
colFactLarge = exp(-((maxN/2)^2)*scaleLarge);
colFactSmall = exp(-((maxN/2)^2)*scaleSmall);
for j = 2:maxN/2
    row = j;
    backrow = (maxN-j)+2;
    rowFactLarge = exp(-(j^2)*scaleLarge);
    rowFactSmall = exp(-(j^2)*scaleSmall);
    fht(row,1) = fht(row,1)*(1 - rowFactLarge) * rowFactSmall;
    fht(backrow,1) = fht(backrow,1)*(1 - rowFactLarge) * rowFactSmall;
    fht(row,maxN/2+1) = fht(row,maxN/2+1)*...
        (1 - rowFactLarge*colFactLarge)* rowFactSmall*colFactSmall;
    fht(backrow,maxN/2+1) = fht(backrow,maxN/2+1)*(1 - ...
        rowFactLarge*colFactLarge) * rowFactSmall*colFactSmall;
    BPfilt(row,1) = BPfilt(row,1)*(1 - rowFactLarge) * rowFactSmall;
    BPfilt(backrow,1) = BPfilt(backrow,1)*(1 - rowFactLarge) * ...
    rowFactSmall;
    BPfilt(row,maxN/2+1) = BPfilt(row,maxN/2+1)*(1 - ...
        rowFactLarge*colFactLarge) * rowFactSmall*colFactSmall;
    BPfilt(backrow,maxN/2+1) = BPfilt(backrow,maxN/2+1)*(1 - ...
        rowFactLarge*colFactLarge) * rowFactSmall*colFactSmall;
end
end
%-------------------------------------------------------------------------
%=========================================================================
function[x1,y1] = GaussianCorrelation(img,r)
% GAUSSIANCORRELATION identifies 'Gaussian-like' windows for tracking
%   [X1,Y1] = GAUSSIANCORRELATION(IMG,R)
%   Vectors X1, Y1 of coordinates of centres of non-overlapping
%   (2R+1)x(2R+1) sized windows in IMG most highly correlated with
%   (2R+1)x(2R+1) sized Gaussian filter
```

```
[nR,nC] = size(img);
NumWindows = (nR-2*r)*(nC-2*r);

corrCoeffs = getCorrCoeffs(img,r,nR,nC,NumWindows);

noOverlapIndex = nonOverlappingCorrCoeffs(corrCoeffs,r,nR,nC,NumWindows);

topCorCoIndex = topCorrelatedPixels(corrCoeffs,noOverlapIndex);

[subRow,subCol] = ind2sub([nR-2*r,nC-2*r],topCorCoIndex);
x1 = subCol+r;
y1 = subRow+r;

end
%-------------------------------------------------------------------------
%=========================================================================
function corrCoeffs = getCorrCoeffs(img,r,nR,nC,NumWindows)
% Find correlation coefficients of all (2r+1)*(2r+1) sized windows in img
% with equal sized Gaussian filter

% x and y indices of all pixels
[xIndex,yIndex] = meshgrid(1:nC,1:nR);

% 1D indices of all window centres in img (excluding boundaries)
winCentre1D = sub2ind([nR nC],yIndex(r+1:nR-r,r+1:nC-r),...
    xIndex(r+1:nR-r,r+1:nC-r));

% Gaussian filter (G)
sigma = (2*r+1)/3;
G = fspecial('gaussian',[2*r+1 2*r+1],sigma);

% correlation coefficient vector
corrCoeffs = zeros(1,NumWindows);

% find correlation coefficient for each window
for index = 1:NumWindows
    window = winCentre1D(index);
    [row,col] = ind2sub([nR,nC],window);

    LandmarkWindow = img(row-r:row+r,col-r:col+r);
    NormLW = LandmarkWindow/sum(sum(LandmarkWindow));

    corrCoeffs(index) = corr2(NormLW,G);
end
```

```
end
%-------------------------------------------------------------------------
%=========================================================================
function noOverlapIndex = nonOverlappingCorrCoeffs(corrCoeffs,r,nR,nC,...
    NumWindows)
% get indices of windows with highest correlation coefficient in each
% overlapping region

% sort windows by order of correlation coefficient
[~,sortCorrCoeffsIndex] = sort(corrCoeffs,'descend');

% centre of windows contained within a subsection of image frame, size
% (ny-2r)x(nx-2r)
subNy = nR-2*r;      % height of subsection
subNx = nC-2*r;      % width of subsection
[subRow,subCol] = ind2sub([subNy,subNx],sortCorrCoeffsIndex);

% loop through all windows to obtain a vector WINDOWARRAY with indices of
% sorted windows with highest correlation coefficients in overlapping
% regions
c = 1; % counter
num = 0; % number of pixels checked or removed
windowArray = 1:NumWindows;
while num < NumWindows
    removeWindow = [];
    for t = (c+1):length(windowArray)
        if abs(subCol(windowArray(c)) - subCol(windowArray(t)))<=r &&...
                abs(subRow(windowArray(c)) - subRow(windowArray(t)))<=r
            removeWindow = vertcat(removeWindow,windowArray(t));
        end
    end
    windowArray = setdiff(windowArray,removeWindow);    % update WINDOWARRAY
    c = c+1;                                            % update counter
    num = num+1+length(removeWindow);                   % update NUM
end
% indices of correlation coefficients to keep
noOverlapIndex = sortCorrCoeffsIndex(windowArray);
end
%-------------------------------------------------------------------------
%=========================================================================
function [topCorCoIndex] = topCorrelatedPixels(corrCoeffs,noOverlapIndex)
% get vector TOPCORCOINDEX of indices of windows with correlation
% coefficient > lower bound (LB), determined by fitting Gaussian mixture
% model with 2 components

% Gaussian mixture model, 2 components
```

```
options = statset('MaxIter',200);
obj = gmdistribution.fit(corrCoeffs(noOverlapIndex)',2,'Options',options);
% index of population with highest mean
idx = cluster(obj,corrCoeffs(noOverlapIndex)');
if min(corrCoeffs(noOverlapIndex(idx==1))) < ...
        min(corrCoeffs(noOverlapIndex(idx==2)))
    inLarge = 2;
else
    inLarge = 1;
end

topCorCoIndex = noOverlapIndex(idx == inLarge);
end
%--------------------------------------------------------------------------
%%%%%%%%%%%%%%%%%%%%%%%%%%%%%%%%%%%%%%%%%%%%%%%%%%%%%%%%%%%%%%%%%%%%%%%%%%%
% 2) TRACKING MOTION OF LANDMARKS BETWEEN FRAMES
%%%%%%%%%%%%%%%%%%%%%%%%%%%%%%%%%%%%%%%%%%%%%%%%%%%%%%%%%%%%%%%%%%%%%%%%%%%
%==========================================================================
function [xn,yn] = landmarkTracking(f1,fL,r,x0,y0,movieStruct,filename,ext)
% LANDMARKTRACKING Tracks location of landmarks
%   [XN,YN] = LANDMARKTRACKING(F1,FL,R,X0,Y0,MOVIESTRUCT,FILENAME,EXT, ...
% CONTRAST)
%   Location of all landmarks tracked in all frames between F1 and FL.
%   XN, YN Coordinates of all landmarks in all frames. Landmarks tracked by
%   following centre of 2D Gaussian fitted to (2R+1)x(2R+1) window around
%   each landmark.

% parameters for fitted Gaussian
params = zeros(length(x0),5);
% params = [A,B,x0,y0,sigma^2];

% number of frames
N = fL-f1+1;

% coordinates of landmarks
xn = zeros(length(x0),N);
yn = zeros(length(y0),N);

for n = 1:N     % index over all frames
    parfor i = 1:length(x0)     % index over all landmarks
        imgFrame = imageAsMatrix(filename,ext,n+f1-1,movieStruct);

        % unsharp fitler to enhance contrast
        imgFrame = imgFrame./255;
        h = fspecial('unsharp');
        imgFrame = imfilter(imgFrame,h);
```

```
            params(i,:) = GaussianFit(imgFrame,y0(i),x0(i),r);
        end
        % populate coordinates of landmarks
        xn(:,n) = params(:,3);
        yn(:,n) = params(:,4);

        % update coordinates for centre of landmark windows
        x0 = round(params(:,3));
        y0 = round(params(:,4));
    end
    end
    %-------------------------------------------------------------------------
    %=========================================================================
    function params = GaussianFit(imgFrame,y0,x0,r)
    % GAUSSIANFIT fits 2D Gaussian to image window
    %   PARAMS = GAUSSIANFIT(IMGFRAME,Y0,X0,R)
    %   2D Gaussian fitted to (2R+1)x(2R+1) window around pixel X0, Y0 in
    %   IMGFRAME.

    %   2D Gaussian
    %   G = A + B*exp(-((x-x0)^2 + (y-y0)^2)/(2*sigma^2))

    %   Fitted parameters
    %   PARAMS = [A,B,x0,y0,sigma^2];

    [nR,nC] = size(imgFrame);

    % if point lies on a boundary, tracks is zero
    if x0-r<1 || x0+r>nC || y0-r<1 || y0+r>nR
        params(1:5) = 0;
    % for interior points, extract (2r+1)x(2r+1) window and fit Gaussian
    else
        L = x0-r;
        R = x0+r;
        B = y0-r;
        T = y0+r;

        window = imgFrame(B:T,L:R);
        [wm,wn] = size(window);

        % Starting values of parameters to fit for least squares algorithm
        params0 = [mean2(window),max(max(window)),r+1,r+1,1];

        LB = [-inf,0,1,1,0];        % lower bounds for parameters
        UB = [inf,inf,wn,wm,r];     % upper bounds for parameters
```

```
    % finds fitted parameters of function @objfun
    options = optimset('Display','off');
    [params,~] = lsqnonlin(@(P) objfun(P,window),params0,LB,UB,options);

    % convert back to full frame indices
    params(3) = params(3)+L-1;
    params(4) = params(4)+B-1;
end
end
%--------------------------------------------------------------------------
%==========================================================================
function resids = objfun(params,I)
% vector residual RESIDS of image I and Gaussian with parameters PARAMS

y = 1:length(I(:,1));
x = 1:length(I(1,:));
G = params(1) + params(2)*exp(-((y - params(4)).^2)'/(2*params(5))) ...
                *exp(-((x - params(3)).^2)/(2*params(5)));
residM = G - I;

resids = reshape(residM,length(I(1,:))^2,1);
end
%--------------------------------------------------------------------------
%%%%%%%%%%%%%%%%%%%%%%%%%%%%%%%%%%%%%%%%%%%%%%%%%%%%%%%%%%%%%%%%%%%%%%%%%%%%
% 3) REMOVAL OF OUTLIERS
%%%%%%%%%%%%%%%%%%%%%%%%%%%%%%%%%%%%%%%%%%%%%%%%%%%%%%%%%%%%%%%%%%%%%%%%%%%%
%==========================================================================
function [xn,yn] = removeOutliers(xn,yn,lambdaC,PW,nFrames,xi_th,r_th)
% REMOVEOUTLIERS 4-stage filtering for outliers
%   TRACKS = REMOVEOUTLIERS(TRACKS,lambdaC,PW,NFRAMES,XI_TH,R_TH)

L = length(xn(:,1));      % number of landmarks

% remove tracks of landmarks that hit boundaries
[boundary,~] = find(xn==0 | yn==0);
xn = xn(setdiff(1:L,boundary),:);
yn = yn(setdiff(1:L,boundary),:);

% 1) coincident landmark tracks filter
[xn,yn] = coincidentFilter(xn,yn,nFrames);

% 2) total distance filter
[xn,yn] = distanceFilter(xn,yn);

% 3) local configuration filter
```

```
[xn,yn] = configurationFilter(xn,yn,lambdaC,PW,xi_th);

% 4) local median test
[xn,yn] = localMedianTest(xn,yn,lambdaC,PW,r_th);
end
%-------------------------------------------------------------------------
%=========================================================================
function [xn,yn] = coincidentFilter(xn,yn,nFrames)
% COINCIDENTFILTER only keep one landmark where tracks intersect
%   [XN,YN] = COINCIDENTFILTER(XN,YN,NFRAMES)
%   Finds landmarks whose tracks intersect and keeps only the one whose
%   speed is most similar in NFRAMES before and after intersection

L = length(xn(:,1));      % number of landmarks
N = length(xn(1,:));      % number of frames

% binary matrix where 1s will identify tracks that intersect
coicidenceMatrix = zeros(L,L);

% interframe displacement in each dimension
xIntDisp = xn(:,2:end) - xn(:,1:end-1);
yIntDisp = yn(:,2:end) - yn(:,1:end-1);

% interframe displacement magnitude
intDispMag = (xIntDisp.^2 + yIntDisp.^2).^(1/2);

% location of landmarks in final frame
xEnd = xn(:,end);
yEnd = yn(:,end);

% populate coicidenceMatrix with ones where intersection
for i = 1:L
    coicidenceMatrix(i,xEnd==xEnd(i) & yEnd==yEnd(i)) = 1;
end

% index of intersecting landmarks
coincidenceIndex = find(sum(coicidenceMatrix,2)>1);

% temporary vector with indices of intersecting landmarks
coincidenceIndexTemp = coincidenceIndex;

% binary vector for all intersecting landmarks, will be populated with ones
% for landmarks to keep
coincidentsToKeep = zeros(1,length(coincidenceIndex));

% compare speed before and after intersection for all coincident landmarks.
```

```
% 1st while loop to go through all intersecting landmarks
% 2nd while loop for when more than 2 landmarks intersect
count = 0;  % number of coincident landmarks tested for speed comparison
while count<length(coincidenceIndex)
    cI = coincidenceIndexTemp(1);
    allCoincidents = find(squeeze(coicidenceMatrix(cI,:))==1);

    cI1 = 1;        % index of 1st intersecting landmark
    cI2 = cI1+1;    % index of comparison intersecting landmark
    while cI2<=length(allCoincidents)
        % find frame where cI1 and cI2 meet
        meetFrame = find(xn(allCoincidents(cI1),:)==...
        xn(allCoincidents(cI2),:) & yn(allCoincidents(cI1),:)...
        ==yn(allCoincidents(cI2),:),1,'first');
        % get mean speed before and after meeting
        cI1SpeedBefore = mean(intDispMag(allCoincidents(cI1),...
            max(1,meetFrame-nFrames):meetFrame-1));
        cI2SpeedBefore = mean(intDispMag(allCoincidents(cI2),...
            max(1,meetFrame-nFrames):meetFrame-1));
        speedAfter = mean(intDispMag(allCoincidents(cI1),...
            meetFrame:min(N-1,meetFrame+nFrames)));

        % if 1st landmark speed most similar, keep as cI1 and compare with
        % next coincident landmark
        % if comparison landmark speed most similar, this becomes cI1
        [~,i] = min([abs(cI1SpeedBefore-speedAfter),abs(cI2SpeedBefore-...
            speedAfter)]);
        if i == 2
            cI1 = cI2;
        end
        cI2 = cI2+1;
    end
    % populate binary vector for intersecting landmarks to keep
    coincidentsToKeep(allCoincidents(cI1)) = 1;
    % update temporary vector
    coincidenceIndexTemp = setdiff(coincidenceIndexTemp,allCoincidents);
    % update count
    count = count+length(allCoincidents);
end

% indices of coincident landmarks to keep
coincidentsToKeepIndex = find(coincidentsToKeep==1);

% update tracks, removing all but one of each set of coincident landmarks
xn = xn([setdiff(1:L,coincidenceIndex),coincidentsToKeepIndex],:);
yn = yn([setdiff(1:L,coincidenceIndex),coincidentsToKeepIndex],:);
```

```
end
%-------------------------------------------------------------------------
%=========================================================================
function [xn,yn] = distanceFilter(xn,yn)
% DISTANCEFILTER filters outlier tracks based on average inter-frame
% distance
%   [XN,YN] = DISTANCEFILTER(XN,YN)

% interframe displacements in each dimension
xIntDisp = xn(:,2:end) - xn(:,1:end-1);
yIntDisp = yn(:,2:end) - yn(:,1:end-1);

% interframe displacements magnitude
intDispMag = (xIntDisp.^2 + yIntDisp.^2).^(1/2);

% average inter-frame displacements magnitude
intFrameDist = mean(intDispMag,2);

% upper bound for total distance
distUpperBound = mean(intFrameDist)+std(intFrameDist);

xn = xn(intFrameDist<=distUpperBound,:);
yn = yn(intFrameDist<=distUpperBound,:);
end
%-------------------------------------------------------------------------
%=========================================================================
function [xn,yn] = configurationFilter(xn,yn,lambdaC,PW,xi_th)
% CONFIGURATIONFILTER filters landmark tracks based on local configuration
%   change
%   [XN,YN] = CONFIGURATIONFILTER(XN,YN,lambdaC,PW,XI_TH)
%   For each landmark, local configuration change factor XI computed using
%   N landmarks within 2*lambdaC/PW neighbourhood. Landmarks filtered if
%   XI>XI_TH or N<4

L = length(xn(:,1));      % number of landmarks

% position coordinates in first frame
x1 = xn(:,1);
y1 = yn(:,1);
% position coordinates in last frame
xe = xn(:,end);
ye = yn(:,end);

xi = zeros(1,L);     % local configuration change factor vector
m = zeros(1,L);      % number of neighbours vector
```

```
% loop through landmarks
for f = 1:L
    % find neighbouring tracks
    [M,~] = find(abs(x1-x1(f))<=2*lambdaC/PW &...
        abs(y1-y1(f))<=2*lambdaC/PW);

    m(f) = length(M);

    % matrices of x and y coordinates (first frame)
    xCff = repmat(x1(M),1,length(M));
    yCff = repmat(y1(M),1,length(M));

    % matrices of x and y coordinates (final frame)
    xCef = repmat(xe(M),1,length(M));
    yCef = repmat(ye(M),1,length(M));

    % get distance matrix (first frame)
    C1 = ((xCff - xCff').^2 + (yCff - yCff').^2).^(1/2);

    % get distance matrix (final frame)
    CF = ((xCef - xCef').^2 + (yCef - yCef').^2).^(1/2);

    % get magnitude of difference between first frame and last frame
    C_diff = abs(C1 - CF);

    % replace zeros with nans
    C_diff(C_diff==0) = nan;

    % find average difference for landmark
    meanDiffFeat = nanmean(C_diff(M==f,M~=f));

    % find average difference for all nhbs (excluding landmark)
    meanDiffNhbs = nanmean(C_diff(M~=f,M~=f),2);

    % find average difference over all nhbs
    meanTot = mean(meanDiffNhbs);

    delta = meanDiffFeat/(meanTot);

    xi(f) = (delta-1)*m(f)/L;
end
xn = xn(xi<=xi_th & m>=4,:);
yn = yn(xi<=xi_th & m>=4,:);
end
%-------------------------------------------------------------------------
%=========================================================================
```

```
function [xn,yn] = localMedianTest(xn,yn,lambdaC,PW,r_th)
% LOCALMEDIANTEST Low temporal resolution outlier detection
%   [XN,YN] = LOCALMEDIANTEST(XN,YN,lambdaC,PW,R_TH)
%   Landmark removed if residual R_AST>R_TH. R_AST difference between
%   displacement vector and median displacement vector of all neighbouring
%   landmarks. Neighbourhood within 2*lambdaC/PW radius.

% cf Westerweel 1994

L = length(xn(:,1));        % number landmarks

% position coordinates in first frame
x1 = xn(:,1);
y1 = yn(:,1);

% x and y displacements between 1st and last frame
xDisp = xn(:,end) - xn(:,1);
yDisp = yn(:,end) - yn(:,1);

r_ast = zeros(1,L);

for f = 1:L
    % find neighbouring landmarks
    [nhbt,~] = find(abs(x1-x1(f))<=2*lambdaC/PW & abs(y1-y1(f))<=2*...
        lambdaC/PW);

    % find median vector excluding f (x and y components)
    medDispX = median(xDisp(nhbt~=f));
    medDispY = median(yDisp(nhbt~=f));
    % r_ast for neighbours
    r_astNhbt = ((xDisp(nhbt~=f)-medDispX).^2 + ...
        (yDisp(nhbt~=f)-medDispY).^2).^(1/2);

    r_ast(f) = ((xDisp(f)-medDispX).^2 + (yDisp(f)-medDispY).^2).^(1/2);
    % normalise r_ast
    r_ast(f) = r_ast(f)/(median(r_astNhbt)+0.1);
end

xn = xn(r_ast<r_th,:);
yn = yn(r_ast<r_th,:);
end
%--------------------------------------------------------------------------
%%%%%%%%%%%%%%%%%%%%%%%%%%%%%%%%%%%%%%%%%%%%%%%%%%%%%%%%%%%%%%%%%%%%%%%%%%%%
% 4) COMPUTATION OF TISSUE-WIDE MOTION
%%%%%%%%%%%%%%%%%%%%%%%%%%%%%%%%%%%%%%%%%%%%%%%%%%%%%%%%%%%%%%%%%%%%%%%%%%%%
%=========================================================================
```

```
function [Dp] = tissueWideMotion(xn,yn,lambdaC,PW,nR,nC)
% TISSUEWIDEMOTION Displacement of all pixels
%   DP = TISSUEWIDEMOTION(XN,YN,lambdaC,PW,M,N)
%   Displacement of all pixels DP found as weighted average of tracked
%   landmark coordinates XN, YN.

lambddaC = lambdaC/PW;     % lambdaC in pixels

L = length(xn(:,1));       % number of landmarks
N = length(xn(1,:));       % number of frames

% smooth tracks
[xn,yn] = smoothTracks(xn,yn);

% 2D array of first frame coordinates
x1 = repmat(xn(:,1),1,N);
y1 = repmat(yn(:,1),1,N);

% x and y landmark displacements
DlX = xn - x1;
DlY = yn - y1;

% distance between each pixel and each landmark (Phi)
distmat = zeros(nR,nC,L);
Phi_3D = zeros(nR,nC,L);
for ll = 1:L
    distmat(round(yn(ll,1)),round(xn(ll,1)),ll) = 1;
    Phi_3D(:,:,ll) = bwdist(distmat(:,:,ll));
end

% make distance array 2D
Phi = reshape(Phi_3D,nR*nC,L);
W = distFunc(Phi,lambddaC);

sumW = repmat(sum(W,2),1,N);

DpX = W*DlX./sumW;
DpY = W*DlY./sumW;

Dp = permute(cat(3,DpX,DpY),[3,1,2]);
end
%-------------------------------------------------------------------------
%=========================================================================
function [x,y] = smoothTracks(x,y)
% SMOOTHTRACKS smooths tracked landmark trajectories
% [x,y] = smoothTracks(x,y)
```

```
for xc = 1:length(x(:,1))
    x(xc,:) = smooth(x(xc,:),'lowess');
    y(xc,:) = smooth(y(xc,:),'lowess');
end
end
%-------------------------------------------------------------------------
%=========================================================================
function W = distFunc(phi,lambddaC)
% DISTFUNC exponential decay distance function
% W = distFunc(distance,lambddaC)
W = exp(-phi/lambddaC);
end
%-------------------------------------------------------------------------
%=========================================================================
function DpFFF = motionFromFirstFrame(Dp,DpEnd,nR,nC)
% MOTIONFROMFIRSTFRAME Pixel displacement relative to first frame
%   DPFFF = MOTIONFROMFIRSTFRAME(DP,DPEND,NR,NC)
%   Pixel displacements from first frame DPFFF computed using
%   current batch of DP and end coordinates of previous batch
%   DPEND. Bilinear interpolation to find motion of sub-pixel
%   coordinates.

% get coordinates of starting points for PIXELDISPSFFF
[x,y] = meshgrid(1:nC,1:nR);
xStart = reshape(x,nC*nR,1)+DpEnd(1,:)';
yStart = reshape(y,nC*nR,1)+DpEnd(2,:)';

% find range of starting coordinates
minx = min(xStart);
miny = min(yStart);
img1x = 1;
img1y = 1;

% rescale to >1
if minx<1
    xStart = xStart+abs(floor(minx))+1;
    img1x = img1x+abs(floor(minx))+1;
end
if miny<1
    yStart = yStart+abs(floor(miny))+1;
    img1y = img1y+abs(floor(miny))+1;
end

% find neighbouring integers for bilinear interpolation
xL = floor(xStart);
```

```
xR = xL+1;
yB = floor(yStart);
yT = yB+1;

% find max of integers for interpolation
maxx = max([max(xR),img1x+nC-1]);
maxy = max([max(yT),img1y+nR-1]);

% get indices for neighbouring pixels
XLYBIndex = reshape(sub2ind([maxy maxx],yB,xL),nC*nR,1);
XLYTIndex = reshape(sub2ind([maxy maxx],yT,xL),nC*nR,1);
XRYBIndex = reshape(sub2ind([maxy maxx],yB,xR),nC*nR,1);
XRYTIndex = reshape(sub2ind([maxy maxx],yT,xR),nC*nR,1);

% get weightings for bilinear interpolation
wxLyB = (xR-xStart).*(yT-yStart);
wxLyT = (xR-xStart).*(yStart-yB);
wxRyB = (xStart-xL).*(yT-yStart);
wxRyT = (xStart-xL).*(yStart-yB);

nF = length(Dp(1,1,:));

DpFFF = zeros(2,nR*nC,nF);

for f = 1:nF
    % make 2D matrix with borders for x and y
    dispBorder1 = zeros(maxy,maxx);
    dispBorder2 = zeros(maxy,maxx);
    dispBorder1(img1y:img1y+nR-1,img1x:img1x+nC-1) = ...
        reshape(squeeze(Dp(1,:,f)),nR,nC);
    dispBorder2(img1y:img1y+nR-1,img1x:img1x+nC-1) = ...
        reshape(squeeze(Dp(2,:,f)),nR,nC);

    if img1y>1
        % added borders equal previous borders
        dispBorder1(1:img1y-1,:) = repmat(dispBorder1(img1y,:),...
            (img1y-1),1);
        dispBorder2(1:img1y-1,:) = repmat(dispBorder2(img1y,:),...
            (img1y-1),1);
    end
    if maxy>img1y+nR-1
        % added borders equal previous borders
        dispBorder1(img1y+nR:end,:) = repmat(dispBorder1(img1y+nR-1,:),...
            (maxy-(img1y+nR-1)),1);
        dispBorder2(img1y+nR:end,:) = repmat(dispBorder2(img1y+nR-1,:),...
            (maxy-(img1y+nR-1)),1);
```

```
    end
    if img1x>1
        % added borders equal previous borders
        dispBorder1(:,1:img1x-1) = repmat(dispBorder1(:,img1x),1,...
            (img1x-1));
        dispBorder2(:,1:img1x-1) = repmat(dispBorder2(:,img1x),1,...
            (img1x-1));
    end
    if maxx>img1x+nC-1
        % added borders equal previous borders
        dispBorder1(:,img1x+nC:end) = repmat(dispBorder1(:,img1x+nC-1),...
            1,(maxx-(img1x+nC-1)));
        dispBorder2(:,img1x+nC:end) = repmat(dispBorder2(:,img1x+nC-1),...
            1,(maxx-(img1x+nC-1)));
    end
    % corners
    dispBorder1(1:img1y,1:img1x) = dispBorder1(img1y,img1x);
    dispBorder2(1:img1y,1:img1x) = dispBorder2(img1y,img1x);
    dispBorder1(1:img1y,img1x+nC-1:end) = dispBorder1(img1y,img1x+nC-1);
    dispBorder2(1:img1y,img1x+nC-1:end) = dispBorder2(img1y,img1x+nC-1);
    dispBorder1(img1y+nR-1:end,img1x+nC-1:end) = ...
        dispBorder1(img1y+nR-1,img1x+nC-1);
    dispBorder2(img1y+nR-1:end,img1x+nC-1:end) = ...
        dispBorder2(img1y+nR-1,img1x+nC-1);
    dispBorder1(img1y+nR-1:end,1:img1x) = dispBorder1(img1y+nR-1,img1x);
    dispBorder2(img1y+nR-1:end,1:img1x) = dispBorder2(img1y+nR-1,img1x);

    dispBorder11D = reshape(dispBorder1,maxx*maxy,1);
    dispBorder21D = reshape(dispBorder2,maxx*maxy,1);

    DpFFF(1,:,f) = DpEnd(1,:)' + wxLyB.*dispBorder11D(XLYBIndex) + ...
        wxLyT.*dispBorder11D(XLYTIndex)+wxRyB.*dispBorder11D(XRYBIndex)+...
        wxRyT.*dispBorder11D(XRYTIndex);
    DpFFF(2,:,f) = DpEnd(2,:)' + wxLyB.*dispBorder21D(XLYBIndex) + ...
        wxLyT.*dispBorder21D(XLYTIndex)+wxRyB.*dispBorder21D(XRYBIndex)+...
        wxRyT.*dispBorder21D(XRYTIndex);
end
end
%--------------------------------------------------------------------------
%%%%%%%%%%%%%%%%%%%%%%%%%%%%%%%%%%%%%%%%%%%%%%%%%%%%%%%%%%%%%%%%%%%%%%%%%
% 5) MOTION-CORRECTED IMAGES
%%%%%%%%%%%%%%%%%%%%%%%%%%%%%%%%%%%%%%%%%%%%%%%%%%%%%%%%%%%%%%%%%%%%%%%%%
%==========================================================================
function mkNewImages(movieStruct,filename,ext,startf,Dp,nC,nR,folderName)
% MKNEWIMAGES creates tif file for each amended image frame
%    MKNEWIMAGES(MOVIESTRUCT,FILENAME,EXT,STARTF,DP,NC,NR,FOLDERNAME)
```

```
%   New images for all frames in current batch saved in FOLDERNAME

F = length(Dp(1,1,:));    % number of frames

for c = 1:F
    imgNew = AmendedImage(movieStruct,ext,filename,Dp,startf,c,nC,nR);

    imgNew = uint8(imgNew);

    tifName = strcat('frame',num2str(startf+c-1),'.tif');

    oldfolder = cd(folderName);

    imwrite(imgNew,tifName)

    cd(oldfolder)
end
end
%--------------------------------------------------------------------------
%==========================================================================
function imgNew = AmendedImage(movieStruct,ext,filename,Dp,startf,c,nC,nR)
% AMENDEDIMAGE images frames with reduced movement
%   IMGNEW = AMENDEDIMAGE(MOVIESTRUCT,EXT,FILENAME,DP,STARTF,C,NC,NR)
%   New image frame IMGNEW constructed from PIXELDISPS. Bilinear
%   interpolation to assign intensity value to sub-pixel coordinates

% frame number
f = startf+c-1;

img = imageAsMatrix(filename,ext,f,movieStruct);

% find new coordinates of each pixel
[Xpos,Ypos] = meshgrid(1:nC,1:nR);
XposNew = reshape(Xpos,nC*nR,1) + squeeze(Dp(1,:,c))';
YposNew = reshape(Ypos,nC*nR,1) + squeeze(Dp(2,:,c))';

% find range of starting coordinates
minx = min(XposNew);
miny = min(YposNew);
img1x = 1;
img1y = 1;

% rescale to >1
if minx<1
    XposNew = XposNew+abs(floor(minx))+1;
    img1x = img1x+abs(floor(minx))+1;
```

```
end
if miny<1
    YposNew = YposNew+abs(floor(miny))+1;
    img1y = img1y+abs(floor(miny))+1;
end

% find neighbouring indices for bilinear interpolation
Xpos0 = floor(XposNew);
Xpos1 = Xpos0+1;
Ypos0 = floor(YposNew);
Ypos1 = Ypos0+1;

% find max of neighbouring indices
maxx = max([max(Xpos1),img1x+nC-1]);
maxy = max([max(Ypos1),img1y+nR-1]);

% get indices for neighbouring pixels
VecPosX0Y0 = reshape(sub2ind([maxy maxx],Ypos0,Xpos0),nR,nC);
VecPosX0Y1 = reshape(sub2ind([maxy maxx],Ypos1,Xpos0),nR,nC);
VecPosX1Y0 = reshape(sub2ind([maxy maxx],Ypos0,Xpos1),nR,nC);
VecPosX1Y1 = reshape(sub2ind([maxy maxx],Ypos1,Xpos1),nR,nC);

% reshape new and neighbouring indices
XposNew = reshape(XposNew,nR,nC);
YposNew = reshape(YposNew,nR,nC);
Xpos0 = reshape(Xpos0,nR,nC);
Xpos1 = reshape(Xpos1,nR,nC);
Ypos0 = reshape(Ypos0,nR,nC);
Ypos1 = reshape(Ypos1,nR,nC);

% make image from current frame with added boundaries (max value at fake
% boundaries)
imgPlusB = ones(maxy,maxx);
imgPlusB = 255*imgPlusB;
imgPlusB(img1y:img1y+nR-1,img1x:img1x+nC-1) = img;

subIX0Y0 = imgPlusB(VecPosX0Y0);
subIX0Y1 = imgPlusB(VecPosX0Y1);
subIX1Y0 = imgPlusB(VecPosX1Y0);
subIX1Y1 = imgPlusB(VecPosX1Y1);

imgNew = (Xpos1-XposNew).*(Ypos1-YposNew).*subIX0Y0 + ...
    (Xpos1-XposNew).*(YposNew-Ypos0).*subIX0Y1 +...
    (XposNew-Xpos0).*(Ypos1-YposNew).*subIX1Y0 +...
    (XposNew-Xpos0).*(YposNew-Ypos0).*subIX1Y1;
end
```

%----------

Bibliography

Aggarwal JK & Nandhakumar N (1988). On the computation of motion from sequences of images-A review. *Proceedings of the IEEE* **76**, 917–935.

Aguilar HN & Mitchell BF (2010). Physiological pathways and molecular mechanisms regulating uterine contractility. *Human Reproduction Update* **16**, 725–744.

Ahrens MB, Orger MB, Robson DN, Li JM & Keller PJ (2013). Whole-brain functional imaging at cellular resolution using light-sheet microscopy. *Nature Methods* **10**, 413–420.

Arnaudeau S, Leprêtre N & Mironneau J (1994a). Chloride and monovalent ion-selective cation currents activated by oxytocin in pregnant rat myometrial cells. *American Journal of Obstetrics and Gynecology* **171**, 491–501.

Arnaudeau S, Leprêtre N & Mironneau J (1994b). Oxytocin mobilizes calcium from a unique heparin-sensitive and thapsigargin-sensitive store in single myometrial cells from pregnant rats. *Pfl□gers Archiv European Journal of Physiology* **428**, 51–59.

Arrowsmith S & Wray S (2014). Oxtocin: its mechanism and action of receptor signalling in the myometrium. *Journal of Neuroendocrinology* **26**, 356–369.

Aslanidi O, Atia J, Benson AP, Van den Berg HA, Blanks AM, Choi C, Gilbert SH, Goryanin I, Hayes-Gill BR, Holden AV, Li P, Norman JE, Shmygol A, Simpson NAB, Taggart MJ, Tong WC & Zhang H (2011). Towards a computational reconstruction of the electrodynamics of premature and full term human labour. *Progress in Biophysics and Molecular Biology* **107**, 183–192.

Baker S & Matthews I (2004). Lucas-Kanade 20 Years On: A Unifying Framework. *International Journal of Computer Vision* **56**, 221–255.

Barron JL, Fleet DJ & Beauchemin SS (1994). Systems and experiment: performance of optical flow techniques. *International Journal of Computer Vision* **12**, 43–77.

Bassingthwaighte J, Hunter P & Noble D (2009). The Cardiac Physiome: perspectives for the future. *Experimental Physiology* **94**, 597–605.

Blanch G, Lavender T, Walkinshaw S & Alfirevic Z (1998). Dysfunctional labour: a randomised trial. *British Journal of Obstetrics and Gynaecology* **105**, 177–120.

Blanks A & Thornton S (2003). The role of oxytocin in parturition. *BJOG: An International Journal of Obstetrics and Gynaecology* **110**, 46–51.

Blanks AM, Zhao ZH, Shmygol A, Bru-Mercier G, Astle S & Thornton S (2007). Characterization of the molecular and electrophysiological properties of the T-type calcium channel in human myometrium. *The Journal of Physiology* **581**, 915–926.

Blanks AM, Shmygol A & Thornton S (2007). Myometrial function in prematurity. *Best Practice & Research Clinical Obstetrics & Gynaecology* **21**, 807–819.

Brainard AM, Korovkina VP & England SK (2007). Potassium channels and uterine function. *Seminars in Cell and Developmental Biology* **18**, 332–339.

Bru-Mercier G, Gullam JE, Thornton S, Blanks AM & Shmygol A (2012). Characterization of the tissue-level Ca2+ signals in spontaneously contracting human myometrium. *Journal of Cellular and Molecular Medicine* **16**, 2990–3000.

Burdyga T, Borisova L, Burdyga AT & Wray S (2009). Temporal and spatial variations in spontaneous Ca events and mechanical activity in pregnant rat myometrium. *European Journal of Obstetrics & Gynecology and Reproductive Biology* **144**, S25–S32.

Bursztyn L, Eytan O, Jaffa AJ & Elad D (2006). Mathematical model of excitation-contraction in a uterine smooth muscle cell. *AJP: Cell Physiology* **292**, C1816–C1829.

Camello C, Lomax R, Petersen OH & Tepikin AV (2002). Calcium leak from intracellular stores—the enigma of calcium signalling. *Cell Calcium* **32**, 355–361.

Chenouard N, Smal I, de Chaumont F, Maška M, Sbalzarini IF, Gong Y, Cardinale J, Carthel C, Coraluppi S, Winter M, Cohen AR, Godinez WJ, Rohr K, Kalaidzidis Y, Liang L, Duncan J, Shen H, Xu Y, Magnusson KEG, Jaldén J, Blau HM, Paul-Gilloteaux P, Roudot P, Kervrann C, Waharte F, Tinevez JY, Shorte SL, Willemse

J, Celler K, van Wezel GP, Dan HW, Tsai YS, Ortiz de Solórzano C, Olivo-Marin JC & Meijering E (2014). Objective comparison of particle tracking methods. *Nature Methods* **11**, 281–289.

Conrad JT, Kuhn WK & Johnson WL (1966). Stress relaxation in human uterine muscle. *American Journal of Obstetrics and Gynecology* **95**, 254–265.

Conrad JT, Johnson WL, Kuhn WK & Hunter J CA (1966). Passive stretch relationships in human uterine muscle. *American Journal of Obstetrics and Gynecology* **96**, 1055–1059.

Döring B, Shynlova O, Tsui P, Eckardt D, Janssen-Bienhold U, Hofmann F, Feil S, Feil R, Lye SJ & Willecke K (2006). Ablation of connexin43 in uterine smooth muscle cells of the mouse causes delayed parturition. *Journal of Cell Science* **119**, 1715–1722.

Duquette RA, Shmygol A, Vaillant C, Mobasheri A, Pope M, Burdyga T & Wray S (2005). Vimentin-Positive, c-KIT-Negative Interstitial Cells in Human and Rat Uterus: A Role in Pacemaking? *Biology of Reproduction* **72**, 276–283.

Fomin VP, Gibbs SG, Vanam R, Morimiya A & Hurd WW (2006). Effect of magnesium sulfate on contractile force and intracellular calcium concentration in pregnant human myometrium. *American Journal of Obstetrics and Gynecology* **194**, 1384–1390.

Fu X, Yi-Jia L, Ciray N, Olovsson M, Ulmsten U & Gylfe E (2000). Oxytocin-induced oscillations of cytoplasmic Ca2+ in human myometrial cells. *Acta Obstetricia et Gynecologica Scandinavica* **79**, 174–179.

Garfield RE, Sims S & Daniel EE (1977). Gap Junctions: Their Presence and Necessity in Myometrium During Parturition. *Science* **198**, 958–960.

Garfield RE, Sims SM, Kannan MS & Daniel EE (1978). Possible role of gap junctions in activation of myometrium during parturition. *Am J Physiol Cell Physiol* **235**, C168–C179.

Greenberg DS & Kerr JND (2009). Automated correction of fast motion artifacts for two-photon imaging of awake animals. *Journal of Neuroscience Methods* **176**, 1–15.

Gullam JE, Blanks AM, Thornton S & Shmygol A (2009). Phase-plot analysis of the oxytocin effect on human myometrial contractility. *European Journal of Obstetrics & Gynecology and Reproductive Biology* **144**, S20–S24.

Hai CM & Murphy RA (1988). Cross-bridge phosphorylation and regulation of latch state in smooth muscle. *American Journal of Cell Physiology* **254**, C99–C106.

Hennig GW, Smith CB, O'Shea DM & Smith TK (2002). Patterns of intracellular and intercellular Ca2+ waves in the longitudinal muscle layer of the murine large intestine In vitro. *The Journal of Physiology* **543**, 233–253.

Horn BKP & Schunck BG (1981). Determining Optical Flow. *Artificial Intelligence* **17**, 185–203.

Hudson CA, Heesom KJ & Bernal AL (2012). Phasic contractions of isolated human myometrium are associated with Rho-kinase (ROCK)-dependent phosphorylation of myosin phosphatase-targeting subunit (MYPT1). *Molecular Human Reproduction* **18**, 265–279.

Hyrc KL, Rzeszotnik Z, Kennedy BR & Goldberg MP (2007). Determining calcium concentration in heterogeneous model systems using multiple indicators. *Cell Calcium* **42**, 576–589.

Inoue Y & Sperelakis N (1991). Gestational change in Na+ and Ca2+ channel current densities in rat myometrial smooth muscle cells. *American Journal of Physiology - Cell Physiology* **260**, C658–C663.

Irfanoglu B & Karaesmen E (1993). A biomechanical model for the gravid uterus In al CBe, editor, *Trans Biomed Health*, pp. 59–65.

Jones K, Shmygol A, Kupittayanant S & Wray S (2004). Electrophysiological characterization and functional importance of calcium-activated chloride channel in rat uterine myocytes. *Pflügers Archiv European Journal of Physiology* **448**, 36–43.

Khan RN, Matharoo-Ball B, Arulkumaran S & Ashford ML (2001). Potassium channels in the human myometrium. *Experimental Physiology* **86**, 255–264.

Kitazawa T, Eto M, Woodsome TP & Brautigan DL (2000). Agonists Trigger G Protein-mediated Activation of the CPI-17 Inhibitor Phosphoprotein of Myosin Light Chain Phosphatase to Enhance Vascular Smooth Muscle Contractility. *Journal of Biological Chemistry* **275**, 9897–9900.

Knock GA, Smirnov SV & Aaronson PI (2004). Voltage-gated K +currents in freshly isolated myocytes of the pregnant human myometrium. *The Journal of Physiology* **518**, 769–781.

Kupittayanant S, Burdyga T & Wray S (2001). The effects of inhibiting Rho-associated kinase with Y-27632 on force and intracellular calcium in human myometrium. *Pflügers Archiv European Journal of Physiology* **443**, 112–114.

Kuriyama H, Kitamura K, Itoh T & Inoue R (1998). Physiological Features of Visceral Smooth Muscle Cells, With Special Reference to Receptors and Ion Channels. *Physiological Reviews* **78**, 881–920.

Lammers WJEP (2013). The electrical activities of the uterus during pregnancy. *Reproductive sciences (Thousand Oaks, Calif.)* **20**, 182–189.

Lammers WJEP, Mirghani H, Stephen B, Dhanasekaran S, Wahab A, Al Sultan MAH & Abazer F (2008). Patterns of electrical propagation in the intact pregnant guinea pig uterus. *Am J Physiol Regul Integr Comp Physiol* **294**, R919–R928.

Lammers WJEP, Stephen B, Al-Sultan MA, Subramanya SB & Blanks AM (2015). The location of pacemakers in the uteri of pregnant guinea pigs and rats. *AJP: Regulatory, Integrative and Comparative Physiology* **309**, R1439–R1446.

Loftus FC, Richardson MJE & Shmygol A (2015). Single-cell mechanics and calcium signalling in organotypic slices of human myometrium. *Journal of Biomechanics* **48**, 1620–1624.

Loftus FC, Shmygol A & Richardson MJE (2014). Fine spatiotemporal activity in contracting myometrium revealed by motion-corrected calcium imaging. *The Journal of Physiology* **592**, 4447–4463.

Longbottom ER, Luckas MJM, Kupittayanant S, Badrick E, Shmigol T & Wray S (2000). The effects of inhibiting myosin light chain kinase on contraction and calcium signalling in human and rat myometrium. *Pflügers Archiv - European Journal of Physiology* **440**, 315–321.

Lucas BD & Kanade T (1981). An Iterative Image Registration Technique with an Application to Stereo Vision. *Proceedings of Imaging Understanding Workshop* pp. 121–130.

Luckas MJM, Taggart MJ & Wray S (1999). Intracellular calcium stores and agonist-induced contractions in isolated human myometrium. *American Journal of Obstetrics and Gynecology* **181**, 1–9.

Lye SJ, Nicholson BJ, Mascarenhas M, MacKenzie L & Petrocelli T (1993). Increased expression of connexin-43 in the rat myometrium during labor is asso-

ciated with an increase in the plasma estrogen:progesterone ratio. *Endocrinology* **132**, 2380–2386.

Mailloux GE, Bleau A & Bertrand M (1987). Computer Analysis of Heart Motion from Two-Dimensional Echocardiograme. *IEEE Transactions on Biomedical Engineering* **BME-34**, 356–364.

Mailloux GE, Langlois F, Simard PY & Bertrand M (1989). Restoration of the Velocity Field of the Heart from Two-Dimensional Echocardiograms. *IEEE Transactions on Medical Imaging* **8**, 143–153.

Mansi T, Pennec X, Sermesant M, Delingette H & Ayache N (2011). iLogDemons: A Demons-Based Registration Algorithm for Tracking Incompressible Elastic Biological Tissues. *International Journal of Computer Vision* **92**, 92–111.

McKillen K, Thornton S & Taylor CW (1999). Oxytocin increases the [Ca2+]i sensitivity of human myometrium during the falling phase of phasic contractions. *American Journal of Physiology - Endocrinology and Metabolism* **276**, E345–E351.

Meijering E, Dzyubachyk O & Smal I (2012). Methods for Cell and Particle Tracking In Conn PM, editor, *Imaging and Spectroscopic Analysis of Living Cells*, pp. 183–200. Elsevier.

Miftahof RN & Nam HG (2011). *Biomechanics of the Gravid Human Uterus* Springer-Verlag.

Miyoshi H, Boyle MB, Mackay LB & Garfield RE (1998). Gap junction currents in cultured muscle cells from human myometrium. *American Journal of Obstetrics and Gynecology* **178**, 588–593.

Mizrahi J, Karni Z & Polishuk WZ (1978). A kinematic analysis of uterine deformation during labor. *Journal of The Franklin Institute* **306**.

Monga M, Campbell DF & Sanborn BM (2016). Oxytocin-stimulated capacitative calcium entry in human myometrial cells. *American Journal of Obstetrics and Gynecology* **181**, 424–429.

Nakao K, Inoue Y, Okabe K, Kawarabayashi T & Kitamura K (1997). Oxytocin enhances action potentials in pregnant human myometrium A study with microelectrodes. *American Journal of Obstetrics and Gynecology* **177**, 222–228.

Nobel D, Borysova L, Wray S & Burdyga T (2014). Store-operated Ca2+ entry and depolarization explain the anomalous behaviour of myometrial SR: effects of SERCA inhibition on electrical activity and force. *Cell Calcium* **56**, 188–184.

Noble K & Wray S (2002). The role of the sarcoplasmic reticulum in neonatal uterine smooth muscle: enhanced role compared to adult rat. *The Journal of Physiology* **545**, 557–566.

Nordsletten DA, Niederer SA, Nash MP & Hunter PJ (2011). Computing multiphysics models to cardiac mechanics. *Progress in Biophysics and Molecular Biology* **104**, 77–88.

Parkington HC, Tonta MA, Brennecke SP & Coleman HA (1999). Contractile activity, membrane potential, and cytoplasmic calcium in human uterine smooth muscle in the third trimester of pregnancy and during labor. *American Journal of Obstetrics and Gynecology* **181**, 1445–1451.

Pearsall GW & Roberts VL (1978). Passive mechanical properties of uterine muscle (myometrium) tested in vitro. *Journal of Biomechanics* **11**, 167–176.

Portugues R, Feierstein CE, Engert F & Orger MB (2014). Whole-Brain Activity Maps Reveal Stereotyped, Distributed Networks for Visuomotor Behavior. *Neuron* **81**, 1328–1343.

Shlykov SG & Sanborn BM (2004). Stimulation of intracellular Ca2+ oscillations by diacylglycerol in human myometrial cells. *Cell Calcium* **36**, 157–164.

Shmigol AV, Eisner DA & Wray S (1998). Properties of voltage-activated [Ca2+]i transients in single smooth muscle cells isolated from pregnant rat uterus. *Journal of Physiology* **511**, 803–811.

Shmygol A, Blanks AM, Bru-Mercier G, Gullam JE & Thornton S (2007). Control of uterine Ca2+ by membrane voltage. *Annals of the New York Academy of Sciences* **1101**, 97–109.

Shmygol A, Gullam JE, Blanks A & Thornton S (2006). Multiple mechanisms involved in oxytocin-induced modulation of myometrial contractility. *Acta Pharmacologica Sinica* **27**, 827–832.

Shmygol A & Wray S (2004). Functional architecture of the SR calcium store in uterine smooth muscle. *Cell Calcium* **35**, 501–508.

Spaery C, Robson SC, Bailey J, Lyall F & Europe-Finner GN (1999). The Differential Expression of Myometrial Connexin-43 Cyclooxygenase-1 and -2 and Gsalpha Proteins in the Upper and Lower Segments of the Human Uterus during Pregnancy and Labor. *The Journal of Clinical Endocrinology and Metabolism* **84**, 1705–1710.

Suffoletto MS (2006). Novel Speckle-Tracking Radial Strain From Routine Black-and-White Echocardiographic Images to Quantify Dyssynchrony and Predict Response to Cardiac Resynchronization Therapy. *Circulation* **113**, 960–968.

Taggart MJ, Burdyga T, Heaton R & Wray S (1996). Stimulus-dependent modulation of smooth muscle intracellular calcium and force by altered intracellular pH. *Pflügers Archiv - European Journal of Physiology* **432**, 803–811.

Thornton S, Davidson JM & Baylis PH (1992). Plasma oxytocin during the first and second stages of spontaneous human labour. *Acta Endocrinology* **126**, 425–429.

Thornton S, Gillespie JI, Greenwell JR & Dunlop W (1992). Mobilization of calcium by the brief application of oxytocin and prostaglandin E2 in single cultured human myometrial cells. *Experimental Physiology* **77**, 293–305.

Thornton S, McKillen HC & Taylor CW (1998). Oxytocin increases the sensitivity in vitro of the contractile apparatus to Ca2+ in human pregnant myometrium. *The Journal of Physiology* **506 (Suppl)**, 144P.

Thul R, Coombes S & Bootman MD (2012). Persistence of pro-arrhythmic spatio-temporal calcium patterns in atrial myocytes: a computational study of ping waves. *Frontiers in Physiology* **3**, 1–8.

Thul R, Coombes S, Llewelyn Roderick H & Bootman MD (2012). Subcellular calcium dynamics in a whole-cell model of an atrial myocyte. *PNAS* **109**, 2150–2155.

Tomasi C & Kanade T (1991). Detection and Tracking of Point Features Technical report CMU-CS-91-132.

Tomek J, Novak O & Syka J (2013). Two-Photon Processor and SeNeCA: a freely available software package to process data from two-photon calcium imaging at speeds down to several milliseconds per frame. *Journal of Neurophysiology* **110**, 243–256.

Vauge C, Carbonne B, Papiernik E & Ferre F (2000). A Mathematical Model of Uterine Dynamics and its Application to Human Parturition. *Acta Biotheoretica* **48**, 95–105.

Wedisinghe L, Macleod M & Murphy DJ (2008). Use of oxytocin to prevent haemorrhage at caesarean section—A survey of practice in the United Kingdom. *European Journal of Obstetrics & Gynecology and Reproductive Biology* **137**, 27–30.

Weiss S, Bajka M, Nava A, Mazza E & Niederer P (2004). A finite element model for the simulation of hydrometra. *Technology and health care : official journal of the European Society for Engineering and Medicine* **12**, 259–267.

Weiss S, Jaermann T, Schmid P, Staempfli P, Boesiger P, Niederer P, Caduff R & Bajka M (2006). Three-dimensional fiber architecture of the nonpregnant human uterus determined ex vivo using magnetic resonance diffusion tensor imaging. *The Anatomical Record Part A: Discoveries in Molecular, Cellular, and Evolutionary Biology* **288A**, 84–90.

Westerweel J (1994). Efficient detection of spurious vectors in particle image velocimetry data. *Experiments in Fluids* **16**, 236–247.

Westerweel J & Scarano F (2005). Universal outlier detection for PIV data. *Experiments in Fluids* **39**, 1096–1100.

Woodcock NA, Taylor CW & Thornton S (2004). Effect of an oxytocin receptor antagonist and rho kinase inhibitor on the [Ca++]i sensitivity of human myometrium. *American Journal of Obstetrics and Gynecology* **190**, 222–228.

Word RA, Tang DC & Kamm KE (1994). Activation Properties of Myosin Light Chain Kinase during Contraction/Relaxation Cycles of Tonic and Phasic Smooth Muscles. *The Journal of Biological Chemistry* **269**, 21596–21602.

Wray S, Burdyga T, Noble D, Noble K, Borysova L & Arrowsmith S (2014). Progress in understanding electro-mechanical signalling in the myometrium. *Acta Physiologica* **213**, 417–431.

Yang J & Leskovec J (2011). Patterns of Temporal Variation in Online Media In *ACM International Conference on Web Search and Data Mining (WSDM '11)*.

Young RC (2007). Myocytes, myometrium, and uterine contractions. *Ann. N.Y. Acad. Sci* **1101**, 72–74.

Young RC & Hession RO (1996). Intra- and intercellular calcium waves in cultured human myometrium. *Journal of Muscle Research and Cell Motility* **17**, 349–355.

Young RC, Schumann R & Zhang P (2001). Intracellular calcium gradients in cultured human uterine smooth muscle: a functionally important subplasmalemmal space. *Cell Calcium* **29**, 183–189.

Young RC & Zhang P (2001). The mechanism of propagation of intracellular calcium waves in cultured human uterine myocytes. *Am J Obstet Gynecol* **184**, 1228–1234.

Young RC & Barendse P (2014). Linking Myometrial Physiology to Intrauterine Pressure; How Tissue-Level Contractions Create Uterine Contractions of Labor. *PLOS Computational Biology* **10**, e1003850.

Young RC & Hession RO (1999). Three-Dimensional Structure of the Smooth Muscle in the Term-Pregnant Human Uterus. *Obstetrics and Gynecology* **93**, 94–99.

Yu JT & Lopez Bernal A (1998). The cytoskeleton of human myometrial cells. *Reproduction* **112**, 185–198.